USGS
science for a changing world

National Cooperative Geologic Mapping Program

Geologic Map and Hydrogeologic Investigations of the Upper Santa Cruz River Basin, Southern Arizona

By William R. Page, Mark W. Bultman, Margaret E. Berry, Kenzie J. Turner, Christopher M. Menges, Floyd Gray, James B. Paces, D. Paco VanSistine, Leah E. Morgan, and Jeremy C. Havens

Pamphlet to accompany

Scientific Investigations Map 3490

U.S. Department of the Interior
U.S. Geological Survey

Cover. Looking south across the southern end of Peña Blanca Lake. The red rocks in the foreground are tuffaceous deposits of the Oligocene Montana Peak Formation. The light-colored cliffs in the background are a pumice-bearing tuff of the Oligocene Atascosa Formation. Photograph by Mark W. Bultman, U.S. Geological Survey.

Geologic Map and Hydrogeologic Investigations of the Upper Santa Cruz River Basin, Southern Arizona

By William R. Page, Mark W. Bultman, Margaret E. Berry, Kenzie J. Turner, Christopher M. Menges, Floyd Gray, James B. Paces, D. Paco VanSistine, Leah E. Morgan, and Jeremy C. Havens

National Cooperative Geologic Mapping Program

Pamphlet to accompany
Scientific Investigations Map 3490

U.S. Department of the Interior
U.S. Geological Survey

U.S. Geological Survey, Reston, Virginia: 2023

Suggested citation:
Page, W.R., Bultman, M.W., Berry, M.E., Turner, K.J., Menges, C.M., Gray, F., Paces, J.B., VanSistine, D.P., Morgan, L.E., and Havens, J.C., 2023, Geologic map and hydrogeologic investigations of the upper Santa Cruz River basin, southern Arizona: U.S. Geological Survey Scientific Investigations Map 3490, 2 sheets, scale 1:50,000, 73-p. pamphlet, https://doi.org/10.3133/sim3490.

Associated data for this publication:
Bultman, M.W., 2023, Sopori Wash sub-basin gravity data, Pima and Santa Cruz Counties, Arizona: U.S. Geological Survey data release, https://doi.org/10.5066/P9MBNX4O.

Morgan, L.E., 2021, Argon data for Santa Cruz Basin, Arizona (ver. 1.1, November 2022): U.S. Geological Survey data release, accessed December 1, 2022, at https://doi.org/10.5066/P94NR0D9.

Paces, J.B., 2021, Sr-, U-, H- and O-isotope data used to evaluate water sources in the Potrero Creek wetlands, upper Santa Cruz basin, southern Arizona, USA: U.S. Geological Survey data release, https://doi.org/10.5066/P9XXW25T.

Page, W.R., Bultman, M.W., Berry, M.E., Turner, K.J., Menges, C.M., Gray, F., Paces, J.B., VanSistine, D.P., Morgan, L.E., and Havens, J.C., 2023, Database for the geologic map of the upper Santa Cruz River basin, southern Arizona: U.S. Geological Survey data release, https://doi.org/10.5066/P9PGUZV0.

ISSN 2329-132X (online)

Acknowledgments

We thank Dr. Olga Hart and Dr. Keith Nelson, Arizona Department of Water Resources (Phoenix, Arizona) for their significant contributions to this project, as they joined us in the field regularly during the course of geologic mapping and other field work to better understand the interplay between geology and hydrology. Our organizations held collaborative fieldtrips with members of the Santa Cruz River Users Advisory Council (ADWR, City of Nogales, Bureau of Reclamation, Bureau of Land Management, U.S. Forest Service, local ranchers and farmers, and others) to better understand the geology and hydrology of the upper Santa Cruz River basin. Dr. Olga Hart collected water samples from the Potrero wetlands area from local wells and samples which were analyzed for isotopic data signatures indictive of certain groundwater sources, included in this report.

Contents

Figures

Tables

Conversion Factors

U.S. customary units to International System of Units

Multiply	By	To obtain
	Length	
centimeter (cm)	0.3937	inch (in.)
millimeter (mm)	0.03937	inch (in.)
meter (m)	3.281	foot (ft)
kilometer (km)	0.6214	mile (mi)
kilometer (km)	0.5400	mile, nautical (nmi)
meter (m)	1.094	yard (yd)
	Area	
square meter (m^2)	0.0002471	acre
hectare (ha)	2.471	acre
square hectometer (hm^2)	2.471	acre
square kilometer (km^2)	247.1	acre
square centimeter (cm^2)	0.001076	square foot (ft^2)
square meter (m^2)	10.76	square foot (ft^2)
square centimeter (cm^2)	0.1550	square inch (in^2)
square hectometer (hm^2)	0.003861	section (640 acres or 1 square mile)
hectare (ha)	0.003861	square mile (mi^2)
square kilometer (km^2)	0.3861	square mile (mi^2)

Datum

Vertical coordinate information is referenced to the North American Vertical Datum of 1988 (NAVD 88).

Horizontal coordinate information is referenced to the North American Datum of 1983 (NAD 83).

Altitude, as used in this report, refers to distance above the vertical datum.

Geologic Time Divisions

Period and subperiod		Epoch		Age
Quaternary		Holocene	late	0–4.2 ka
			middle	4.2–8.2 ka
			early	8.2–11.7 ka
		Pleistocene	late	11.7–129 ka
			middle	129–774 ka
			early	774 ka–2.58 Ma
Tertiary	Neogene	Pliocene		2.58–5.333 Ma
		Miocene	late	5.333–11.63 Ma
			middle	11.63–15.97 Ma
			early	15.97–23.03 Ma
	Paleogene	Oligocene		23.03–33.9 Ma
		Eocene		33.9–56.0 Ma
		Paleocene	late	56.0–59.2 Ma
			middle	59.2–61.6 Ma
			early	61.6–66.0 Ma

Ages of time boundaries are those of Cohen and others (2013, updated) and the U.S. Geological Survey Geologic Names Committee (2018). Ages are expressed in ka for kilo-annum (thousands of years before present) and Ma for mega-annum (millions of years before present).

Abbreviations

3-D	three dimensional
CDT	conductivity depth transforms
DEM	digital elevation model
Ma	mega-annum
TEM	transient electromagnetic
S/m	Siemens per meter

Geologic Map and Hydrogeologic Investigations of the Upper Santa Cruz River Basin, Southern Arizona

By William R. Page[1], Mark W. Bultman[1], Margaret E. Berry[1], Kenzie J. Turner[1], Christopher M. Menges[1], Floyd Gray[1], James B. Paces[1], D. Paco VanSistine[1], Leah E. Morgan[1], and Jeremy C. Havens[2]

Abstract

This report includes an updated geologic map and cross sections of the upper Santa Cruz River basin, southern Arizona. The map and cross sections describe the geometry, thickness, and structure of the Miocene to Holocene units which form the main aquifers in the basin. The report also includes results of new hydrogeologic studies including (1) mapping and defining depth to bedrock based on geophysical data in the map area to better define the geometry and structure of the basin aquifers, (2) describing newly recognized hydrologically significant faults in the Peck Canyon and Sopori Wash areas, and (3) evaluating groundwater sources and hydrogeology of the Potrero Creek wetlands.

Introduction

This report presents an updated geologic map of the upper Santa Cruz River basin (fig. 1, sheet 1) emphasizing basin hydrogeology and structure. The map was compiled and designed to describe major basin aquifers composed of Miocene to early Pleistocene basin-fill deposits, and early Pleistocene to Holocene alluvial sediments which represent basin erosional and depositional intervals and associated geomorphic surfaces. The upper Santa Cruz River aquifer system provides groundwater to Nogales (Sonora), Nogales and Rio Rico (Arizona) and adjoining communities (fig. 1). The southern edge of the map is the international border with Sonora, Mexico. The new map includes seven hydrogeologic cross sections (sheet 2) illustrating the geometry, thickness, and structure of the Miocene to Holocene aquifer units. Additional results of new project hydrogeologic studies are presented in the report, including (1) mapping and defining the depth to bedrock in the map area to better understand the geometry and structure of the Miocene to Holocene aquifers; (2) describing hydraulically significant new faults and zones of high hydraulic conductivity in the Sopori Wash and Peck Canyon focus areas; and (3) evaluating groundwater sources and hydrogeology of the Potrero Creek wetlands area based on isotopic data, groundwater geochemistry, and geologic and geophysical data. Also included are brief summaries of our previously published geologic, geophysical, and hydrogeologic studies in the upper Santa Cruz River basin (Bultman and Page, 2016; Page and others, 2016a and b; and Page and others, 2018).

Methodology

Map Compilation Methods

The map was compiled digitally in ArcMap (versions 10.5 and 10.7.1) with the aid of NAIP orthophotography, imagery viewed with Google Earth, 1996 National Aerial Photography Program (NAPP) 1:40,000 scale color infrared aerial photographs, 1958 Department of Agriculture 1:20,000 scale black and white aerial photographs, 1:24,000 and 1:100,000-scale topographic maps, and a high-resolution (2-m) bare earth digital elevation model (DEM) for Santa Cruz County derived from lidar flown in 2004. The database for the geologic map presented in sheet 1 is from Page and others (2023).

Bedrock units were compiled from existing geologic maps (see sheet 1, fig. 2), primarily from Drewes (1971b, 1980), Simons (1974), and Graybeal and others (2015). Bedrock map unit descriptions and linework were used from those reports with minor modifications, and location of some unit contacts and faults were adjusted, or shifted, based on interpretations made to match the linework with the various imagery viewed in ArcMap. In areas where it was not possible to interpret and adjust contacts or faults based on imagery, the original linework was left unchanged. New reconnaissance-scale mapping of Oligocene volcanic rocks was conducted for this report, primarily in the Atascosa and Tumacacori Mountains. The mapping is supported by argon geochronology (Morgan, 2021), resulting in a better understanding of these rocks as they relate to the regional geology.

[1]U.S. Geological Survey.

[2]A-sa-ma-di (Smart) Business Solutions, LLC.

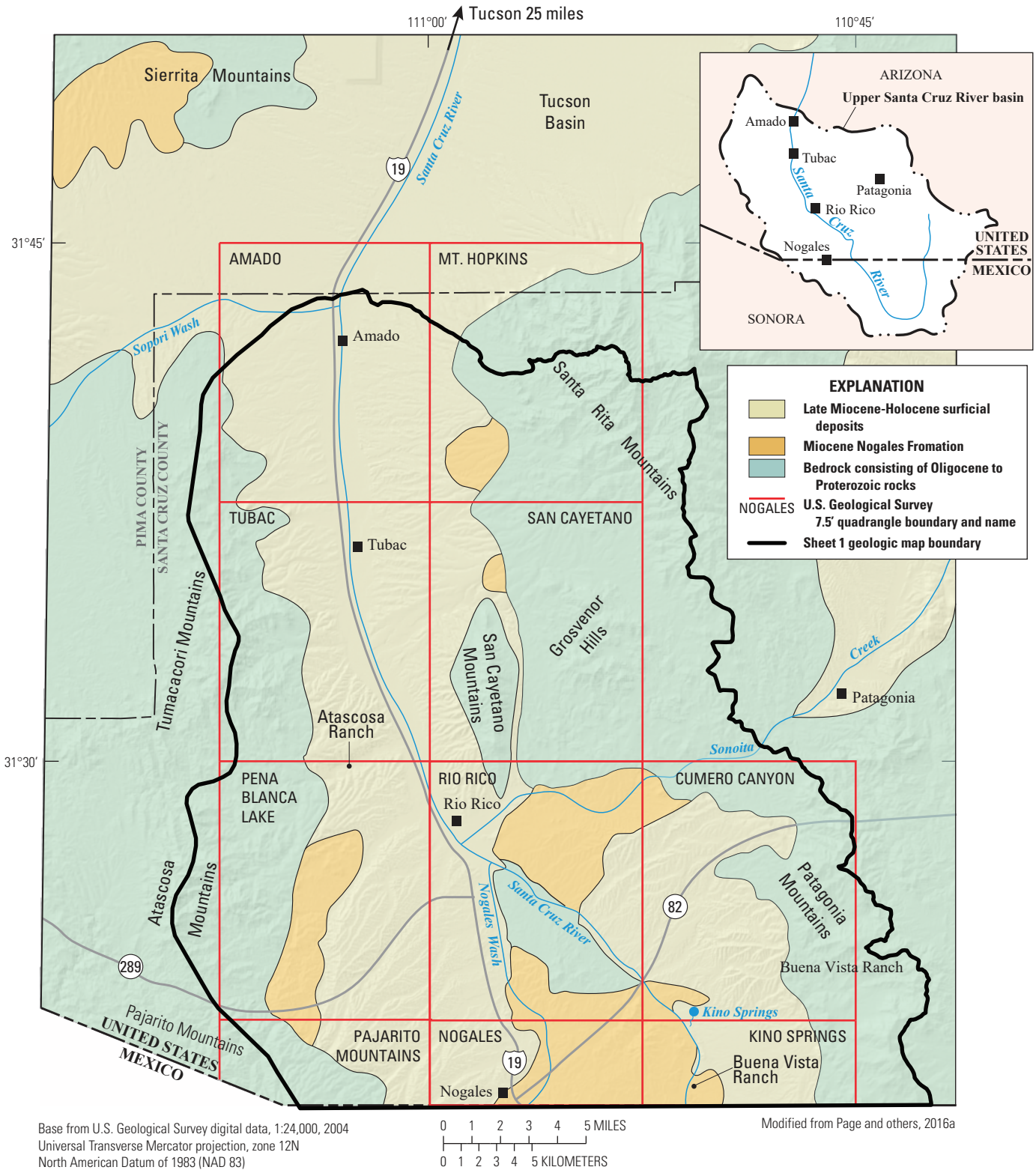

Figure 1. Index map of the upper Santa Cruz River basin showing major physiographic, geologic, and hydrogeologic features in the map region. Black squares are town locations. Inset map in upper right shows location of upper Santa Cruz River basin with dashed boundary and Santa Cruz River in blue.

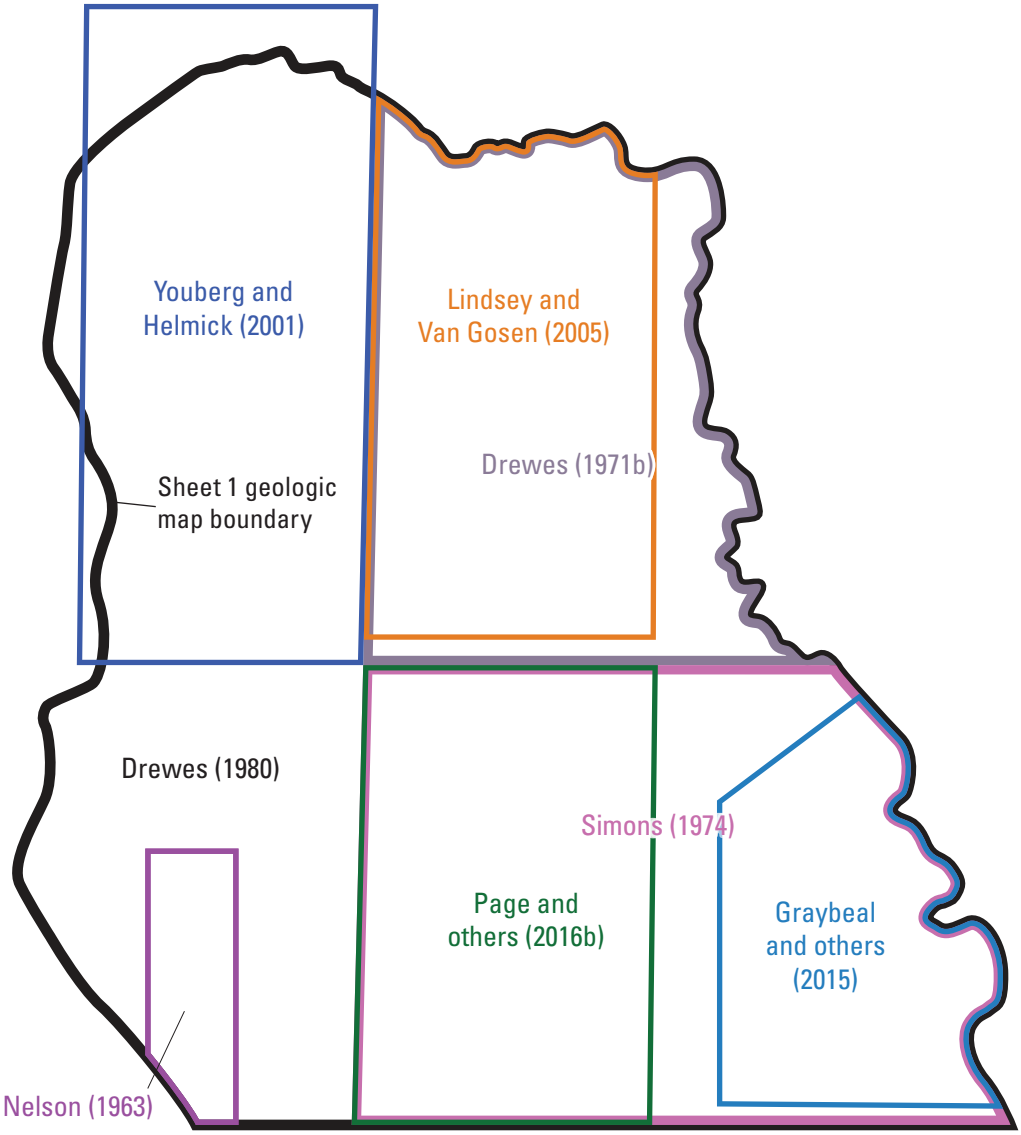

Figure 2. Geologic map sources used in the compilation of sheet 1 (Nelson, 1963; Drewes, 1971b; Simons, 1974; Drewes, 1980 [a contribution including and extending beyond the mapped limit]; Youberg and Helmick, 2001; Lindsey and Van Gosen, 2005; Graybeal and others, 2015; Page and others, 2016b).

Faults and contacts in the Rio Rico and Nogales 7.5 minute (′) quadrangles were compiled from Page and others (2016b), who conducted new 1:24,000 scale detailed mapping primarily of the Miocene to Holocene basin-fill and alluvial deposits which form the main aquifers in the upper Santa Cruz River basin. These units include the Miocene Nogales Formation, late Miocene to early? Pleistocene basin-fill deposits, and early Pleistocene to Holocene alluvial deposits.

Surficial units were mostly compiled from existing geologic maps (see sheet 1, fig. 2), primarily from Page and others (2016b), Youberg and Helmick (2001), Helmick (1986), and Lindsey and Van Gosen (2005), with minor modifications to unit designations and locations of contacts and faults, which were adjusted based on interpretation from the previously listed imagery and soils data (U.S. Department of Agriculture Natural Resources Conservation Service, 2008). Unit descriptions were compiled from the listed reports and from local field observations.

Geophysical Methods

New geophysical investigations were completed in conjunction with compilation of the upper Santa Cruz River basin geologic map (sheet 1) and cross sections (sheet 2). The main result was the development of a new depth to bedrock model for sheets 1 and 2 and adjacent areas (see “Depth to Bedrock

in the Geologic Map Area" section). This model is essential to understanding and interpreting the subsurface geometry, structure, stratigraphy, and hydrogeology of the Miocene to Holocene basin aquifers within and adjacent to the sheet 1 map area. The new depth to bedrock model is based on analyzing both gravity and aeromagnetic data from Gettings and Houser (1997) and Bultman and Page (2016), both of which applied different geophysical methods discussed below.

Gettings and Houser's (1997) model covers the entire area of sheet 1 and extends into the northern upper Santa Cruz River basin. Their study applied density functions of the basin sediments combined with a residual gravity anomaly grid (1 kilometer [km] cell size) which was obtained by subtracting the gravity effects of bedrock ranges bordering the basins from the complete Bouguer gravity anomaly. Bultman and Page (2016) estimated depth to bedrock for the Rio Rico and Nogales 7.5′ quadrangles by analyzing the 1996 Patagonia aeromagnetic survey using three different methods: horizontal gradient analysis; analytic signal analyses; and Euler deconvolution. The 250 m flight line spatial density allows for a more detailed model than the Gettings and Houser (1997) more regional model. Further discussion of the methodology developed for the new model is discussed in the "Depth to Bedrock" section.

In addition to the development of a new depth to bedrock model for the area of sheets 1 and 2, several additional geophysically based hydrogeologic studies were completed for this report including (1) modeling depth to bedrock in the Sopori Wash sub-basin, which borders but is mostly outside the northwest boundary of sheet 1; and (2) investigating hydrologically significant faults and their influence on groundwater flow in the Peck Canyon area.

The Sopori Wash sub-basin was modeled because (1) it has not been studied in detail, (2) it is a moderately deep basin that drains into the Santa Cruz River in the northern map area (sheet 1), and (3) it is part of the Arizona Department of Water Resources Santa Cruz Active Management Area (https://new.azwater.gov/ama/santa-cruz). Data from 40 new gravity stations were collected in the Sopori Wash sub-basin area for this report (Bultman, 2023), and results further refined the basin structure, geometry, and estimated the basin depth at about 700 m. See the "Depth to Bedrock in the Sopori Wash Sub-Basin" section for further details on the basin.

New geophysical and geologic investigations were also conducted in the Peck Canyon area, an area where unusually stable groundwater levels are observed along faults which may serve as conduits for groundwater movement and recharge to the northern upper Santa Cruz River basin. These studies included (1) mapping exposed faults (that is, the Lowell fault), and (2) identifying concealed faults by analyzing curvilinear maxima from the gradient of the complete Bouguer anomaly data, and which represent rocks of different densities juxtaposed across the faults. In addition, we interpreted transient electromagnetic (TEM) data which were used to interpret concealed faults and indicate clay zones and or saturated sediments. See "Peck Canyon" section for further details and complete discussion of all geophysical methods used.

Geochronology Methods

Previously reported geochronologic ages for the map area were determined over the span of approximately the last 50 years with the application of multiple analytical methods including K-Ar, $^{40}Ar/^{39}Ar$, U-Pb zircon, and zircon lead-alpha. Assessing these reported ages is complicated by variation in analytical methods, isotopic systems, and related decay constants used to determine the calculated age. Accepted values for decay constants and standardized mineral ages used for calibration have changed through the years resulting in calculated differences of 1 to 2 percent. Furthermore, K-Ar and lead-alpha methods are outdated geochronometers having been superseded by more precise methods. The lead-alpha method used aliquots of multiple zircon grains that did not account for potential variability of ages between grains or between zones within individual grains. Furthermore, the method was imprecise, which is reflected in large uncertainties ranging from about 10 to 30 percent for ages reported in Marvin and others (1973). Modern zircon dating methods, however, are more precise with uncertainties generally less than 1 percent (for example, Vikre and others, 2014). In addition, modern in situ zircon dating methods can determine the age of individual domains within a single grain as opposed to an age determined from the entirety of many grains for the lead-alpha method. Most ages in this report are based on K-Ar and $^{40}Ar/^{39}Ar$ methods, and it is worth noting that variables factoring into the calculated age can complicate direct comparison of ages.

Ages determined using K-Ar and $^{40}Ar/^{39}Ar$ methods require the use of reliable decay constants for ^{40}K and, in the case of the $^{40}Ar/^{39}Ar$ method, a mineral standard of assumed age. Decay constants were standardized by Steiger and Jäger (1977), but Drewes (1981) noted that K-Ar ages in his study area utilizing the Steiger and Jäger (1977) values were about 2 percent older than ages calculated using previously accepted values with which some ages were calculated. The $^{40}Ar/^{39}Ar$ method also utilized decay constants of Steiger and Jäger (1977) for many years, but more recent decay constants are now commonly used (for example, Min and others, 2000). Furthermore, the $^{40}Ar/^{39}Ar$ method is dependent upon co-irradiating and measuring isotopes of the unknown sample and a mineral standard, or neutron fluence monitor, with an assumed age. Sanidine grains from the Fish Canyon Tuff are commonly used as a neutron fluence monitor. Accepted ages for the Fish Canyon Tuff have fluctuated slightly over the years and include 27.84 mega-annum (Ma; Deino and Potts, 1990; uncertainty not reported; age was adjusted by Deino and Potts [1990] from 27.9 Ma reported by Cebula and others [1986]), 28.02±0.32 Ma (Renne and others, 1998; uncertainty adjusted to 2 sigma), and 28.201±0.023 Ma (Kuiper and others, 2008; 2-sigma uncertainty), among others. Variations in the neutron fluence monitor age and decay constants can

result in an age difference of about 1 percent or less. To illustrate, a 30 Ma age calculated for a sample based on 28.02 Ma Fish Canyon Tuff age (Renne and others, 1998) and decay constants from Steiger and Jäger (1977) will instead be about 30.2 Ma when calculated using the 28.201 Ma age (Kuiper and others, 2008) and decay constants of Min and others (2000). New sample ages in this report (table 1; figs. 3–6) and ages reported by Page and others (2016b) are calculated relative to a Fish Canyon Tuff age of 28.201±0.023 Ma (Kuiper and others, 2008) and decay constants of Min and others (2000).

K-Ar and $^{40}Ar/^{39}Ar$ ages from other published sources cited in this report are not corrected so that all ages are relative to common decay constants and neutron fluence monitor ages for multiple reasons. Drewes (1981) reported K-Ar ages in an informal manner by rounding to the nearest million years and reporting no uncertainties. Although many of these ages are derived from previously published sources where the decay constants and monitor ages are indicated, many other ages are from unpublished sources with no indication of decay constants used in calculating the age. Additionally, the fluence monitor ages and decay constants are not indicated for $^{40}Ar/^{39}Ar$ ages reported by Seaman and others (1995). Given the publication year, these ages were certainly not calculated using the Kuiper and others (2008) monitor age or decay constants of Min and others (2000) and, therefore, could be up to about 1 percent younger relative to new $^{40}Ar/^{39}Ar$ ages reported here (table 1) or by Page and others (2016b).

Table 1. Geochronology data for volcanic rocks analyzed for this report.

[Table modified from Morgan (2021). ID, identification; Ma, mega-annum; ±, plus or minus; σ, sigma error; MSWD, mean standard weighted deviation; n/(total), indicates how many of the analyses are included in the interpreted age; NA, not available]

Sample ID	Run ID	Material	Easting	Northing	Map Unit Symbol	Preferred sample age Age (Ma) ± error (2σ)	Plateau		Isochron				Integrated	Juvenile Population Weighted Mean		
							Age (Ma) ± error (2σ)	MSWD	Age (Ma) ± error (2σ)	MSWD	n/(total)	$^{40}Ar/^{36}Ar$	Age (Ma) ± error (2σ)	Age (Ma) ± error (2σ)	MSWD	n/(total)
RP15-8	2596-01	Whole rock	492311	3470889	Tnb	13.620±0.055	13.620±0.055	1.46	13.43±0.18	39	9/(9)	306±17	13.47±0.15	NA	NA	NA
KTSC18-31	2707	Sanidine	491436	3480704	Tat	23.986±0.027	NA	NA	NA	NA	NA	NA	NA	23.986±0.027	17.73	32/(35)
KTSC18-08	2706	Sanidine	491390	3472115	Tat	24.112±0.025	NA	NA	NA	NA	NA	NA	NA	24.112±0.025	11.5	40/(40)
RP-18-1	2708	Sanidine	492107	3473798	Tat	24.129±0.035	NA	NA	NA	NA	NA	NA	NA	24.129±0.035	48.4	13/(35)
KTSC18-09	2597-01	Whole rock	490853	3474671	Tmp	25.68±0.19	NA	NA	25.55±0.19	40	9/(9)	304.3±4.8	25.68±0.19	NA	NA	NA
KTSC19-06	2598-01	Whole rock	490224	3478729	Tmp	26.26±0.71	NA	NA	26.7±1.0	620	9/(9)	286±21	26.26±0.71	NA	NA	NA
KTSC19-04	2713-01	Biotite	491811	3485947	Tat	26.443±0.084	26.443±0.084	1.63	26.41±0.12	3.4	18/(18)	309±21	26.454±0.091	NA	NA	NA
KTSC19-04	2714-01	Hornblende	491811	3485947	Tat	NA	26.76±0.40	0.31	26.80±0.49	0.37	10/(11)	293±46	26.76±0.40	NA	NA	NA
KTSC19-01	2710-01	Biotite	490130	3499019	Tat	26.47±0.11	26.47±0.11	0.53	26.67±0.24	0.79	22/(24)	282±18	26.47±0.11	NA	NA	NA
KTSC19-05	2715-01	Biotite	489875	3486677	Tv	26.473±0.095	26.473±0.095	1.03	26.34±0.22	2.4	16/(18)	337±45	26.48±0.11	NA	NA	NA
KTSC19-05	2716-01	Hornblende	489875	3486677	Tv	NA	26.65±0.51	0.48	27.07±0.72	0.29	10/(11)	243±72	26.65±0.51	NA	NA	NA
KTSC19-05	2716-02	Hornblende	489875	3486677	Tv	NA	26.54±0.48	0.68	25.4±1.7	0.41	5/(8)	470±230	26.54±0.48	NA	NA	NA
KTSC19-03	2711-01	Biotite	487314	3497151	Tat	26.601±0.095	26.601±0.095	1.42	26.93±0.20	5	16/(18)	258±19	26.58±0.16	NA	NA	NA
KTSC19-03	2712-02	Hornblende	487314	3497151	Tat	NA	26.50±0.34	0.38	26.62±0.44	0.4	13/(13)	260±100	26.50±0.34	NA	NA	NA
KTSC19-03	2712-01	Hornblende	487314	3497151	Tat	NA	26.42±0.27	0.37	26.53±0.72	0.29	11/(16)	240±300	26.42±0.27	NA	NA	NA

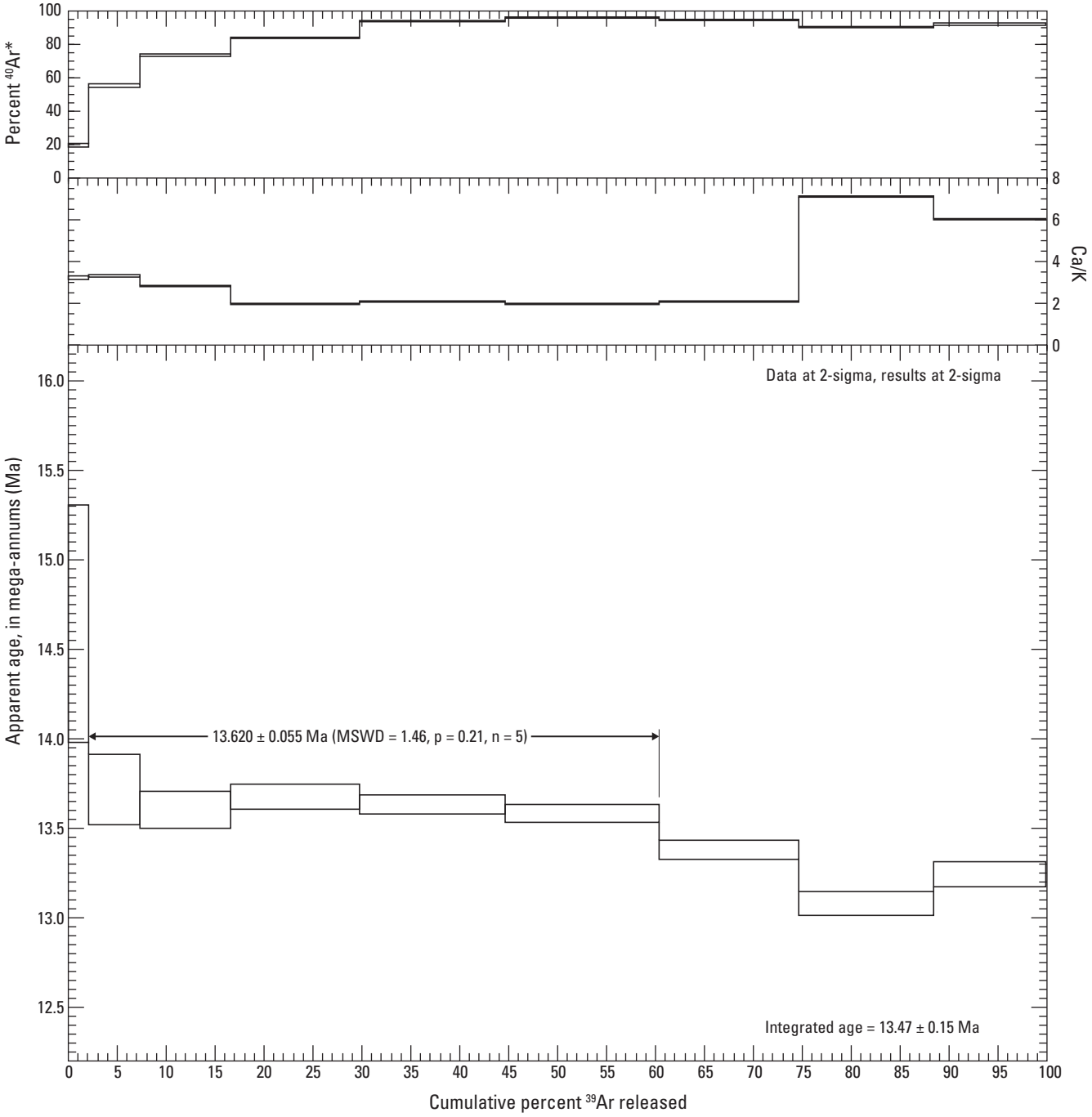

Figure 3. Plot of $^{40}Ar/^{39}Ar$ geochronology incremental heating data for whole rock analysis of Nogales Formation basalt. Apparent age shown in mega-annum (Ma); %, percent; MSWD, mean square of weighted deviates.

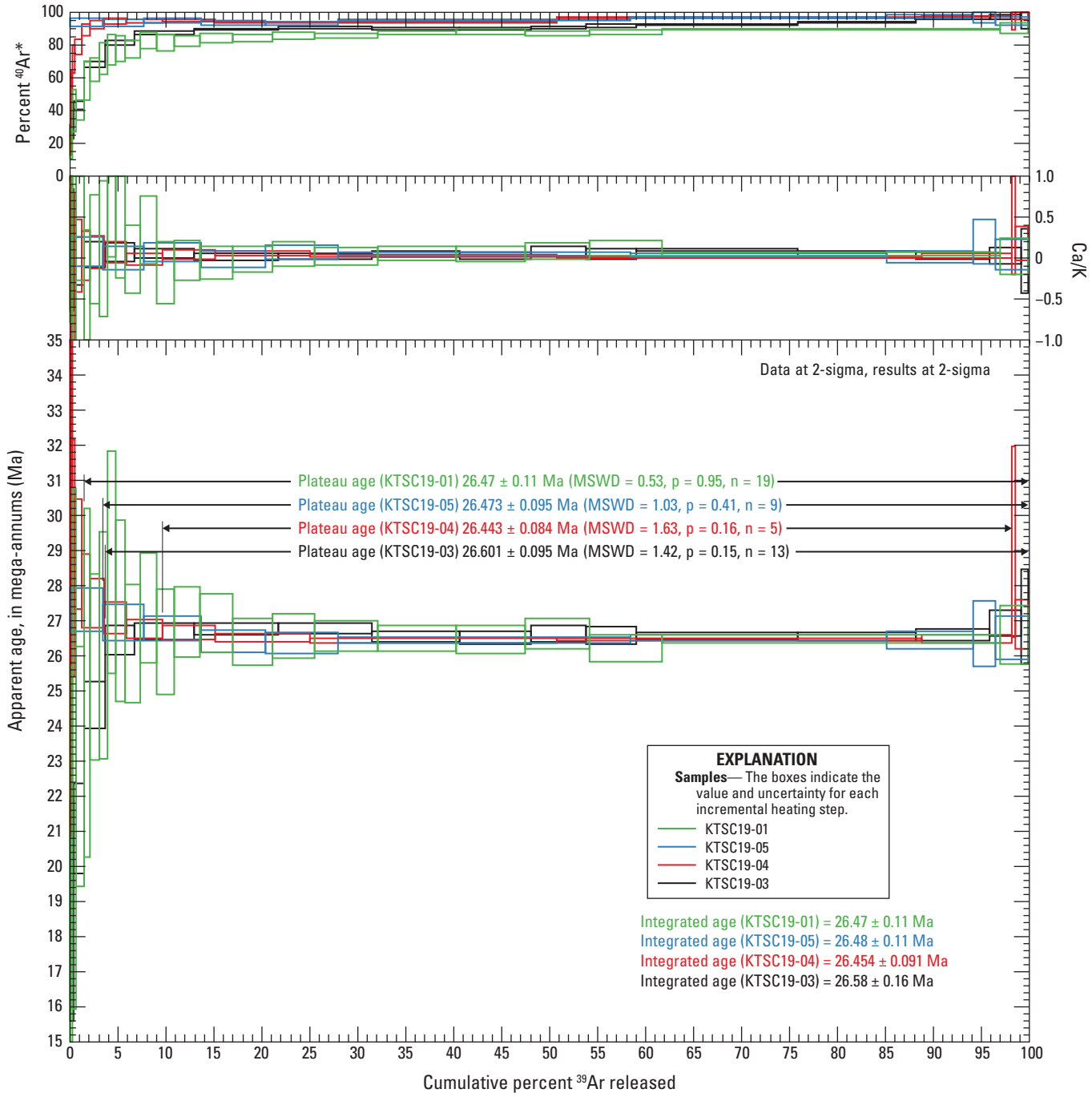

Figure 4. Plot of $^{40}Ar/^{39}Ar$ geochronology incremental heating data for biotite analyses of samples from Atascosa Formation and Atascosa and Montana Peak Formations, undivided. Apparent ages shown in mega-annum (Ma); %, percent; MSWD, mean square of weighted deviates.

Figure 5.—Following page Plot of $^{40}Ar/^{39}Ar$ geochronology single-grain, laser-fusion sanidine data for tuffs within the Atascosa Formation. Dashed lines and gray squares and triangles indicate population of grains omitted from the mean age calculation. Number of grains used in the calculation and total number of grains analyzed are reported in table 1. Apparent ages shown in mega-annum (Ma); %, percent; MSWD, mean square of weighted deviates.

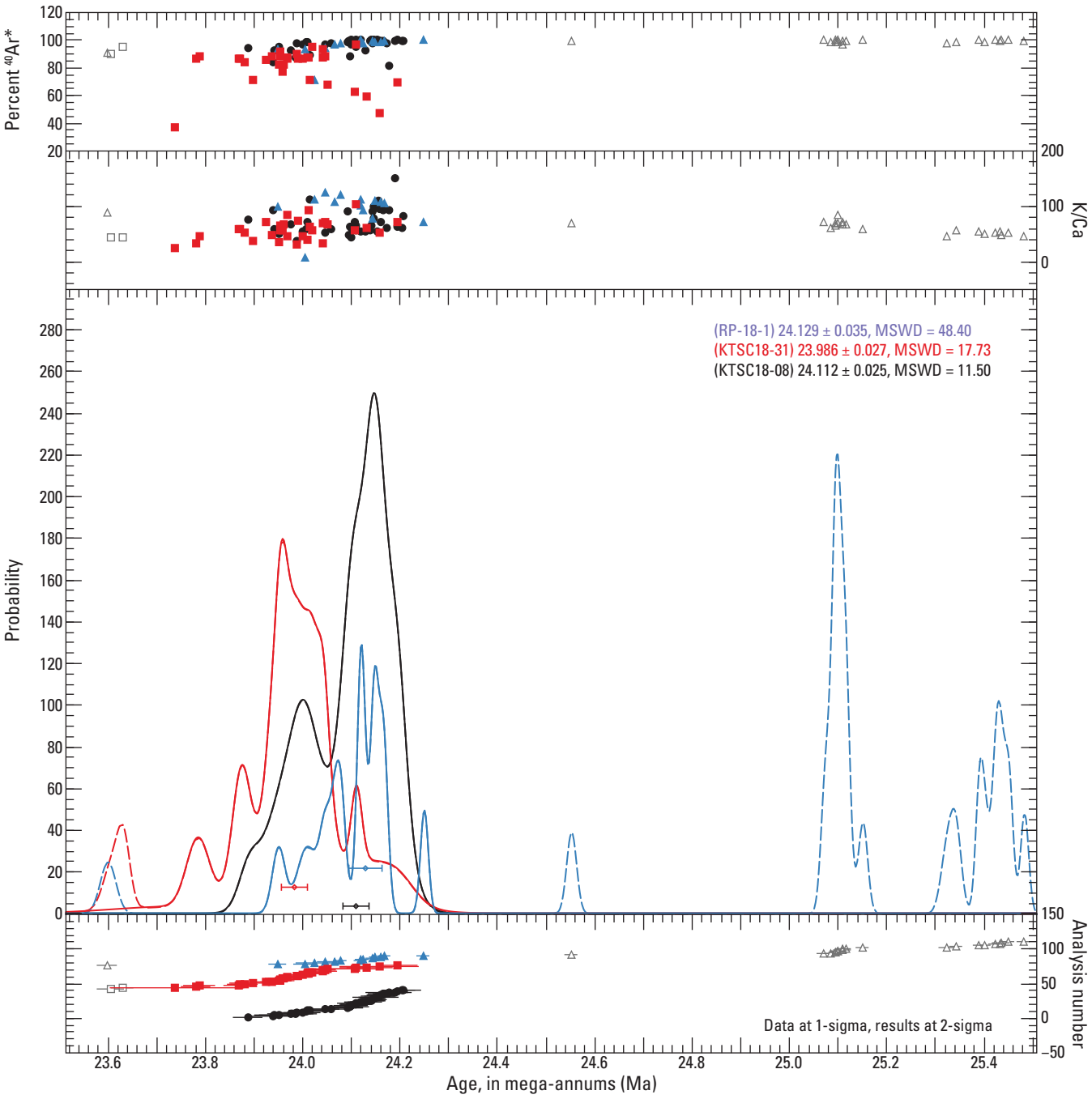

EXPLANATION

Sample age probability—Solid line indicates probability function for analyses used in calculating the weighted mean age. Dashed line indicates probability function including ages omitted from the age calculation

- RP-18-1
- KTSC18-31
- KTSC18-08

Single-crystal analysis age—Solid symbols indicate analyses used in the weighted mean age calculation. Open gray symbols indicate analyses omitted from the calculation. Line lengths indicate uncertainty in the age reported at 1 sigma

- RP-18-1
- KTSC18-31
- KTSC18-08

Weighted mean age of the sample—Line lengths indicate uncertainty in the weighted mean age calculation reported at 2 sigma

- RP-18-1
- KTSC18-31
- KTSC18-08

Single-crystal age relative to K/Ca value and percent radiogenic ^{40}Ar—Solid symbols indicate analyses used in the weighted mean age calculation. Open gray symbols indicate analyses omitted from the calculation

- RP-18-1
- KTSC18-31
- KTSC18-08

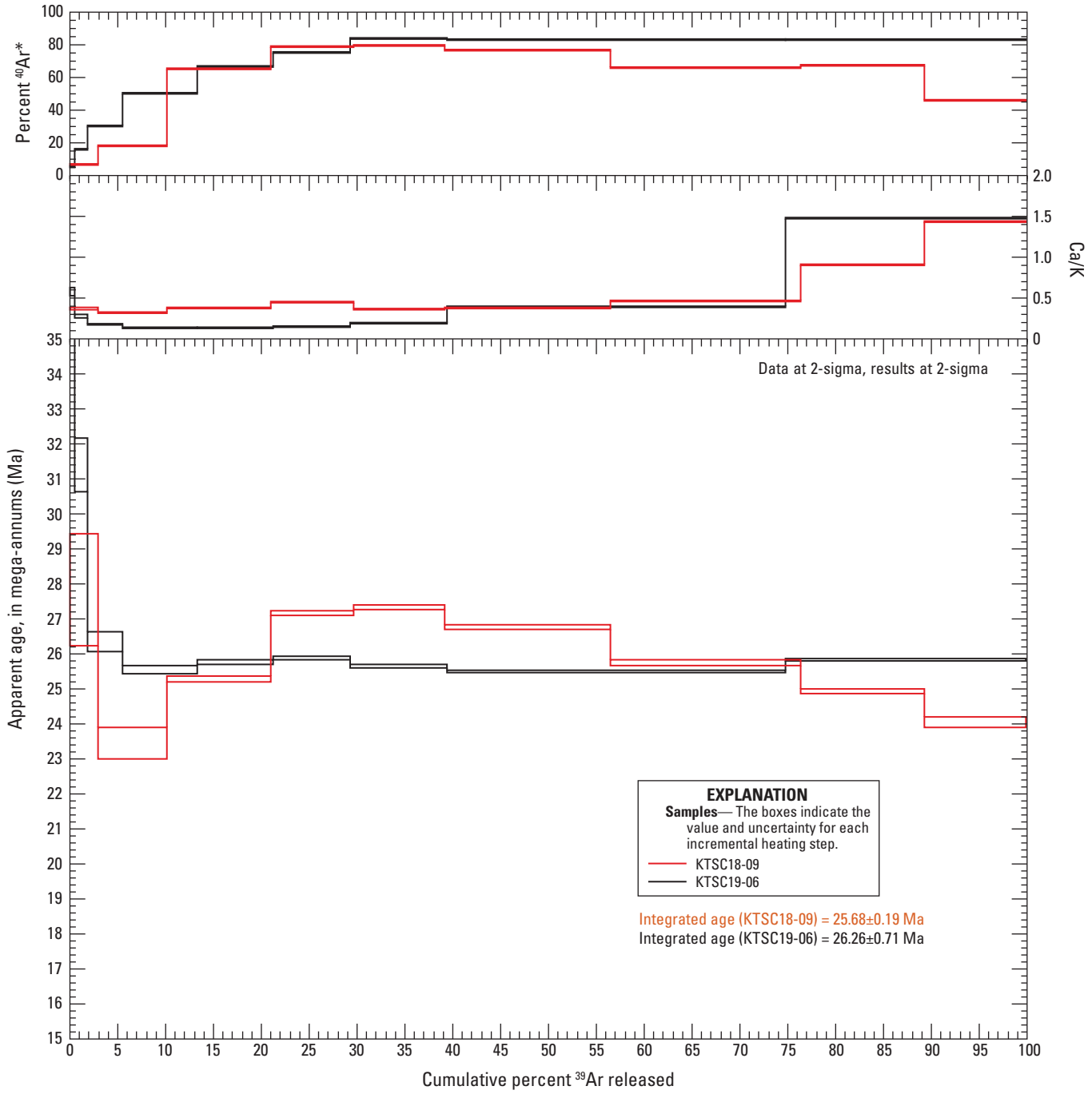

Figure 6. Plot of $^{40}Ar/^{39}Ar$ geochronology incremental heating data for whole rock analyses of lava flows within the Montana Peak Formation. Apparent ages shown in mega-annum (Ma); %, percent; MSWD, mean square of weighted deviates.

DESCRIPTION OF MAP UNITS

RIVER DEPOSITS

Qycr **Active river channel deposits (latest Holocene)**—Modern river-channel deposits of Youberg and Helmick (2001). Alluvium transported and deposited by discrete channel systems during the past several years to decades. Unit mapped along Santa Cruz River and sections of Nogales Wash, Sonoita Creek, and Sopori Wash. Channels are anastomosing to braided systems of small subchannels and low bars (local relief as much as 1−2 meters [m]) within a larger discrete meandering channel belt up to tens of meters wide. In urbanized areas of Nogales, from the diversion tunnel north of the international border to the Mariposa Canyon area, channel of Nogales Wash is artificially restrained within concrete abutments. Deposits are composed of unconsolidated, poorly to moderately sorted, weakly to moderately bedded, and interstratified silt, fine to coarse sand, and pebble-, cobble-, and locally small-boulder gravel. Clasts rounded to subangular. No soil development other than very thin (≤1−2 centimeters [cm]) surface crusts composed of silt and very fine sand in channel reaches that have not had recent flows. Most reaches currently experience discontinuous, intermittent to ephemeral flow, except for Nogales Wash and nearby downstream reaches of the Santa Cruz River that receive limited perennial discharge from south of the international border at Nogales. Many channels locally contain sparse to dense riparian vegetation. Most large channels are prone to moderate to extreme flow discharges during prolonged or intense precipitation events. Larger flooding episodes commonly are associated with major sediment transport, deposition, and local erosion within channels and adjacent lowland areas. Estimated thickness 2−6 m

Qyr **Young river floodplain and terrace deposits, undifferentiated (Holocene)**—Holocene floodplain and terrace deposits of Youberg and Helmick (2001). Alluvial deposits associated with floodplain and low-level river terraces flanking main channels on valley floors of major drainages. Locally includes active channel deposits too narrow to map separately. Unit mapped along sections of the Santa Cruz River, Nogales Wash, Sonoita Creek, and Sopori Wash. Terrace surfaces generally 1–5 m above adjacent active channels. Much of the most recent valley incision is related to pronounced arroyo incision that initiated in the late 1880s along all major drainages in the region (Betancourt, 1990; Wood and others, 1999). Deposits composed of unconsolidated to weakly consolidated, poorly to moderately sorted, poorly to moderately bedded, and interstratified sand, silt, and pebble-, cobble-, and locally small-boulder gravel, with a larger percentage of fine-grained components in the upper part of the unit. Clasts rounded to subangular. Original depositional surfaces artificially altered to varying degrees by agricultural development or urbanization. Unit subdivided into Qyr2 and Qyr1 where more than one set of Holocene terrace deposits are discernible. Estimated thickness 2−6 m

Qyr2 **Young river floodplain and terrace deposits (late Holocene)**—Alluvial deposits associated with flat to gently undulating (local relief generally <50 cm) low floodplain surfaces, many abandoned after post-1880s arroyo cutting, and one or more higher terraces 1–2 m above adjacent active channels. Surfaces typically extensive and undissected, with little to no natural post-depositional modification. Occasionally flooded. Soil development incipient to weakly developed A/C profiles. Estimated thickness 2−6 m

Qyr1 **Young river terrace deposits (Holocene)**—Alluvial deposits associated with low-level river terraces 2–5 m above adjacent active channels and 1–3 m above lower Qyr2 terraces. Surfaces have not received discharge or alluvial

sediment in the past several decades to millennium. Natural surface modification limited to some smoothing of original depositional surfaces and development of light varnish on surface clasts. Incipient to weak soil development to depths of 1−1.5 m. Soils on the highest (oldest) terraces characterized by A or Av, Bw, and Bk horizons with stage I carbonate morphology. Estimated thickness 2−6 m

Qlyr **Young to young-intermediate river terrace deposits (Holocene to late Pleistocene)**—Holocene to late Pleistocene river terraces of Youberg and Helmick (2001). Alluvial deposits associated with low-intermediate level river terraces generally 5–11 m above active channels, mapped along sections of Santa Cruz River mostly north of Peck Canyon. Deposits are composed of unconsolidated, poorly sorted, poorly bedded, and interstratified sand, gravelly sand, and sandy pebble-, cobble-, and minor boulder-gravel. Clasts subangular to rounded. Surfaces flat to gently sloping with minor low-relief dissection, and typically veneered by younger (Holocene) fine-grained alluvium not mapped separately. Original depositional surfaces locally altered to varying degrees by urbanization. Soil development in terrace deposits characterized by reddened Bt horizons and Bk horizons with stage I–II carbonate morphology. Estimated thickness 2−6 m

Qlr **Young-intermediate river terrace deposits (late Pleistocene)**—Late Pleistocene river terraces of Youberg and Helmick (2001). Alluvial deposits associated with intermediate-height river terraces preserved along valley margins of major drainages. Mapped along sections of the Santa Cruz River, Nogales Wash, Sonoita Creek, and Sopori Wash. Locally forms two sets of terraces not mapped separately, one at heights of 8–15 m and the other at heights of 10–25 m above adjacent channels. Along the Santa Cruz River north of Rio Rico, main Qlr terraces are typically 16–20 m above the active channel. Deposits are composed of unconsolidated, poorly sorted, poorly bedded, and interstratified sand, gravelly sand, and sandy pebble-, cobble-, and minor boulder-gravel. Clasts subangular to rounded. Terrace surfaces flat to gently sloping with minor to moderate dissection. Artificial alteration by urbanization common, and particularly extensive along Interstate 19 (I–19), which north of Tubac is largely built on Qlr terrace surfaces. Weak to moderate physical weathering of surface clasts. Where not disturbed by urbanization, pavement weakly to moderately developed with varnish that imparts orange to reddish-brown coloration to terrace surfaces in outcrop and on NAIP orthophotography and imagery viewed with Google Earth. Moderate soil development, to depths of 1–1.5 m, characterized by distinct Av horizons, weak to moderately developed Bt horizons, and Bk horizons with stage I–II carbonate morphology. Estimated thickness 3−6 m along the Santa Cruz River and 1−3 m elsewhere

Qmr **Older-intermediate river terrace deposits (middle Pleistocene)**—Middle Pleistocene river terrace deposits of Youberg and Helmick (2001). Alluvial deposits associated with scattered remnants of high-level terraces. Preserved in a few places along the Santa Cruz River, where terrace remnants are 24–28 m above the active channel, and along Sonoita Creek, where deposits form accordant series of broad, rounded, isolated benches, 5–10 m wide and about 30–40 m above the active channel. Deposits are composed of unconsolidated, poorly sorted, poorly bedded, and interstratified sand, gravelly sand, and sandy pebble-, cobble-, and minor boulder-gravel. Clasts mainly subangular to rounded. Remnant surfaces artificially altered where crossed by I–19 along the Santa Cruz River valley. Natural surfaces, where preserved, typically have moderate to strong modification of original morphology, with moderate to locally strong pavements that subsequently have been partially stripped, moderate to strong physical clast weathering, and moderate to strong varnish on surface clasts. Varnish on surface clasts imparts

dark-reddish-orange to brown coloration to terrace surfaces in outcrop and on color photographic imagery. Locally eroded, moderately to strongly developed soils, about 1–2 m thick, characterized by well-developed, clay-rich Bt horizons, and Bk and cemented K horizons with stage II+ and III+ carbonate morphology, respectively. Estimated thickness up to 10−12 m along the Santa Cruz River and 1−3 m along Sonoita Creek

ALLUVIAL AND BASIN-FILL DEPOSITS

Qy **Young alluvial deposits, undifferentiated (Holocene)**—Undifferentiated Holocene alluvium of Youberg and Helmick (2001) and Lindsey and Van Gosen (2005). Alluvial deposits associated with channels, adjacent floodplains, low terraces, and small alluvial fans along tributary drainages, and narrow alluvial plains at the toe of piedmont slopes along the Santa Cruz River valley margin. Most surfaces 0.5–3 m above active local channels. Lower surfaces rarely to occasionally flooded within decadal to millennial time scales by high-discharge runoff during extreme precipitation events, whereas higher surfaces rarely if ever inundated. Deposits composed of unconsolidated to very weakly consolidated, poorly to moderately sorted, poorly bedded, and interstratified sand, silt, and pebble- to cobble-gravel, with an increase in fine-grained sediment near the top of the unit. Locally contains a few scattered small boulders. Clasts rounded to subangular. Clast size and relative abundance typically decrease downstream from mostly sandy pebble-cobble gravel in upland reaches to sand and pebbly gravel in distal reaches. Unit subdivided into Qy2 and Qy1 where more than one set of Holocene alluvial deposits are discernible. Thickness commonly 2−3 m

Qy2 **Younger of young alluvial deposits (late Holocene)**—Late Holocene alluvium of Youberg and Helmick (2001). Deposits associated with channels, adjacent floodplains, lowest terraces, and small alluvial fans along tributary drainages. Forms surfaces mostly 0.5–2 m above active local channels. Surfaces generally flat to gently undulating, and undissected with minimal or no modification of original depositional surface. No to very weak soil development, limited to thin fine-grained A horizons developed on some terrace surfaces. Thickness commonly 2−3 m

Qy1 **Older of young alluvial deposits (Holocene)**—Holocene alluvium of Youberg and Helmick (2001) and Lindsey and Van Gosen (2005). Deposits associated with low terraces locally preserved along margins of incised tributary valleys at heights of 2–3 m above active channels; also may include small fan remnants near canyon mouths of tributary drainages. Surfaces generally flat to gently undulating with minor dissection by widely spaced shallow rills. Some smoothing of original depositional surfaces, poorly preserved bar-and-swale morphology, and incipient pavement development. Some surface clasts physically weathered and (or) lightly varnished. Very weak to weak soil development, about 1–1.5 m deep, characterized by Av, Bw, and Bk horizons with thin stage I carbonate morphology. Thickness commonly 2−3 m

Qly **Young and young-intermediate alluvial deposits, undifferentiated (Holocene and late Pleistocene)**—Alluvial deposits associated with channels, alluvial fans, sheetwash, and low and intermediate-height terraces; mapped in headwater regions of tributary drainages. Deposits composed of mostly unconsolidated, poorly sorted, poorly bedded, sand, gravelly sand, and sandy pebble- and cobble-gravel. Clasts mainly subrounded to subangular. Estimated thickness 0.5−3 m

Ql **Young-intermediate alluvial deposits, undifferentiated (late Pleistocene)**—Late Pleistocene alluvium of Youberg and Helmick (2001) and Lindsey and Van Gosen (2005). Deposits associated with intermediate-height terraces and alluvial fans along tributary drainages and on piedmont slopes along the

Santa Cruz River valley margin. Top of unit commonly projects to, or grades to top of unit Qlr. Deposits of unit Ql typically overlie older sediments or bedrock. Surfaces flat to gently undulating benches at heights of 5–25 m above adjacent channels. Deposits are composed of unconsolidated, poorly sorted, poorly bedded, and interstratified sand, gravelly sand, and sandy gravel. Clasts mainly subrounded to subangular and range in size from pebbles to cobbles, with local scattered small boulders. Varnish on surface clasts imparts an overall orange to reddish brown coloration to surfaces in outcrop and color photographic imagery. Unit subdivided into Ql2 and Ql1 where more than one set of late Pleistocene alluvial deposits are discernible. Commonly 2−3 m thick

Ql2 **Younger of young-intermediate alluvial deposits (late Pleistocene)**—Latest Pleistocene member of Youberg and Helmick (2001). Forms benches 5–10 m above adjacent channels on valley floors of tributary drainages. Surfaces slightly dissected by widely spaced gullies and rills 1–2 m deep. Original surface morphology slightly to moderately modified by development of weak to locally moderate pavement, light-toned orange to pale-red varnish, and weak to locally moderate physical clast weathering. Moderate soil development, to depths of 1–1.5 m, characterized by distinct Av horizons, weakly to moderate developed Bt horizons, and Bk horizons with stage I–II carbonate morphology. Commonly 2−3 m thick

Ql1 **Older of young-intermediate alluvial deposits (late Pleistocene)**—Late Pleistocene member of Youberg and Helmick (2001). Forms benches 12–25 m above adjacent channels in valley floors of tributary drainages. Surfaces characterized by broad, gently rounded to locally flat interfluves interspersed with widely spaced gullies and rills 2–5 m deep. Original depositional surface modified by weak to moderate pavement development, moderate to locally strong reddish brown to orange varnish, and weak to moderate physical clast weathering. Generally moderate soil development, to depths of 1–1.5 m, characterized by distinct Av horizons, weakly to moderately developed Bt horizons, and Bk horizons with stage I–II+ carbonate morphology. Commonly 2−3 m thick

Qm **Older intermediate alluvial deposits (middle Pleistocene)**—Middle Pleistocene alluvium of Youberg and Helmick (2001) and Lindsey and Van Gosen (2005). Deposits preserved mainly as isolated and scattered erosional remnants of high-level terraces and alluvial fans related to tributary drainages. Surfaces typically strongly dissected, with broad, rounded interfluves, and benches at relative heights of 10–30 m above incised tributary channels. Deposits are composed of unconsolidated, poorly sorted, poorly bedded, and interstratified sand and gravel. Clasts mainly subangular to rounded, and range in size from pebbles to cobbles with scattered small boulders. Moderate to strong modification of original surface morphology, with moderate to locally strong pavements that subsequently have been partially stripped, moderate to strong physical clast weathering, and moderate to strong varnish on surface clasts. Varnish on surface clasts imparts dark reddish-brown or orange-brown coloration to surfaces in outcrop and on color photographic imagery. Locally eroded, moderately to strongly developed soils, about 1–2 m thick, characterized by well-developed, clay-rich Bt horizons, and Bk and cemented K horizons with II–III+ carbonate morphology, respectively. Thickness 10−20 m in Josephine Canyon (Lindsey and Van Gosen, 2010), and typically 0.5−5 m elsewhere

Qo **Old alluvial deposits (early Pleistocene)**—Early Pleistocene alluvium of Youberg and Helmick (2001) and Lindsey and Van Gosen (2005). Alluvial-fan deposits preserved mainly as high, isolated erosional remnants overlying basin-fill deposits (unit QTa) and bedrock. Best preserved north of Rio Rico on the upper piedmont east and west of the Santa Cruz River. Deposits are

composed of weakly to moderately consolidated, poorly to moderately bedded, sandy gravel and gravelly sand. Clasts typically subrounded to subangular, and range in size from pebbles to boulders. Clasts are derived locally from adjacent highlands. Original surface is strongly modified and only partially preserved, with some erosional remnants of moderately to strongly varnished surface clasts on partially stripped former pavements. Locally preserved surface soil is characterized by a strongly developed, dark red and heavily clay-enriched Bt horizon above a well cemented K horizon with stage IV–V carbonate morphology, which includes laminar carbonate at the top of the K horizon. Thickness commonly 10−20 m (Lindsey and Van Gosen, 2010); locally only 1−2 m thick above exposures of gently westward sloping basal contact

QTa **Alluvial basin fill (early Pleistocene? to latest Miocene)**—Early Pleistocene to Pliocene alluvium of Youberg and Helmick (2001) and Lindsey and Van Gosen (2005). Deposits of basin-fill sediment overlying Nogales Formation and bedrock units. Unit consists of stratified sequences of mostly alluvial-fan deposits that are deeply eroded and dissected into a series of ridges and ravines (ballena topography), with local relief of 10–70 m. No original depositional surfaces are preserved. Deposits are composed of light-reddish-brown, and pinkish-gray to light-gray, weakly consolidated, moderately to poorly bedded, and interstratified sandy gravel and gravelly sand. Locally includes finer-grained sections of mostly sand and pebbly sand. Bedding contacts diffuse to gradational in character. Clasts commonly subangular to subrounded, and range in size from pebbles to cobbles. Clasts are composed of various rock types exposed along basin margins. Volcanic rock types, including rhyolite, rhyodacite, and dacitic flows and tuffs, are most common, but some sections, especially near the base of unit, contain large amounts of granitic clasts in areas near exposed granitic bedrock. Vertical exposures of unit erode to form characteristic shallow vertical fluting that crosscuts bedding. Bedding dips are typically shallow and oriented in a basinward direction. Generally, few fractures, faults or bedding partings are present in most exposures. Unit differentiated from sediments of the underlying Nogales Formation based on weak induration, diffused bedding, vertical fluting in outcrop, and general absence of deformation. The exception is the basal part of the unit, which has local internal faulting, and is slightly more indurated and has greater stratal tilt relative to sediments higher in the unit. Basal part of unit QTa is faulted against the informally named Mariposa member of Nogales Formation along I–19 south of Potrero Creek; along the Rio Rico fault on the west flank of the San Cayetano Mountains, where unit QTa in the hanging wall is faulted against Salero Formation in the footwall; and at Crawford Hill where unit QTa is faulted against the Nogales Wash member (informal name) of the Nogales Formation. Thickness of unit poorly constrained, but exposed sections, combined with subsurface estimates based on geophysical and borehole data, suggest thicknesses of 50–100 m; possibly as much as 150 m thick in deeper subbasins

NOGALES FORMATION (MIOCENE)

Modified from Page and others (2016b). Exposed mostly in the Rio Rico and Nogales 7.5′ quadrangles where it includes (from top to base) the Mariposa, Nogales Wash, and Proto Canyon members (Page and others, 2016b). Also exposed in the Agua Fria Canyon area in the Peña Blanca Lake and Pajarito Peak 7.5′ quadrangles, and in scattered outcrops along the northwest flank of the Santa Rita Mountains in the San Cayetano and Mount Hopkins 7.5′ quadrangles. Maximum age of formation is about 20 to 18 Ma, and minimum age is about 11 Ma (Cosca and others, 2013; Houser and others, 2004; and Page and others, 2016b); thickness ranges from 80 to 950 m thick in map area

Tnu **Nogales Formation, undivided (Miocene)**—Includes deposits of the formation present primarily along the basin margins, between mountain range fronts and deeper sub-basins within the Metropolitan Nogales area, where individual members of the formation defined in the Rio Rico and Nogales 7.5′ quadrangles (Page and others, 2016b) are not recognized. Consists of moderately consolidated volcaniclastic conglomerate, sandstone and siltstone and some claystone, and some tuff beds. Thickness from about 80 to 250 m thick

Tnb **Nogales Formation basalt (middle Miocene)**—Present in the upper part of the formation. Exposed in the Mariposa member in the southernmost Nogales 7.5′ quadrangle, where flows are 3 to 5 m thick and consist of medium-dark-gray olivine basalt, dated at 11.67±0.09 Ma (Cosca and others, 2013; Page and others, 2016b). Other basalt flows are exposed in the Agua Fria Canyon area, and locally in the Pajarito Mountains area (Drewes, 1980). Basalt flows in the Agua Fria Canyon area are about 10 to 20 m thick and yielded dates of 13.65±0.11 Ma and 13.64±0.11 Ma, respectively (Cosca and others, 2013, Page and others, 2016b). Olivine basalt flows are also exposed in lower Walker Canyon, in the Pajarito Mountains, where they are up to 20 m thick; a whole rock $^{40}Ar/^{39}Ar$ sample yielded an age of 13.65±0.10 Ma (RP15–8, table 1, fig. 6), which is within analytical uncertainty of the basalt sample in Agua Fria Canyon

Tnt **Nogales Formation tuff (lower to middle Miocene)—**Includes white tuff beds near the base (generally within 20 to 30 m above base) of the formation exposed in Agua Fria and Walker Canyons. Laser fusion $^{40}Ar/^{39}Ar$ geochronology on plagioclase grains for the Agua Fria Canyon basalt yielded a mean age of 18.4±1.5 Ma (Cosca and others, 2013; Page and others, 2016b). Maximum thickness about 20 m thick in Walker Canyon area, but generally ranges from about 3 to 10 m thick. Houser and others (2004) dated a tuff about 30 m above the base of the Nogales Formation in the Cottonwood Canyon on the northwest flank of the Santa Rita Mountains. The sample yielded two possible ages of 15.53±0.38 Ma (sanidine) and 17.38±0.77 Ma (whole rock). Correlation of this tuff with the Agua Fria Canyon tuff is unclear, although both tuffs were deposited near the same stratigraphic position suggesting they may be partly correlative

Tnm **Mariposa member (upper Miocene)**—Widely exposed and defined in the Nogales and Rio Rico 7.5′ quadrangles (Page and others, 2016b). Consists mostly of grayish-orange-pink to pinkish-gray alternating beds of volcaniclastic, calcareous, conglomerate and sandstone. Member locally contains grayish-orange-pink claystone unit in Mariposa Road area (between Grand Avenue and I–19); about 30 to 40 m of unit is exposed, but total thickness estimated at 60 m or more. Claystone unit gradational with overlying sandstone and conglomerate. In basin south of Sonoita Creek and east of Santa Cruz River, member contains units like those in urban Nogales, but conglomerate and sandstone is less coarse, and units represent a finer-grained facies, consisting of alternating beds of fine-grained, volcaniclastic sandstone, siltstone, and claystone. Along the international border in the southeastern part of the map, only lower part of Mariposa member is exposed and consists of grayish-orange, volcaniclastic conglomerate with mostly subangular, light-brownish-gray porphyritic volcanic clasts. In this area, member contains thin discontinuous, medium dark gray, olivine basalt flows (3 to 5 m thick) and have a $^{40}Ar/^{39}Ar$ age of 11.67±0.09 Ma (Cosca and others, 2013). Member is generally about 80–100 m thick, but maximum thickness is estimated to be 350 m in deeper basins

Tnn **Nogales Wash member (middle to upper Miocene)** —Only exposed in Nogales 7.5′ quadrangle south of Mariposa Road, and along the international border from Ephraim Canyon to about 4 km east of Grand Avenue. Member is mostly pinkish-gray, yellowish-gray, and grayish-orange-pink

volcaniclastic sandstone, conglomeratic sandstone, and minor siltstone and claystone. Beds typically contain tabular planar crossbeds, and few show mudcracks, bioturbation, and leaf impressions. Basal thickness of 20 to 30 m forms distinctive massive cliffs composed of pinkish-gray volcaniclastic sandstone and conglomeratic sandstone, with abundant pumice fragments. Member is moderately fractured and is disconformable with overlying Mariposa member. Thickness estimated at about 50 to 150 m

Tnp **Proto Canyon member (lower Miocene)**—Upper part consists mostly of yellowish-gray to pinkish-gray volcaniclastic sandstone and conglomerate. Middle parts of the member consist of alternating beds of yellowish-gray volcaniclastic sandstone and conglomerate; pale-red sandy and gravelly claystone; and pale-red clayey and sandy arkosic conglomerate that contains subangular clasts of monzonite. Lower part is basal conglomerate consisting mostly of grayish-red, clast-supported monzonite boulder, cobble and pebble debris-flow conglomerate which grades upward into pale-reddish-brown, weakly consolidated arkose sandstone and conglomerate with monzonite boulders, cobbles, and pebbles. In the Sonoita Creek area the Proto Canyon member consists of upper and lower parts; upper part is mostly thin-bedded, fine-grained, volcaniclastic sandstone and conglomeratic sandstone which weathers to form distinctive rounded ledges. Lower part is volcaniclastic conglomerate and sandstone with cobbles, pebbles, and grains primarily of subangular white and red porphyritic volcanic rocks, rhyodacitic to rhyolitic tuff, pumice, and some basal debris-flow conglomerate eroded mostly from the Grosvenor Hills Volcanics. Proto Canyon member is unconformably overlain by the Nogales Wash member, and by the Mariposa member where the Nogales Wash member is absent. Member thickness variable, but maximum thickness about 450 m

BEDROCK UNITS

GROSVENOR HILLS VOLCANICS (OLIGOCENE)

Rhyolitic to dacitic lava flows, welded tuffs, nonwelded tuffaceous deposits, volcaniclastic sedimentary deposits, and intrusive-extrusive rhyolite to rhyodacite laccoliths and lava domes. Units here follow Drewes (1971b, 1972) where volcanic deposits are divided into a lower rhyolite member and upper rhyodacite member. $^{40}Ar/^{39}Ar$ and K-Ar geochronology indicate eruption and emplacement ages between 23.5 and 27.8 Ma (Drewes, 1972; Page and others, 2016b)

Tghr **Rhyolite to rhyodacite intrusive-extrusive rocks**—Described as laccoliths and dikes by Drewes (1971b; 1972). However, presence of vitrophyre horizons in upper parts of Tghr in the northern part of Grosvenor Hills indicate at least some rocks represent extrusive lava domes. Dikes are more common in the central and southern parts of Grosvenor Hills where some dikes intrude west-northwest-trending faults. Phenocryst assemblage is similar to rhyodacite member and includes plagioclase, augite, hypersthene, hornblende, biotite and accessory minerals. Geochronologic age determinations include 27.3± approximately 1.3 Ma from northernmost part of Grosvenor Hills and 27.8±2.8 Ma from easternmost part of Grosvenor Hills (K-Ar, amphibole; Drewes, 1972). Page and others (2016b) report an age of 27.8±0.3 Ma ($^{40}Ar/^{39}Ar$, amphibole) for an intrusion in the southern part of the Grosvenor Hills. Unit intrudes rhyodacite member and similarity in age and phenocryst assemblage suggests unit may be at least partly coeval and may be cogenetic with rhyodacite member

Tghu **Rhyodacite member**—Includes agglomerate, lava flows, welded and nonwelded tuff. Agglomerate blocks, lava flows and welded tuffs consist of 30–40 modal percent phenocrysts with assemblage that includes plagioclase, sparse quartz, augite, hypersthene, biotite, hornblende and accessory minerals. Distinguished from rhyolite member by higher phenocryst content

and presence of pyroxene. Pumice- and lithic-bearing pyroclastic deposits southeast of the Grosvenor Hills are tentatively correlated with the rhyodacite member based on a K-Ar age of 25.3±5.1 Ma (biotite; Damon and Bikerman, 1964). Geochronologic ages range from 27.6±1.6 Ma for a lava flow in the northeast part of Grosvenor Hills (K-Ar, plagioclase; Drewes, 1972) to 23.5±0.1 Ma for a rhyolitic tuff in the southern part of Grosvenor Hills ($^{40}Ar/^{39}Ar$, biotite; Page and others, 2016b). Combined thickness of unit approximately 430 m

Tghl **Rhyolite member**—Chiefly tuff and tuff breccia, with minor agglomerate, lava flows, sandstone, welded tuff, and coarse breccia. Some tuffaceous deposits include flattened pumice and lithic fragments indicating a pyroclastic origin. Phenocryst content of lava flows 10–20 modal percent and includes plagioclase, quartz, biotite, hornblende and accessory minerals. Thickness at least 150 meters

Tv **Atascosa and Montana Peak Formations, undivided (Oligocene)**—Pyroclastic deposits, lava flows, and possibly some intrusive rocks. Unit is mapped in areas with no field observations and where distinction between the bounding units was unclear. $^{40}Ar/^{39}Ar$ age for a lava flow in the southernmost Tumacacori Mountains is 26.473±0.095 Ma (biotite; KTSC19–05, table 1), which is equivalent in age to Atascosa Formation. Stratigraphic position of the flow was uncertain and therefore is included with unit Tv

Tat **Atascosa Formation (Oligocene)**—Includes pyroclastic deposits, lava domes and flows, and intrusive rocks of generally dacite to rhyolite composition. Pyroclastic deposits that include block-and-ash, ignimbrite, and minor ash fall are dominant rock type in Atascosa and southern part of Tumacacori Mountains. In northern part of Tumacacori Mountains, lava flows increase in proportion. Lava flows commonly have basal vitrophyre composed of annealed blocks of breccia. Phenocryst assemblage varies but includes combination of plagioclase, alkali feldspar, biotite, quartz, hornblende and accessory minerals. Reported ages document a basal contact with the Montana Peak Formation that gets progressively younger to the south. Geochronologic age determinations include 26.5±1.2 Ma from a welded tuff near Corral de Piedras (near Tumacacori Peak) (K-Ar, biotite with hornblende; Damon and Bikerman, 1964). Seaman and others (1995) report $^{40}Ar/^{39}Ar$ ages ranging from 26.31±0.31 Ma (biotite) in the Cerro Colorado Mountains, north of the Tumacacori Mountains; 23.32±0.15 Ma (sanidine) for the uppermost lava flow in the Atascosa Mountains; and 25.97±0.09 and 25.52±0.26 Ma for unlocated samples in the Tumacacori Mountains. $^{40}Ar/^{39}Ar$ ages reported here include 26.601±0.095 Ma (biotite; KTSC19–03, table 1, fig.4) and 26.47±0.11 Ma (biotite; KTSC19–01, table 1, fig. 4) in the northern Tumacacori Mountains and 26.443±0.084 Ma (biotite; KTSC19–04, table 1, fig. 4) in the southern Tumacacori Mountains. In the Atascosa Mountains, single-grain laser-fusion sanidine ages (fig. 5) include 23.986±0.027 Ma (KTSC18–31, table 1) for a pumice-bearing tuff north of Romanote Canyon, and 24.112±0.025 Ma (KTSC18–08, table 1) and 24.129±0.035 Ma (RP18–01, table 1) for a pumice-bearing tuff in the Peña Blanca Lake area. Maximum thickness of about 550 m in upper reaches of Romanote Canyon where dip on beds suggests extrusive deposits of the Atascosa Formation may have filled a topographic low and about 400 m west of Tumacacori Peak

Tai **Intrusive rocks of the Atascosa Formation (Oligocene)**—Intrusive rocks in northern part of Tumacacori Mountains. Unit intrudes deposits as young as tuffs of the Atascosa Formation. Intrusive rocks identified by brecciated margins and vertical flow foliation on the interior. Phenocryst assemblage includes alkali feldspar, biotite, little or no hornblende, and little or no quartz

Tmp **Montana Peak Formation (Oligocene)**—Lava flows and pyroclastic deposits with widely variable compositions ranging from basaltic trachyandesite to rhyolite. Rhyolitic rocks are observed in areas west and northwest of Peña Blanca Lake and include pyroclastic deposits and sparse lava flows (Nelson, 1963). From Peña Blanca Lake area north to Peck Canyon, common rock type is red tuffaceous deposit that incorporates dacitic enclaves with crenulated margins suggesting possible mixing relationship. Lava flows are present throughout mapped extent and vary from fine grained with altered olivine (iddingsite) and pyroxene to porphyritic with plagioclase and pyroxene as common phenocrysts. Seaman and others (1995) report an age of 27.72±0.09 Ma ($^{40}Ar/^{39}Ar$, biotite) immediately below the contact with the Atascosa Formation near Tumacacori Peak. Total gas whole rock $^{40}Ar/^{39}Ar$ ages reported here (table 1, fig. 6) include 25.68±0.19 Ma for a porphyritic lava flow below the contact with the Atascosa Formation in Romanote Canyon (KTSC19–06) and 26.26±0.71 Ma for a fine-grained lava flow northwest of Peña Blanca Lake (KTSC18–09). Youngest ages reported for the Montana Peak Formation in the Pena Blanca area are coeval with oldest Atascosa Formation volcanism in the northern Tumacacori Mountains. Maximum exposed thickness about 360 m in southern part of Atascosa Mountains

Tlc **Sedimentary deposits (Oligocene and Eocene?)**—Conglomerate, gravel and sand; small scattered outcrops present in the Pajarito Mountains, and in the west central Santa Rita Mountains (Drewes, 1980). Generally overlies the rocks in the upper part of the Salero Formation or Grosvenor Hills Volcanics

GRANODIORITE AND MONZONITE COMPLEX OF THE PATAGONIA MOUNTAINS (PALEOCENE)

Tqmp **Quartz monzonite porphyry**—Unit mapped by Graybeal and others (2015) for outcrops in the Sycamore Canyon and Soldier Basin areas in central Patagonia Mountains. Light-gray quartz monzonite porphyry with 3 to 6 mm long plagioclase phenocrysts. Pervasive quartz-sericite-alunite-kaolinite alteration. Vikre and others (2014) report ages that range from 61.27±0.06 Ma ($^{40}Ar/^{39}Ar$ biotite) to 59.2±1.2 Ma (U-Pb, zircon)

Tg **Granodiorite**—Exposed in central part of Patagonia Mountains, and associated with mineralization and alteration zones. Most of the unit consists of stocks containing gray biotite-hornblende granodiorite. Simons (1974) reported K-Ar ages on biotite 58.3 Ma and hornblende 58.5 Ma. Also contains biotite quartz monzonite facies exposed in western part of outcrop belt. Partly equivalent to map unit Tlg of Drewes (1980)

Tbq **Biotite quartz monzonite**—Exposed in southwestern Patagonia Mountains (Graybeal and others, 2015) where it includes equigranular to porphyritic biotite quartz monzonite with some biotite. Vikre and others (2014) reported approximate U-Pb zircon date of 64 Ma and $^{40}Ar/^{39}Ar$ on biotite of 61 to 60 Ma

Tbg **Biotite granodiorite**—Exposed in the north central Patagonia Mountains (Graybeal and others, 2015) where it consists of biotite granodiorite which in places is moderately porphyritic with biotite and plagioclase phenocrysts. U-Pb zircon dates of 63–60 Ma, and $^{40}Ar/^{39}Ar$ biotite date of 60 Ma (Vikre and others, 2014)

TKgg **Gringo Gulch Volcanics (Paleocene and Upper Cretaceous)**—Exposed in the southern Santa Rita Mountains in the Sonoita Creek area (Drewes, 1971b; 1972; Simons, 1974; Graybeal and others, 2015). Upper member consists of andesitic flows, dacite-clast bearing sandstone and conglomerate, rhyolitic tuff, and tuffaceous sandstone. Lower member consists of rhyolitic tuff and tuff breccia, dacitic and rhyolitic lava flows, sandstone and conglomerate. Vikre and others (2014) reported U-Pb zircon date for the unit at 68 Ma

TKp **Latitic to dacitic porphyry (Paleocene and Late Cretaceous)**—Exposed in stocks in the northern San Cayetano Mountains, and in central Santa Rita Mountains. Consists of quartz latite to dacitic porphyry in small stocks and plugs. Dated at 61, 63, 64, and 65 Ma (Drewes, 1980)

INTRUSIVE COMPLEX OF THE SANTA RITA AND SAN CAYETANO MOUNTAINS (LATE CRETACEOUS)

Kd **Diorite and quartz diorite—**Stocks of fine to medium grained dark gray diorite and quartz diorite dated at 67 Ma, and equivalent to Josephine Canyon Diorite (Drewes, 1971b)

Kq **Quartz monzonite—**Stocks of pinkish gray medium grained quartz monzonite, equivalent to the Elephant Head Quartz Monzonite, and dated at 68, 69, and 70 Ma (Drewes, 1971b)

Kg **Granodiorite—**Stocks of gray, medium grained granodiorite; locally porphyritic and equivalent to the Madera Canyon Granodiorite dated at 68 Ma (Drewes, 1971b)

Ks **Salero Formation (Upper Cretaceous)**—In San Cayetano Mountains unit consists predominantly of red and gray conglomeritic quartzite, and greenish gray thin-bedded argillite (Drewes, 1971b). Along the Santa Cruz River, south of Sonoita Creek, unit unconformably overlies the Jurassic monzonite, and consists mostly of red to brown conglomerate and conglomeritic sandstone with pebble to boulder-size clasts. Along the west flank of the Santa Rita Mountains, Salero Formation consists of large exotic blocks of older volcanic, intrusive, and sedimentary blocks up to 1 km long in a rhyolitic matrix (Drewes, 1971b). Lipman and Sawyer (1985) interpret this deposit as representing intracaldera fill

Kfc **Fort Crittenden Formation (Upper Cretaceous)**—Small scattered outcrops exposed in the Montosa Canyon area in the northwestern Santa Rita Mountains. Includes brown and red conglomerate, sandstone, and siltstone, with minor rhyolitic tuff; generally less than 100 m thick (Drewes, 1971a)

Kbu **Bisbee Group, undivided (Lower Cretaceous)**—Exposed on the northwest flank of the Santa Rita Mountains and consists of pale red to grayish-red arkose, conglomerate, fine-grained sandstone, siltstone, and some thin beds of laminated limestone containing mollusk fragments. These rocks represent the northwestern facies of the Bisbee Group (Drewes, 1971a, 1980). About 100 to 200 m exposed

JTrvs **Volcanic and sedimentary rocks in the southeastern part of the Patagonia Mountains and northern Tumacacori Mountains (Jurassic and Triassic)**—Red volcanic conglomerate, sandstone and siltstone, and red to gray latitic to dacitic tuff, and minor rhyolitic lava (Simons, 1974). Drewes (1980) reported an imprecise zircon-lead-alpha dates of 173 to 143 Ma. Unit about 600 m thick. Also includes red mudstone, sandstone, conglomerate, and interbedded rhyodacitic rocks in the northernmost Tumacacori Mountains, about 200 m thick

Jg **Granite and quartz monzonite, undifferentiated, of the Santa Rita and Tumacacori Mountains and Mount Benedict horst block (Late Jurassic)**—We follow Drewes's (1980) mapping for the unit in the Santa Rita Mountains, Mount Benedict horst block, and northern Tumacacori Mountains (Drewes, 1980). Stocks of pinkish-gray, coarse-grained granite and quartz monzonite. Exposed in isolated outcrops near Josephine Canyon area (Santa Rita Mountains) with age dates of 160 and 148 Ma (Drewes, 1980); in the Mount Benedict area in southcentral part of map and dated at 164 and 160 Ma (Drewes, 1980), and at the northern end of the Tumacacori Mountains with age dates at 148 Ma and 145 Ma (Drewes, 1980)

GRANITIC COMPLEX OF CUMERO CANYON (LATE JURASSIC)

Unit originally named Granite of Comoro Canyon by Simons (1974) but later modified by Graybeal and others (2015). Unit names and description mostly from Graybeal and others (2015) who recognized four informal subunits based on detailed mapping and U-Pb zircon ages of 150±20 Ma, and 160±20 Ma. Simons (1974) reported an imprecise zircon-lead alpha date of 160±20 Ma. Drewes (1980) reported a similarly imprecise dates of 163 and 148 Ma for the unit in the Maggie's Canyon area in northwestern Patagonia Mountains

Jtg **Granite of Three R Canyon—**Light-gray, grayish-orange, coarse-grained granite that is pervasively sericitized and pyritized, and has a reported zircon-lead-alpha date of 160±20 Ma (Graybeal and others, 2015). Exposed in Three R Canyon area in northern Patagonia Mountains

Jcm **Porphyritic granite—**Grayish-orange, gray, brownish-gray, or pale red, fine-grained porphyritic granite, and some coarse-grained granite and syenite. Some sericite, chlorite, and epidote alteration. Several outcrops exposed west of Soldier Basin and Guajolote Peak

Jcs **Equigranular alkali syenite—**Pale-red, light-gray and grayish-orange coarse-grained equigranular alkali syenite (Graybeal and others, 2015). An imprecise zircon-lead-alpha date of 150±20 Ma was reported

Jcg **Equigranular granite—**Pale-red, light-gray coarse-grained equigranular granite. Widely exposed where it intrudes unit Yg along the western part of the Patagonia Mountains, extending from the north in the Three R Canyon area, to the southern map boundary

Jp **Tuff of Pajarito Mountains (Middle Jurassic**)—Originally described by Riggs (1985; Cobre Ridge Tuff), and Riggs and Busby-Spera (1991). Pink to purple crystal-rich ignimbrite; highly welded removing most glass shards and pumice. Phenocryst content 30 to 50 percent and assemblage includes minor altered biotite and amphibole. Unit observed in Pajarito Mountains by Riggs and Busby-Spera (1991) to contain megabreccia blocks with high degree of welding indicating an intracaldera tuff associated with the Cobre Ridge caldera. Riggs and Busby-Spera (1991) reported a modeled U-Pb zircon age at 170±5 Ma based on multiple analyses ranging from 180 to 165 Ma. Jurassic age is significantly older than 109.22±2.6 Ma K-Ar age on feldspar reported by Damon and others (1996) and Riggs (1985). Thickness estimated at least 3,000 m in Pajarito Mountains

Trm **Monzonitic rocks in the Santa Rita and Patagonia Mountains (Triassic)**—Consists mainly of stocks of dark-gray, coarse-grained monzonite and quartz monzonite, with imprecise zircon-lead-alpha dates of 184, 190, and 210 Ma (Drewes, 1980). In the northern Patagonia Mountains, unit includes stocks of light-gray monzonite porphyry, which intrude rocks of the Mount Wrightson Formation.

Trmw **Mount Wrightson Formation (Triassic)**—Exposed north of Montosa Canyon on northwest flank of the Santa Rita Mountains, in the Josephine Peak area, in central Santa Rita Mountains., and in the northern Patagonia Mountains. In Montosa Canyon area, consists mostly of rhyolitic welded tuff, some andesitic to dacitic lava flows, and eolian quartz sandstone. In Josephine Peak area, unit is about 800 m thick and consists mostly of medium-gray, porphyritic lava flows, and latitic to rhyolitic welded tuff, lava flows, and breccia. Unit is imprecisely dated at 220 Ma (zircon-lead-alpha) in this area (Drewes, 1971b, 1980). In northern Patagonia Mountains unit consists of light-gray to pale-red rhyolitic to latitic lava and tuff, and some light-greenish gray quartzite, siltstone, sandstone, and conglomerate (Simons, 1974); thickness about 600 m in Patagonia Mountains

PIPu **Permian and Pennsylvanian rocks, undifferentiated**—Unit includes lower Permian sedimentary rocks exposed on west flank of the Santa Rita Mountains including parts of the Scherrer Formation, Epitaph Dolomite, and

Colina Limestone. Scherrer Formation consists of fine-grained quartzitic sandstone and some dolomite. Epitaph Dolomite consists of gray marly dolomite and some limestone. Colina Limestone consists of dark gray, medium- to thick-bedded limestone (Drewes, 1971b, 1980). Pennsylvanian rocks include the Horquilla Limestone (Middle and Upper Pennsylvanian), exposed on western flank of the Santa Rita Mountains in Cottonwood Canyon area, and consists of fine-grained medium-bedded, light-pinkish-gray limestone generally less than 200 m thick (Drewes, 1971b, 1980)

MDu **Mississippian and Devonian rocks, undifferentiated**—Includes parts of the Escabrosa Limestone (Lower to Middle Mississippian) and Martin Formation (Upper Devonian) and exposed in Cottonwood Canyon area on the west flank of the Santa Rita Mountains. Escabrosa Limestone consists of medium-gray coarse-grained thick-bedded fossiliferous limestone, and Martin Formation contains brown dolomite, and limestone and siltstone (Drewes, 1971b, 1980). Combined unit is less than 80 m thick

Ꞓu **Cambrian rocks, undifferentiated (Upper and Middle Cambrian)**—Includes parts of the Abrigo Limestone (Middle and Upper Cambrian) and Bolsa Quartzite (Middle Cambrian). Small outcrops of the units are exposed near the Cottonwood Canyon area on the west flank of the Santa Rita Mountains. Abrigo Limestone consists of brown thin-bedded limestone, sandstone, quartzite, and shale, and Bolsa Quartzite consists of brown to white, or purplish-gray coarse-grained, thick bedded quartzite (Drewes, 1971b, 1980). Unit generally less than 25 m thick combined

Yg **Granitoid rocks (Mesoproterozoic rocks)**—Granodiorite and quartz monzonite occurring in stocks that are exposed along the western flank of the Patagonia Mountains (Drewes, 1980). Unit also exposed on northwestern side of the Santa Rita Mountains near Cottonwood Canyon

Xp **Pinal Schist (Paleoproterozoic rocks)**—Includes chlorite schist, phyllite, and some metavolcanic, metaquartzite, and gneiss (Drewes, 1980). Exposed on northwestern side of the Santa Rita Mountains near Cottonwood Canyon area.

Structural Geology

All major mapped faults in the study area are discussed in this section (fig. 7). The faults were defined by Simons (1974), Drewes (1980), Gettings and Houser (1997), Graybeal and others (2015), Page and others (2016a), and Bultman and Page (2016). Newly recognized faults (mostly concealed faults including the Santa Cruz, Atascosa, Lowell, Tumacacori, and Agua Fria Canyon faults), were mapped based primarily on interpretation of geophysical data presented in this report and in Bultman and Page (2016).

Many faults formed during Miocene crustal extensional deformation, and main episodes of extension occurred in southern Arizona from about 20 to 10 Ma (Menges, 1981; Menges and McFadden, 1981; Menges and Pearthree, 1989). Extensional deformation was broadly contemporaneous with deposition of the Nogales Formation, based on observations that all members of the formation are moderately to highly faulted, with abundant intraformational faults and fractures and moderate to steeply inclined bedding dips. Major basin-and-range extensional faulting lasted until latest Miocene time based on faults that offset the oldest post-Nogales Formation late Miocene basin-fill deposits. The youngest tectonic activity in the map area is demonstrated by some minor high-angle normal faulting of younger alluvial basin-fill (map unit QTa), old alluvial deposits (map unit Qo), older intermediate alluvial deposits (map unit Qm), and older of the young intermediate alluvial deposits (map unit Ql1) in the northern part of the map area north of Mavis Wash (sheet 1). Fault displacement of the Pleistocene deposits is small, and apparently similar to that reported by Pearthree and Youberg (2000) for the area immediately to the north, where late Pleistocene surfaces are offset about 2 m and middle and early Pleistocene surfaces are offset 4–5 m.

Mount Benedict Fault

The northwest-striking Mount Benedict fault (fig. 7) was originally described by Gettings and Houser (1997). The fault is mostly concealed by surficial deposits along the Santa Cruz River (Page and others, 2016b), and it controls the course of the river from the Rio Rico area, southward across the international border into Sonora, Mexico. The fault is exposed at several locations along the Santa Cruz River between the United States–Mexico border and Rio Rico. To the south, the fault is exposed in the southern Cumero Canyon 7.5′ quadrangle

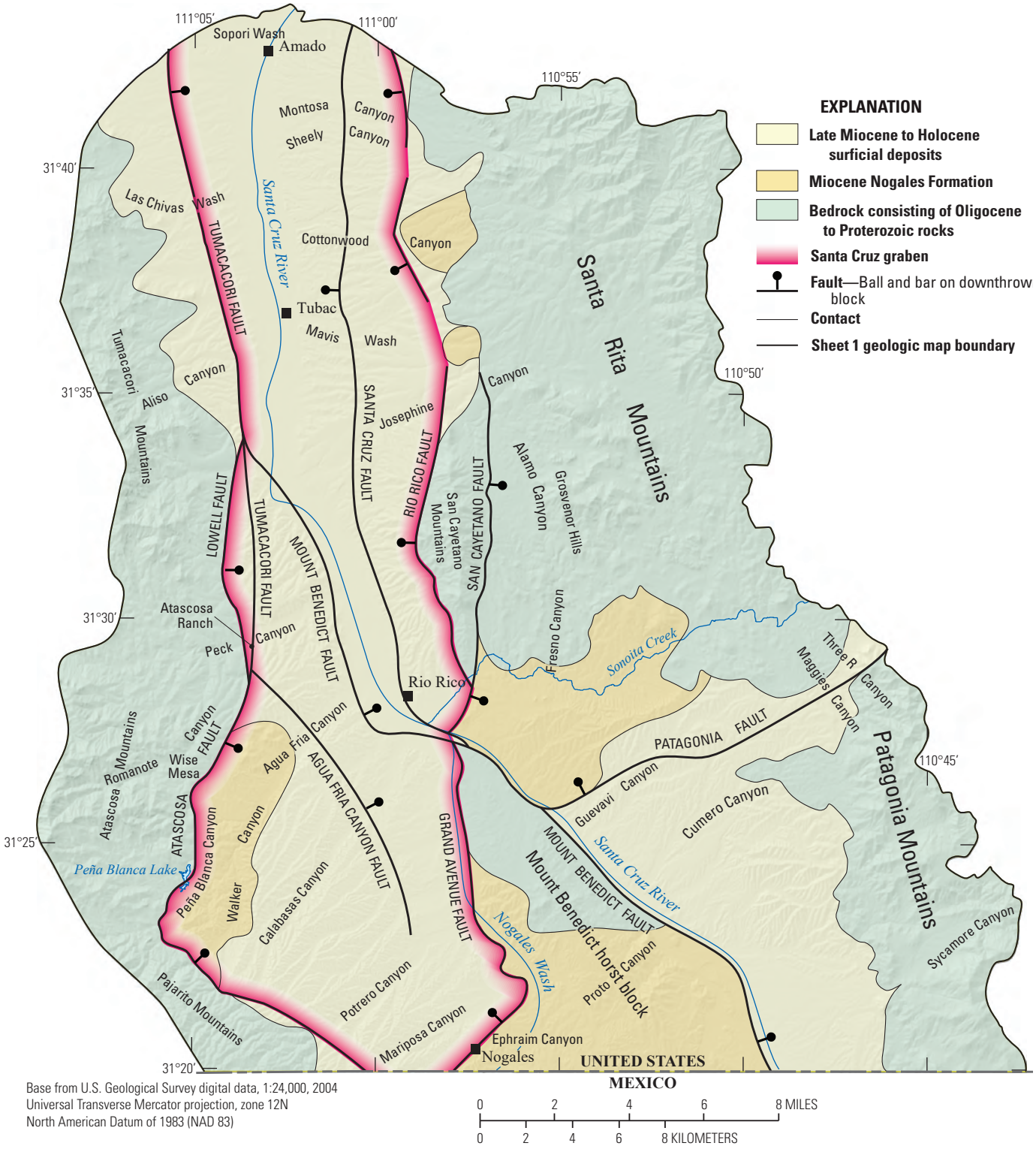

Figure 7. Index map showing major faults discussed in the "Structural Geology" section of the report. Late Miocene–Holocene surficial deposits light yellow; Miocene Nogales Formation dark yellow; and Oligocene to Proterozoic bedrock green.

southeast of the intersection of State Highway 82 and the Santa Cruz River (sheet 1 and fig. 7). In this area the fault juxtaposes red arkosic conglomerate of the Proto Canyon member of the Nogales Formation in the footwall against pinkish- to yellowish-gray volcaniclastic sandstone of the Mariposa member in the hanging wall. The Mount Benedict fault is concealed further south of these outcrops, but continues southward into Sonora, Mexico based on geophysical and geologic data.

The Mount Benedict fault is also exposed between Guevavi Canyon and Sonoita Creek (sheet 1, and Page and others, 2016b). In this area the fault downdrops sediments of the Mariposa member of the Nogales Formation against the quartz monzonite of Mount Benedict, and also some Salero Formation which unconformably overlies the monzonite locally. Near Sonoita Creek the fault is concealed but is interpreted to bend westward across the Santa Cruz River, then northward along the west side of the river to merge with the Tumacacori fault (sheet 1 and fig. 7).

Santa Cruz Fault

The Santa Cruz fault is a newly defined north-striking normal fault extending from Sonoita Creek northward for about 28 km to the northern edge of the map (sheet 1 and fig. 7). The fault is mostly concealed, and its trace was interpreted primarily from geophysical data (gravity and aeromagnetic data). To the north, however, the fault is exposed in the Montosa Canyon area (sheet 1) where originally mapped by Youberg and Helmick (2001). Our field investigations of the fault in Montosa Canyon revealed down-to-the-west movement with about 2 m offset of late Pleistocene deposits (map unit Ql1). Scarps were also observed offsetting latest Miocene to early? Pleistocene deposits (map unit QTa) just north of Montosa Canyon.

Rio Rico Fault

The Rio Rico fault (Page and others, 2016b) is a down-to-the-west range-front-fault on the west flank of the San Cayetano Mountains (fig. 7). The San Cayetano Mountains form a horst block with the Rio Rico fault on the west side and San Cayetano fault on the east side (fig. 7 and sheet 1). At its southern end the fault is interpreted to terminate into the San Cayetano fault just north of Sonoita Creek. The fault is exposed northwest of Sonoita Creek where it juxtaposes latest Miocene to early? Pleistocene basin-fill (map unit QTa) in the hanging wall against rocks of the Cretaceous Salero Formation in the footwall. At this location the fault strikes about N 35 degrees (°) W and dips 70° southwest (Page and other, 2016a). Northward along the Rio Rico fault short fault segments are exposed mostly in drainages where Cretaceous and Tertiary intrusive rocks in the footwall are juxtaposed against latest Miocene to early? Pleistocene basin-fill (unit QTa) in the hanging wall. At its northern end the fault dies out just north of the San Cayetano Mountains.

San Cayetano Fault

The San Cayetano fault of Drewes (1972) bounds the east flank of the San Cayetano Mountains horst block (fig. 7) and exhibits down-to-the-east offset. Along its northern extent the fault juxtaposes mostly Cretaceous Salero Formation rocks in the footwall against Oligocene Grosvenor Hills Volcanics, Miocene Nogales Formation sedimentary rocks, and Pleistocene to Holocene deposits in the hanging wall. Drewes (1972) estimated about 300 to 760 m of cumulative vertical displacement along this part of the fault that likely occurred following late Oligocene volcanism until after deposition of the Miocene Nogales Formation. At the southern end of the San Cayetano Mountains the fault is interpreted to bifurcate into two splays, both of which terminate into the Mount Benedict fault (sheet 1). At its northern end the fault extends north of the San Cayetano Mountains to the Mavis Wash area where it offsets rocks of the Grosvenor Hills Volcanics. The San Cayetano fault may be important in providing mountain recharge from the Grosvenor Hills southward into the Sonoita Creek drainage basin, and eventually westward into the Santa Cruz River inner valley. Nelson (2007) reported hydraulic flow data from the Sonoita Creek area indicating subsurface flow between the Fresno Canyon-Sonoita Creek confluence (sheet 1), and the Santa Cruz River, with estimated underflow rates of at least 500 acre-feet per year.

Atascosa, Tumacacori, and Lowell Faults; Range Front Fault System on West Flank of Atascosa and Tumacacori Mountains

In the western part of the map area, the major range front fault system bounding the Atascosa and Tumacacori Mountains extends from the south in the Peña Blanca Lake area, northward to likely continue across the northern boundary of sheet 1 (fig. 7). Parts of the fault were originally mapped by Drewes (1980); however, we revised the location of strands of the fault system based on our new mapping combined with interpretation of conductivity depth transforms (CDTs) derived from airborne transient electromagnetic (TEM), aeromagnetic, and gravity data presented in this report and in Bultman and Page (2016). The range front fault is well exposed in the southern part of the map area, from south of Peña Blanca Lake northward to Wise Mesa (sheet 1 and fig. 7), where it becomes concealed. We refer to this fault segment as the Atascosa fault (fig. 7), which downdrops volcanic sandstone and tuff units of the Nogales Formation in the hanging wall against Oligocene volcanic rocks (mostly Montana Peak Formation) in the footwall. North of Wise Mesa (sheet 1) the fault is concealed but is interpreted to bifurcate into two strands, a more major fault of the system equivalent to the Atascosa fault, which we refer to as the Tumacacori fault (fig. 7) and a minor western strand that we refer to as the Lowell fault (fig. 7). The Tumacacori fault is mostly concealed, however, fault scarps are observed in late Miocene to early? Pleistocene basin-fill deposits (map unit QTa on sheet 1) between Aliso Canyon to the south and Las Chivas Wash to the north (sheet 1). The fault is concealed north of Las

Chivas Wash but is interpreted to extend northward across the northern map boundary based on geophysical data (gravity, TEM, and magnetic data). The Lowell fault (fig. 7) is a splay of the Tumacacori fault and is exposed at the Atascosa Ranch in Peck Canyon (sheet 1). The fault juxtaposes Oligocene volcanic rocks (Montana Peak and Atascosa formations) in the footwall against late Miocene to early? Pleistocene basin-fill deposits in the hanging wall. The volcanic rocks are pervasively faulted and fractured (see Peck Canyon section this report and Nelson, 2007), and the fault in this area is interpreted to be an important mountain front recharge zone that supplies groundwater to the Rio Rico sub-basin and to northern parts of the upper Santa Cruz River basin in the Amado area (see the Peck Canyon section this report).

Agua Fria Canyon Fault

The Agua Fria Canyon fault is a northwest-striking high-angle normal fault that merges with the Tumacacori fault to the north in the Peck Canyon area and extends southeastward to the Alamo Canyon area in the Rio Rico 7.5′ quadrangle (fig. 7 and sheet 1). The fault is concealed at the surface and its location was mapped based on interpretation of east-west CDTs from TEM data in the area (Bultman and Page, 2016). In the Agua Fria Canyon area the fault is concealed but offsets the Miocene Nogales Formation exposed in the footwall against late Miocene to early? Pleistocene basin-fill deposits in the hanging wall (sheet 1). Near its southern end the fault forms the western boundary of a major graben structure with the Grand Avenue fault forming the eastern graben boundary (fig. 7). The fault may influence northward groundwater flow along the graben structure as it trends along a zone of low electrical conductivity and potentially high hydraulic conductivity (See “Peck Canyon” section of report).

Grand Avenue Fault

The Grand Avenue fault (fig. 7 and sheet 1) bounds the west side of the Mount Benedict horst block (fig. 7) and is concealed along much of its trace but exposed at several key locations discussed below (Page and others, 2016a). At its southern end, the fault strikes northeast and is concealed in Ephraim Canyon (sheet 1); north of the canyon, the fault is concealed, but it separates isolated outcrops of the Mariposa member of the Nogales Formation on the downthrown side from rocks of the Nogales Wash member on the upthrown side (Page and others, 2016a). Northward, the fault is exposed south of Mariposa Road and west of Grand Avenue (sheet 1), where it juxtaposes massive claystone of the Mariposa member of the Nogales Formation in the hanging wall against volcaniclastic sandstone of the Nogales Wash member in the footwall (Page and others, 2016b). North of Mariposa Road, the fault bends northwestward (sheet 1) and juxtaposes sandstone and conglomerate beds of the Mariposa member in hanging wall, against tuffaceous sandstone of the Proto Canyon member in the footwall. Northernmost exposures of the fault are near the juncture of Potrero Canyon and I–19 (Page and others, 2016b; sheet 1). Here, the fault downdrops late Miocene to early? Pleistocene basin-fill deposits in the hanging wall against west-dipping tuffaceous sandstone of the Proto Canyon member of the Nogales Formation in the footwall. Further north, the Grand Avenue fault is concealed, and hanging wall rocks of the Mariposa and Proto Canyon members in the subsurface are interpreted (based on geophysical modeling) to be progressively down-dropped northward against the quartz monzonite of Mount Benedict in the footwall, indicating significant west-side down offset (Page and others, 2016b). At its northern end, we interpret the Grand Avenue fault to terminate at the Mount Benedict fault (sheet 1). Several other faults are mapped west of the Grand Avenue fault (sheet 1) and these faults are concealed and were interpreted based on airborne TEM data and other geophysical data (Bultman and Page, 2016). The Grand Avenue fault together with faults to the west form a complex graben in the subsurface (sheet 1), and this fault system may be an important control on northward groundwater flow in deeper parts of the Nogales Wash drainage basin, from Mexico in the south northward into the Rio Rico area.

Patagonia Fault

The Patagonia fault, originally mapped by Simons (1974) and described by Bultman (2015), is a mostly concealed northeast striking fault in the southeastern map area (sheet 1 and fig. 7). The fault exhibits down-to-the-northwest offset based on scattered outcrops along the northwestern Patagonia Mountains south of State Highway 82, where the fault downdrops rocks of the Oligocene Gringo Gulch Volcanics in the hanging wall against Jurassic monzonite and granite in the footwall. Additional evidence supporting the fault location includes isolated outcrops on each side of the concealed fault about 0.75 km to the southwest, consisting of Proterozoic monzonite and granite exposed on the southeast side of the fault and Cretaceous Salero Formation on the northwest side, also indicating down-to-the-northwest movement. Just south of this location, the fault is interpreted to bend slightly to the northwest (based on gradient maxima of gravity and magnetic data of Bultman and Page, 2016) and then bends back to the southwest to continue down Guevavi Canyon. This segment of the fault offsets lower and upper latest Miocene to early? Pleistocene basin-fill units, and the location of this newly mapped fault strand is based primarily on (1) scattered exposures of the fault in Guevavi Canyon, and (2) apparent offset of lower and upper units of Late Miocene to early? Pleistocene basin-fill exposed along the fault. The fault is interpreted to terminate at the Mount Benedict fault along the Santa Cruz River. The Patagonia fault and other concealed northeast-trending faults to the northwest of the Patagonia fault, mapped by Page and others (2016b), may influence groundwater flow from mountain front recharge areas along the Grosvenor Hills and Patagonia Mountains, westward into the

Santa Cruz River inner river valley. From the inner valley the groundwater is then diverted northwestward into the Rio Rico area, as it flows along the uplifted Jurassic monzonite confining unit of the Mount Benedict horst block. These observations and interpretations are consistent with those of Nelson (2007), who reported potentiometric surface contour maps indicate lateral flow from these mountain front recharge areas into the Santa Cruz River valley axis.

Santa Cruz Graben

Drewes (1981) originally defined the Santa Cruz graben (fig. 7) and reported it to have formed during maximum episodes of extensional faulting (20 to 13 Ma) in the southern Arizona region. The southern part of the graben extends across our geologic map area (sheet 1, fig. 7), where it is bound on the west (from north to south) by the Tumacacori, Lowell, and Atascosa faults. Faults on the east side of the graben include (from north to south); the Santa Cruz fault and several north-striking segmented faults extending for about 10 km along the northwestern Santa Rita Mountains to the northern edge of sheet 1. Southward, faults forming the eastern graben margin include the Rio Rico and Grand Avenue faults (sheet 1; fig. 7). Description of fault offset relations along the graben margin are discussed below.

Western Graben Margin

The Tumacacori fault is mostly concealed, however, fault scarps are observed in latest Miocene to early? Pleistocene alluvial basin-fill deposits (map unit QTa on sheet 1) between Las Chivas Wash to the north and Aliso Canyon to the south (sheet 1). The Lowell fault is mostly concealed but is exposed in Peck Canyon at Atascosa Ranch (sheet 1) where it juxtaposes Oligocene volcanic rocks in the footwall against latest Miocene to early? Pleistocene alluvial basin-fill deposits in the hanging wall (sheet 1 map unit QTa). Alluvial basin-fill rocks (unit QTa) are also offset along the Lowell fault for about 1 km north of Peck Canyon.

Fault exposures along the down-to-the-east Atascosa fault extend southward from Wise Mesa to the Pena Banca Lake area (sheet 1) where Oligocene volcanic rocks in the hanging wall are offset against sedimentary and volcanic rocks of the Miocene Nogales Formation in the footwall. Southward of Peña Blanca Lake, the fault is mostly concealed, but faults offset the Jurassic Tuff of Pajarito against the sedimentary and volcanic rocks of the Miocene Nogales Formation from Walker Canyon southeastward to Calabasas Canyon (sheet 1). The fault is concealed southeast of Calabasas Canyon.

Eastern Graben Margin

Along the east side of the Santa Cruz graben (from north to south) fault scarps along the Santa Cruz fault are present from the Montosa Canyon Wash area southward to the Sheely Canyon (sheet 1). Faults in this area offset (1) latest Miocene to early? Pleistocene alluvial basin-fill (map unit QTa); (2) Old alluvial deposits (map unit Qo); and (3) late Pleistocene deposits (map unit Ql1). South of Sheely Canyon the Santa Cruz fault is concealed and we interpret it to merge with the Mount Benedict fault. East of the Santa Cruz fault, shorter segment, discontinuous faults bound the northwest Santa Rita Mountains and extend from the Montosa Canyon area southward to Mavis Wash (sheet 1). Faults along this segment offset deposits as young as middle Pleistocene and as old as latest Miocene (map units Qm, Qo, and QTa). South of Josephine Canyon the Rio Rico fault bounds the west flank of the San Cayetano Mountains and it extends southward to merge with the San Cayetano fault (sheet 1). The Rio Rico fault mainly offsets latest Miocene to early? Pleistocene basin-fill (map unit QTa) against the Cretaceous Salero Formation.

The southernmost fault defining the eastern margin of the Santa Cruz graben is the Grand Avenue fault which is interpreted to merge with the Mount Benedict fault at its northern end. Southward the fault is concealed to the Potrero Canyon area where it offsets rocks of the Miocene Nogales Formation in the footwall against latest Miocene to early? Pleistocene basin-fill (map unit QTa) in the hanging wall. South of Potrero Canyon and extending to the U.S.–Mexico border only short segments of the fault are exposed which primarily offset members of the Miocene Nogales Formation.

Mount Benedict Horst Block

The Mount Benedict horst block (fig. 7) is a triangular zone of uplifted Jurassic quartz monzonite of Mount Benedict and overlying members of the Miocene Nogales Formation. The horst block is important to the hydrogeologic framework because it forms an uplifted basement confining unit separating the southern upper Santa Cruz River basin into two groundwater basins, one to the east of the horst block and Santa Cruz River, and south of the Grosvenor Hills, and the other to the west of the horst block in the Nogales Wash drainage and east of the Tumacacori and Atascosa Mountains. These major basins are further subdivided into sub-basins originally defined by Bultman and Page (2016) and Page and others (2016b) and further discussed in the “Depth to Bedrock” section for the map area in this report. The Mount Benedict horst block is bound by major faults, including the Mount Benedict fault on the east side of the block and the Grand Avenue fault on the west side (fig. 7).

Hydrogeologic Investigations

Overview of Published Project Reports

Geologic Map of the Rio Rico and Nogales 7.5′ Quadrangles

Producing the geologic map of the Rio Rico and Nogales 7.5′ quadrangles (Page and others, 2016b) was the first objective of our project because existing geologic maps for these quadrangles lacked sufficiently detailed mapping and hydrogeologic data for the upper Santa Cruz River basin aquifer units, which include, from base to top, (1) the Miocene Nogales Formation; (2) late Miocene to early Pleistocene basin-fill; and (3) early Pleistocene to Holocene alluvium.

Our new mapping of the Nogales Formation resulted in significant stratigraphic revision including defining new members of the formation linked to member type areas. Mapping the formation in these quadrangles was significant because it is the thickest aquifer unit in the upper Santa Cruz River basin, reaching maximum thicknesses of 950 m (Page and others, 2016b), and the formation is well exposed due to dissection and faulting along the Santa Cruz River and Nogales Wash drainages. Furthermore, the base and top of the formation is well exposed providing clarification of important hydrostratigraphic relations with overlying and underlying units, more accurate estimates of unit thicknesses, and a better overall understanding of individual stratigraphic units within the formation.

New mapping of the Late Miocene to Holocene aquifer units in the Rio Rico and Nogales 7.5′ quadrangles (Page and others, 2016b) has also resulted in new detailed descriptions for those units that better define their hydrogeologic characteristics in the upper Santa Cruz River basin. We correlated our new mapping of the Rio Rico and Nogales quadrangles with surficial geologic mapping of Youberg and Helmick (2001) in the adjacent Tubac and Amado 7.5′ quadrangle, and Lindsey and Van Gosen (2005) in the Mount Hopkins and San Cayetano 7.5′ quadrangles. Most previous geologic maps within the Rio Rico and Nogales quadrangles did not define late Miocene to Holocene surficial units at sufficient levels of detail or spatial resolution to be useful in our compilation effort. Older regional maps (Drewes, 1980; Simons, 1974, and Graybeal and others, 2015) only described three or four generalized basin-fill and surficial units, whereas our new map in sheet 1 describes 18 total units. Interpretive mapping of basin-fill and alluvium was constrained by, and unit description and age estimates are based on data collected at GPS-located field stations along a series of traverses. Terrace heights were estimated from 1:24,000-scale topographic maps, digital elevation model (DEM) data, and for lower (younger) units, local field measurements. Surficial units are classified and mapped on the basis of both their genesis and relative age. These units are primarily alluvial in origin and were deposited either by axial streams and their major tributaries or by distributed, shallow, channel systems on piedmont alluvial fans, which also include sediment deposited by debris flows. Age estimates for the deposits are based primarily on age-related physical characteristics that change progressively with time. Chief among these are preservation of original depositional form or microtopography (for example, bar-and-swale morphology), development of desert pavement, degree of varnish development and amount of physical weathering of clasts (Bull, 1991), and the degree of soil development. The relative heights of stream-terrace and tributary-fan deposits provide an additional constraint on age estimates, because progressive and persistent dissection of major and tributary drainage systems, punctuated by periodic depositional events, produces a series of deposits where progressively younger deposits are inset within and topographically lower than older deposits. No radiometric ages have been obtained for Pliocene or Quaternary deposits in the map area. Thus, general age designations for these units are based on correlations with chronosequences developed in adjacent mapped areas (Helmick, 1986; Pearthree and Biggs, 1999; Pearthree and Youberg, 2000; Youberg and Helmick, 2001; Lindsey and Van Gosen, 2010). Map unit symbols for Quaternary deposits follow Youberg and Helmick (2001) to retain consistency with previous mapping in adjacent areas.

Hydrogeologic Investigations of the Nogales Formation

Part of our investigations included conducting hydrogeologic studies of the Miocene Nogales Formation (Page and others 2016a). These studies helped evaluate groundwater resource potential for the formation in the upper Santa Cruz River basin and results indicate that parts of the formation may provide additional sources of groundwater for the area. Samples of volcaniclastic sandstone were collected from outcrops of the formation and analyzed for porosity, bulk density, saturated hydraulic conductivity, and fabric. Results show that effective porosity ranged from 16 to 42 percent, bulk density from 1.6 to 2.47 grams per cubic centimeter, and saturated hydraulic conductivity (SHC) from 4 to 57 centimeters per day (4.9×10^{-5} to 6.7×10^{-4} centimeters per second). Thin sections examined for fabric characteristics exhibited framework grains consisting of quartz, feldspar, biotite, hornblende, pumice, volcanic glass, and opaque minerals, which primarily reflect erosion from Tertiary volcanic rocks in the region. Matrix in most samples consisted of pumice fragments, and predominantly silt and clay in others. Samples with a mostly silt and clay matrix have lower porosity and SHC compared to those with mostly pumice, which have higher and wider ranges of porosity and SHC. Pore space in the Nogales Formation sediments includes moldic, intercrystalline, and fracture porosity. Some intercrystalline pore space is partially filled with calcite cement. About one third of the samples contained fractures, consistent with fractures noted in outcrops in all members of the formation. Scanning electron microscope (SEM) and X-ray diffraction (XRD) analyses indicated that most of the samples

contained secondary zeolite and mixed-layer clay. X-ray diffraction analyses verified clinoptilolite as the main zeolite in Nogales Formation samples as well as smectite and illite clay with some kaolinite. Samples which contain greater amounts of clinoptilolite and lesser amounts of smectite had high porosity and SHC in narrow ranges. However, samples with abundant smectite and lesser amounts of clinoptilolite span the entire ranges of porosity and SHC for the formation.

All members of the Nogales Formation are fractured and faulted as a result of Tertiary Basin and Range extensional deformation, which was broadly contemporaneous with deposition of the formation. These structures may have significant influence on groundwater flow in the upper Santa Cruz River basin because although many of the sediments in the formation have characteristics indicating they may be productive aquifers based only on porous-media flow, faulting and fracturing of these sediments may further enhance permeability and groundwater flow in these basin-fill aquifers.

Three-Dimensional Hydrogeologic Framework Model of the Rio Rico and Nogales 7.5′ Quadrangles

Our project research included development of a three-dimensional (3-D) hydrogeologic model for the Nogales and Rio Rico 7.5′ quadrangles (Page and others, 2018). The 3-D model was constructed using EarthVision (Dynamic Graphics, Inc., https://www.dgi.com), a 3-D modeling software package used for analysis, synthesis, modeling, and visualization of geoscience data. A principal component of the model report is a 3-D Viewer, which consists of software enabling viewing data interactively in 3-D space, and the ability to sequentially slice through and rotate the modeled geology, to help examine and explain the internal complexities of the basin. Although the model was constructed using EarthVision software, the 3-D Viewer is a limited functionality version of the EarthVision main modeling program, that allows interactive visualization and manipulation of 3-D models using encrypted files. Once the encrypted file for the model is loaded on a computer, data and image registration files can be loaded and displayed for model visualization and other analyses. Datasets (EarthVision .dat file format) in the report include (1) files of all modeled fault sheet surfaces, (2) files defining the surfaces of the Late Cretaceous diorite stock at the southern edge of the model, and (3) groundwater elevation data points recorded from shallow water wells in the area. Image registration files include selected airborne electromagnetic data in the form of CDTs in the 3-D-model area.

Geologic units in the 3-D model area range in age from Jurassic through Holocene, and are defined and modified for the 3-D model, primarily from the geologic map of Page and others (2016a). Three major hydrogeologic units were defined in the model and these same unit subdivisions are presented in the cross sections in sheet 2 of this report and include (1) a bedrock confining unit, which consists of Jurassic monzonite, Cretaceous plutonic, volcanic, and sedimentary rocks, and Tertiary (Paleocene and Oligocene) volcanic and plutonic rocks; and the basin aquifer units including (2) the Miocene Nogales Formation and (3) latest Miocene to early? Pleistocene basin-fill deposits and early Pleistocene to Holocene alluvium.

One limitation of the 3-D model, and an important reason for its original construction, is the general lack of subsurface geologic data for the area, except for driller logs from shallow water wells, and a few deeper water wells. Location and depth data from 161 water wells were included in the model and helped define the water table elevation, but the wells generally are not deep enough to interpret subsurface geology and geometry, including defining faults and contacts between late Miocene to Holocene deposits, units of the Nogales Formation, and underlying Oligocene to Proterozoic bedrock units. Because subsurface data for the area are sparse, subsurface elevations of hydrogeologic units in the 3-D model were estimated based on a combination of surface geologic map data (Page and others, 2016a) projected into the subsurface, and geophysical data modeling from prior work (Bultman and Page, 2016). The configuration, geometry, and structure of the modeled geology currently represents the best interpretation of the subsurface geology, especially in areas with less data. Therefore, the 3-D model serves as an important starting point for further evaluation of groundwater resources in the basin. Because of the general lack of deeper wells in the upper Santa Cruz River basin, future investigations to test the accuracy of the 3-D model, including drilling deeper test wells to confirm our hydrostratigraphic and structural interpretations at depth, would improve characterization of subsurface geology and availability of water resources in this region.

New Hydrogeologic Investigations

Depth to Bedrock in the Geologic Map Area: Defining the Geometry, Thickness, and Structure of the Miocene to Holocene Upper Santa Cruz River Basin Aquifer Units

One of the major results of our geophysical investigations in the upper Santa Cruz River basin was development of a new depth to bedrock model to accompany the geologic map (sheet 1) and cross sections (sheet 2). The model is key to understanding and defining the geometry, thickness, and structure of the Miocene to Holocene basin aquifers which was one of our project's primary objectives. The new depth to bedrock model is based on two previously published depth to bedrock models in the upper Santa Cruz River basin. In this report bedrock refers to the Oligocene to Proterozoic igneous, sedimentary, and metamorphic rocks that underlie the basin aquifers. The basin aquifers consist of (1) the Miocene Nogales Formation; (2) latest Miocene to early? Pleistocene basin fill; and (3) early Pleistocene to Holocene alluvium. In

this report these Miocene to Holocene units are referred to collectively as "basin fill" or "sub-basins" (see figure 8 with named sub-basins).

The first and primary model used (Gettings and Houser, 1997; fig. 8) was based on an analysis of the complete Bouguer gravity anomaly and a depth-density function derived from estimates of porosity and saturated bulk density in the basin fill. Figure 8 displays the gravity stations used to build the model (other gravity stations that lie outside of the figure 8 boundaries are also used). Depth to bedrock was estimated using a procedure involving interpolation of (1) the depth-density functions derived in their report; (2) stratigraphic data from water wells; (3) a residual gravity anomaly grid obtained by subtracting the gravity effects of the bedrock ranges bordering the basin from the complete Bouguer gravity anomaly; and (4) depth to bedrock estimates from three Natural Uranium Resource Evaluation aeromagnetic profiles.

The Gettings and Houser (1997) model data were gridded at 1 km cell size to produce a map of depth to bedrock (fig. 9). This large cell size was required due to the scattered and dispersed nature of gravity data (gravity stations in fig. 9) in the upper Santa Cruz River basin. The map is known to have accurate depths in the northern part of the upper Santa Cruz River basin where the basin is dominated by large bowl-shaped sub-basins. In contrast, the southern portion of the basin is more complex with numerous sub-basins that are not well represented with a 1 km grid cell size. In addition, the southeastern portion of the basin has fewer gravity stations (fig. 9) and therefore the gravity-based depth estimates are less accurate.

The second depth to bedrock model used (from Bultman and Page, 2016) was created using the 1996 Patagonia aeromagnetic survey to estimate depths in the upper Santa Cruz River basin at a higher resolution than Gettings and Houser (1997). Bultman and Page (2016) estimated depths using three different methods: horizontal gradient analysis, analytic signal analysis, and Euler deconvolution, all based on data gridded with a 200 m cell size. In general, depth to bedrock estimates determined in that study are slightly shallower than the gravity-based depths in the deepest part of the basin; however, other geophysical evidence shows that they display more accurate depths at a higher resolution in other parts of the basin (Bultman and Page, 2016). In areas where the direction of natural remanent magnetization was known to be reversed with respect to the Earth's magnetic field and significantly modified the total measured magnetic field, the depth estimates of Gettings and Houser (1997) were used in the Bultman and Page (2016) model.

The depth to bedrock model from Bultman and Page (2016) covered only the Rio Rico and Nogales 7.5′ quadrangles (fig. 1). For this report, the model was enlarged, using the same methodology, to cover the entire portion of the upper Santa Cruz River basin south of Universal Transverse Mercator (UTM) northing 3489150. To the north of this point the deep sub-basins in the narrow part of the upper Santa Cruz River basin are best estimated using gravity. This model was gridded to produce a map with a 1 km cell size to match the resolution of the Gettings and Houser (1997) map.

The two depth to bedrock maps (Gettings and Houser, 1997, and the enlarged map based on the method of Bultman and Page, 2016) were combined to create a new depth to bedrock map (fig. 10) that extends over the entire portion of the upper Santa Cruz River basin represented by the geologic map (sheet 1) in this report. This was done by simply using the depth values from the map with the deepest depth at a given location. In this way, the more accurate values reported in the original Gettings and Houser (1997) map for the deepest portions of the basin are preserved. In addition, the 1 km gridded data of Gettings and Houser (1997) is more compatible with the 1:50,000 scale of the new geologic map presented in this report (sheet 1) compared with the finer 200 m grid size used by Bultman and Page (2016). Still, many individual sub-basins that were not identified in the gravity-based depth to bedrock map (fig. 9) can be seen in the aeromagnetic data portion of the new depth to bedrock map (see southern part of fig. 10). Two sub-basins labeled "A" and "B" are especially prominent. Sub-basin "A" is named here the Kino Springs sub-basin. Sub-basin "B" is named here the Highway 82 sub-basin and is discussed in Bultman and Page (2016).

Data from the 1998 transient electromagnetic survey over the upper Santa Cruz River basin (Bultman and Page, 2016) is in the form of CDTs, which are used here to test the existence of the Kino Springs sub-basin. Bultman and Page (2016) proposed the existence of the Highway 82 sub-basin just to the north based on interpretations using CDT and other data. In the location of the Kino Springs sub-basin, these CDTs are the only geophysical data available for interpretation.

The CDT is a one-dimensional transform developed by Wolfgram and Karlik (1995) to convert transient electromagnetic data to electrical conductivity in a cross-sectional format for each flight line in the survey. CDTs are based on a horizontal electrical conductor model and are generally effective for imaging horizontal conductors. While the depth and estimated conductivity may be approximate, the method is sensitive to the lateral extent of these conductors and therefore it can be effective for finding breaks and offsets (faults) in horizontal conductors. Vallée and Smith (2007) described the CDTs utility as a transform method by noting that it works as well as (but somewhat differently to) other layered earth inversions. The electrical conductivity values displayed in each CDT are generally given in Siemens per meter (S/m).

Some caveats should be considered when interpreting these data, including (1) under optimal conditions TEM interpretations including CDTs can locate the water table and distinguish saturated clays from saturated sands, and possibly unsaturated sediments from saturated sediments. When sediments, especially if saturated, lie on top of non-conductive bedrock, the method can work well for determining the apparent or relative depths to bedrock; and (2) acquiring TEM survey data over power lines or electrical noise of any kind greatly influences the data and the processing of the data. CDTs should be viewed with power line monitor information

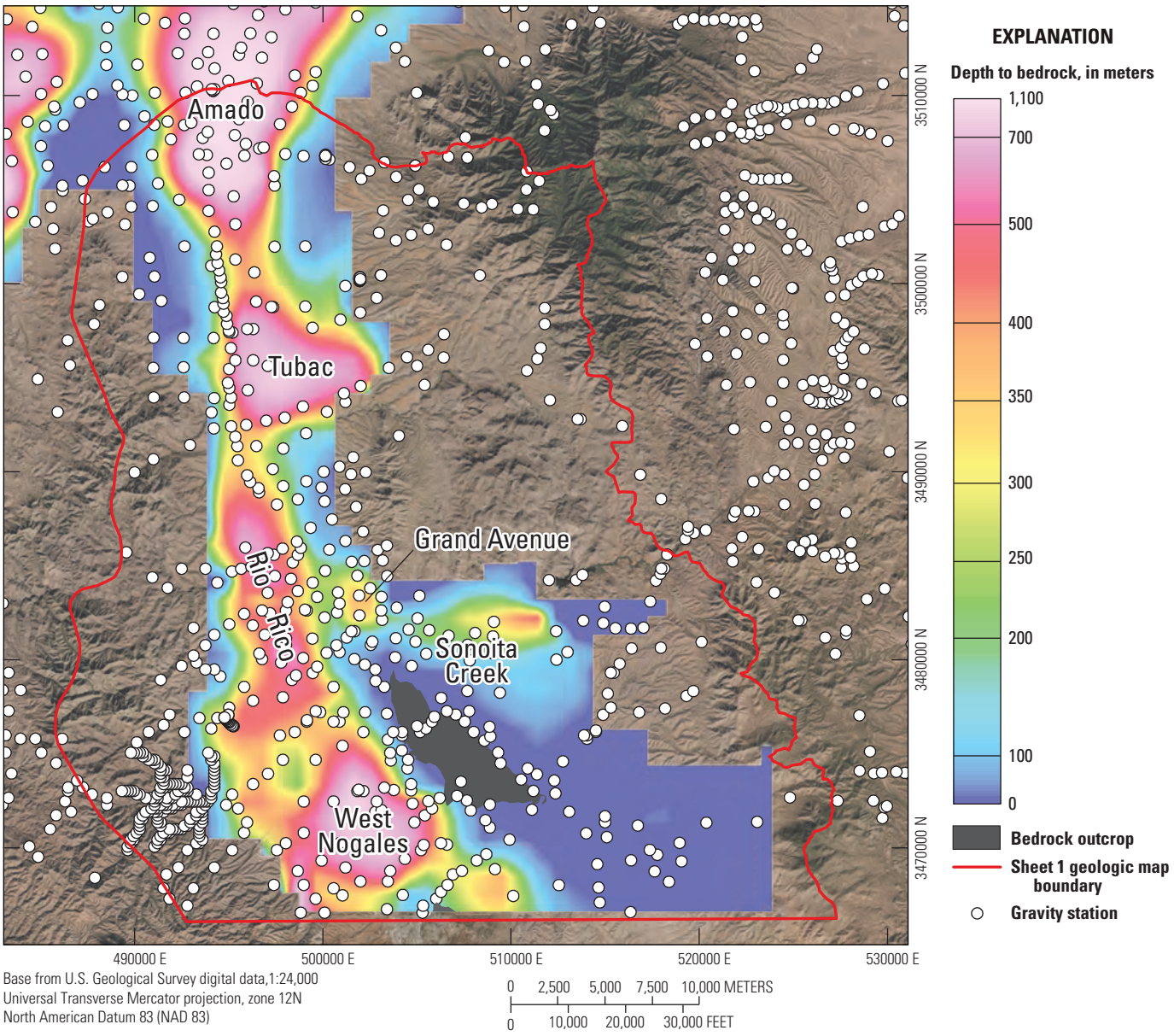

Figure 8. Depth to bedrock in the upper Santa Cruz River basin based on Gettings and Houser (1997). Red line indicates border of geologic map in sheet 1. Solid black areas are bedrock outcrop within the depth to bedrock map. Colored areas indicate the estimated thickness of basin-fill. Gravity stations used to build the model are displayed, and gravity stations that lie outside of the figure boundaries are also used. Sub-basins named in this report are labeled.

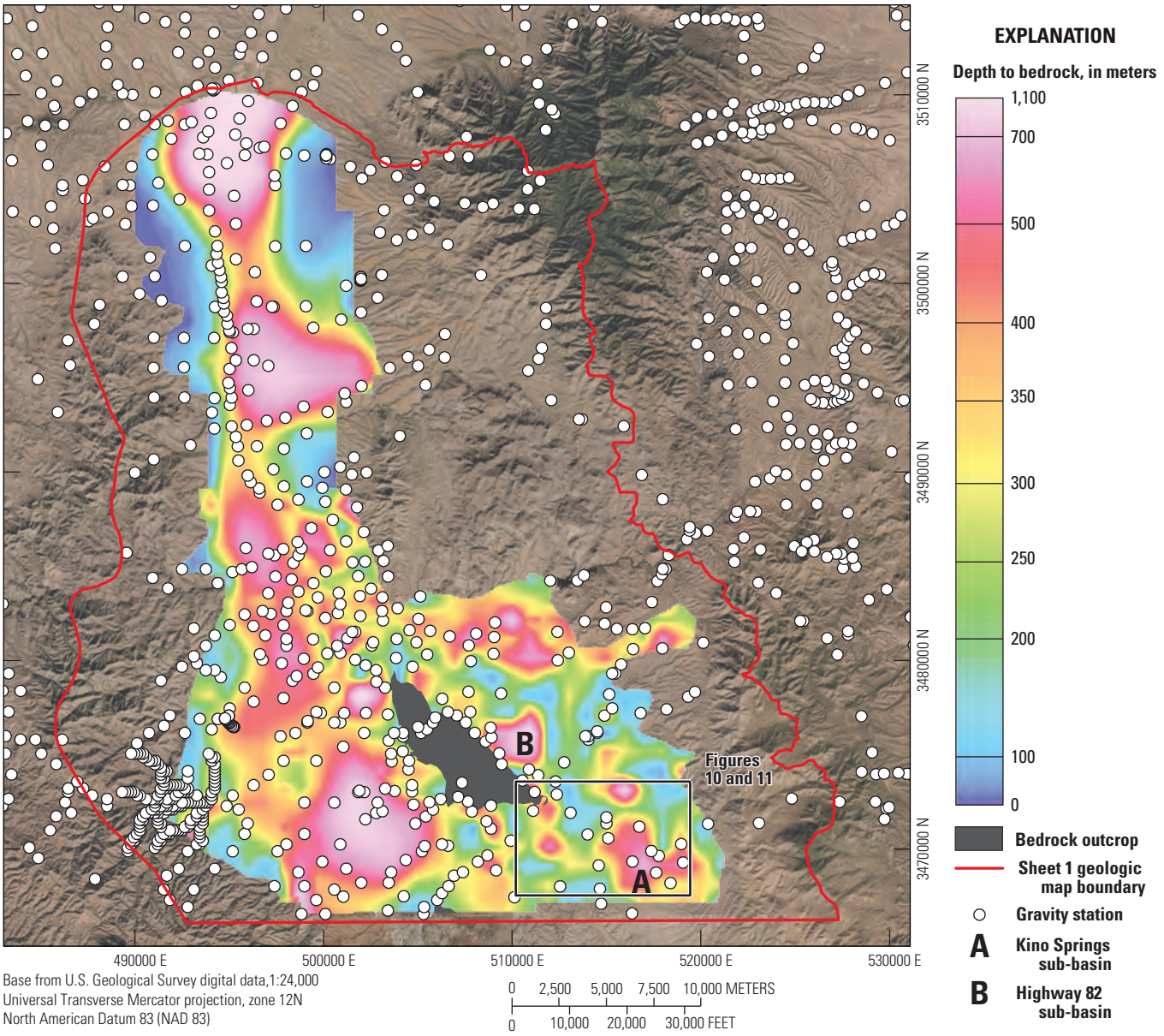

Figure 9. New depth to bedrock map in the upper Santa Cruz River basin based on the models of Gettings and Houser (1997), Bultman and Page (2016), and aeromagnetic data analyzed in this report. Red lines indicate border of geologic map in sheet 1. Solid black areas represent bedrock outcrop within the depth to bedrock map. Colored areas indicate the thickness of basin fill and alluvial units. Black outline in southeast part of map indicates area of figures 10 and 11. Gravity stations used to build the model are displayed (other gravity stations that lie outside of the figure boundaries are also used).

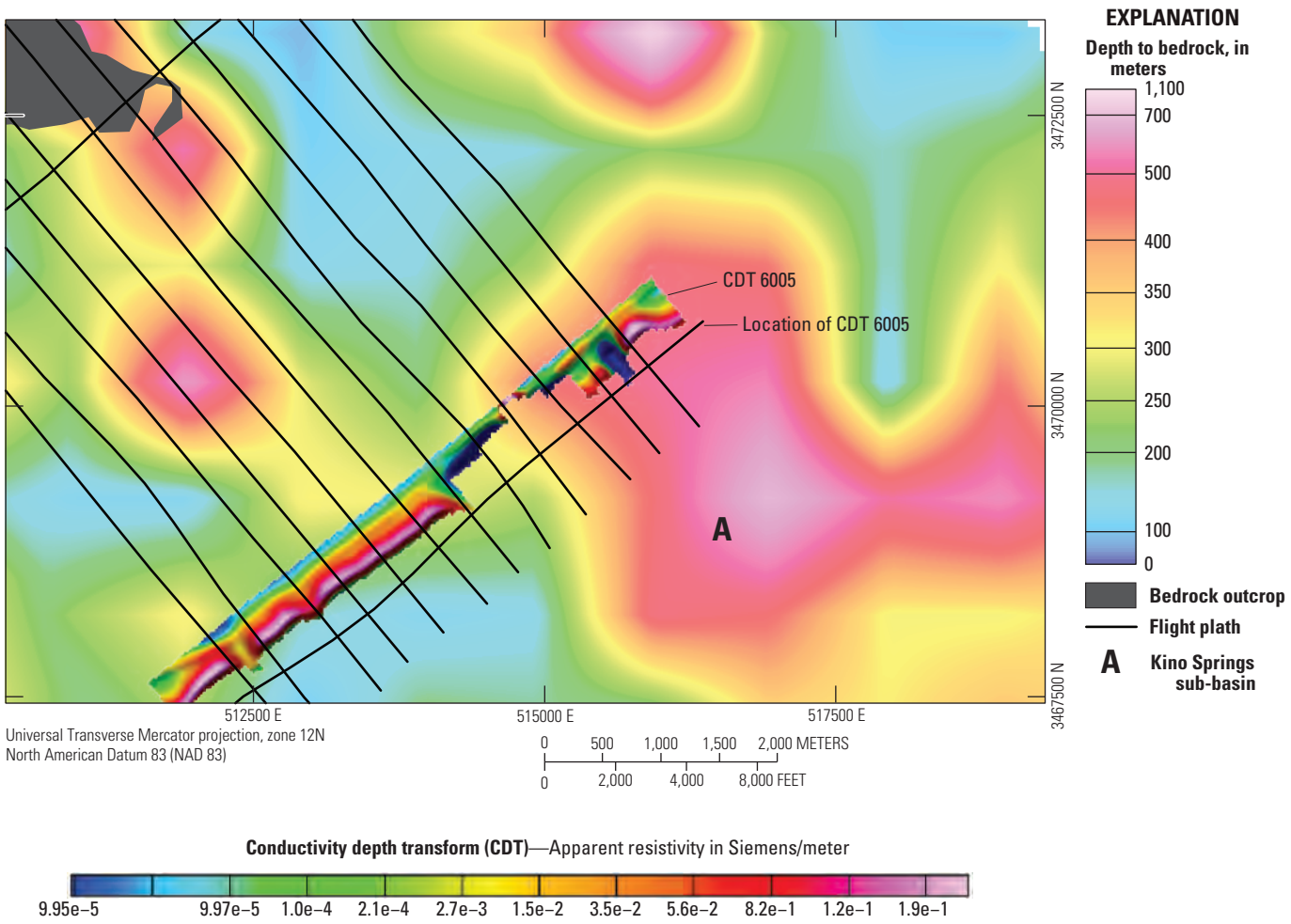

Figure 10. Transient electromagnetic conductivity depth transform (CDT) profile 6005 (Bultman and Page, 2016) plotted over depth to bedrock. Thin black lines indicate flight paths of aircraft that acquired TEM data. Location of flight path for CDT profile 6005 is indicated. The Kino Springs sub-basin is labeled "A." Map extent is indicated in figure 9.

(which is also acquired during the survey) and the results in areas of electrical noise should not be considered accurate; (3) the conductivity values are apparent conductivities and approximate; (4) these methods average conductivity over a large area; and (5) the CDT models are one dimensional.

Figure 10 shows CDT 6005 plotted on top of the depth to bedrock data in figure 9. The northeastern portion of this CDT enters the Kino Springs sub-basin labeled "A" and, as seen in the CDT, it appears that sediments thicken in the sub-basin as represented by thick medium (green) and high (red) conductivity regions in the CDT. While the CDTs show relative depths, the CDT in figure 11 indicates thickening of sediments over bedrock in the area of the Kino Springs sub-basin. Figure 11 shows CDTs 210 and 212 plotted on the depth to bedrock data of figure 9. The southeastern ends of these CDTs also enter the Kino Springs sub-basin labeled "A." As with CDT 6005, there is an indication that sediments thicken in the sub-basin as represented by thick medium (green) and high (red) conductivity regions in the CDT. All three CDTs support the thickening of sediments over intrusive bedrock and indicate the presence of the sub-basin.

The new depth to bedrock map (fig. 9) formed the foundation for construction of seven geologic cross sections (sheet 2) that illustrate the geometry, thickness, and structure of the Miocene to Holocene aquifer units in the upper Santa Cruz River basin. Two north-south cross sections follow the axes of the Santa Cruz River and the Nogales Wash Drainage basins and five east-west sections intersect the two north-south sections. The cross section locations were chosen to extend across the deepest parts of the sub-basins shown on the new depth to basement map (fig. 9). The surface profiles were constructed from 10-m DEMs and once the profile locations were chosen, contacts were drawn between the late Miocene to Holocene sediments, the Nogales Formation, and underlying bedrock units. The depths, geometry, and structure of the units were derived from combing the depth maps of Bultman and Page (2016) and Gettings and Houser (1997). East-west oriented sections were drawn perpendicular to the north-south sections

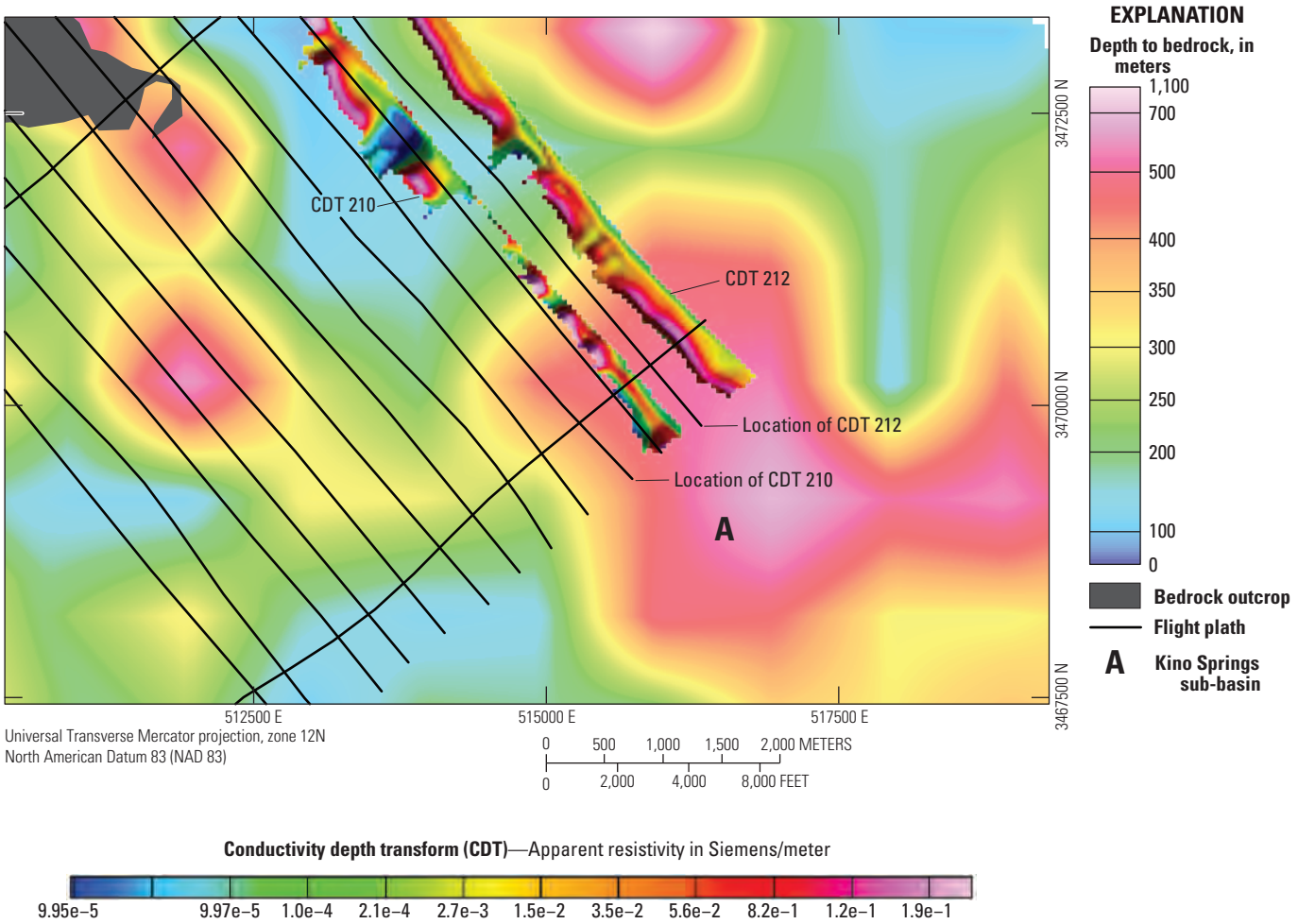

Figure 11. Transient electromagnetic conductivity depth (CDT) profiles 210 and 212 (Bultman and Page, 2016) plotted over depth to bedrock. Thin black lines indicate flight paths of aircraft that acquired TEM data. Location of flight paths for CDT profiles 210 and 212 are indicated. The Kino Springs sub-basin is labeled "A." Map extent indicated in figure 9.

and intersect at the deepest part of the sub-basins. Along each cross section profile the depth to bedrock (and base of the Nogales Formation) estimated depths using the three different methods described earlier and used to build the new depth to bedrock map shown in figure 9. In summary, the network of sections displayed in sheet 2 illustrates the depth, geometry and structure of the Miocene to Holocene groundwater sub-basins.

In addition, Page and others (2018) produced a 3-D model of the depth to bedrock data in the Rio Rico and Nogales 7.5′ quadrangles. An image of the bedrock surface for this model is shown with the depth to bedrock map in figure 12. Using software, both the Nogales Formation and late Miocene to Holocene surficial units can be added or removed from the 3-D model, and the model can be rotated and sliced to reveal a cross section of the basin units and underlying bedrock at any location or orientation.

Depth to Bedrock in the Sopori Wash Sub-Basin

Sopori Wash is a tributary to the Santa Cruz River and flowing northeast from near Arivaca, Arizona to join the Santa Cruz River near Amado, Arizona (fig. 13). Sopori Wash is part of the Arizona Department of Water Resources' Santa Cruz Active Management Area (https://new.azwater.gov/ama/santa-cruz) and merits special consideration in this report given that the Gettings and Houser (1997) depth to bedrock map (based on legacy gravity data) shows a 700+ meter deep sub-basin along the Sopori Wash (fig. 13). The sub-basin is referred to as the Sopori Wash sub-basin.

The Sopori Wash sub-basin, as depicted by Gettings and Houser (1997), is about 10 km in extent in the north-south direction and 5–7 km wide in the east-west direction (fig. 13). To the south of the deepest portion of the sub-basin, the depth to bedrock estimates decrease to less than 100 m depth before increasing again further south to form a second small

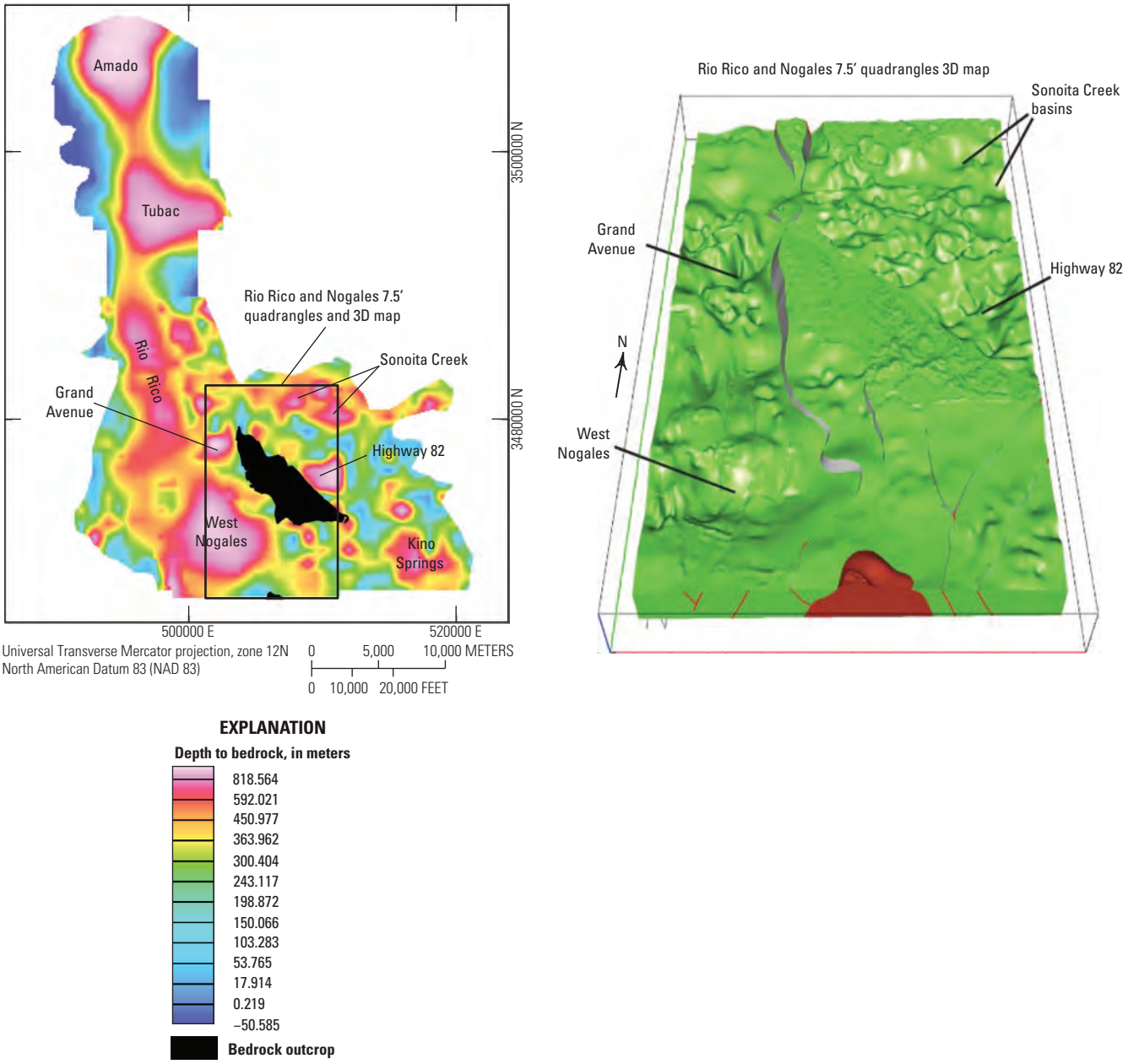

Figure 12. Map on left shows the named sub-basins defined in the depth to bedrock map in figure 9. The black rectangle shows the area of the Rio Rico and Nogales 7.5′ quadrangles (fig. 1 and Page and others, 2016b). The figure on the right shows the top of bedrock and corresponding sub-basins defined in the 3-D model of Page and others (2018).

depression with a depth of about 500 meters (fig. 14). The location and depth of that depression is primarily controlled by only one gravity station (as indicated by the southern-most white circle with a black border in the depression fig. 14).

Consistent with observations that the Nogales Formation crops out over a large area near Sopori Wash (sheet 1), gravity data of Gettings and Houser (1997) indicate only a thin veneer (less than 50 m) of latest Miocene to Holocene sediments in this area. Thus, the majority of sediments in the Sopori Wash sub-basin is likely dominated by Nogales Formation. It is possible, however, that the Sopori Wash sub-basin may have a small yet significant thick portion of Nogales Formation and late Miocene to Holocene sediments on its eastern side adjacent to the Tumacacori Mountains, based on geophysical modeling (Gettings and Houser, 1997).

To further define the size and shape of the Sopori Wash sub-basin and the small sub-basin to its south, data from 40 new gravity stations (table 2; Bultman, 2023) were acquired

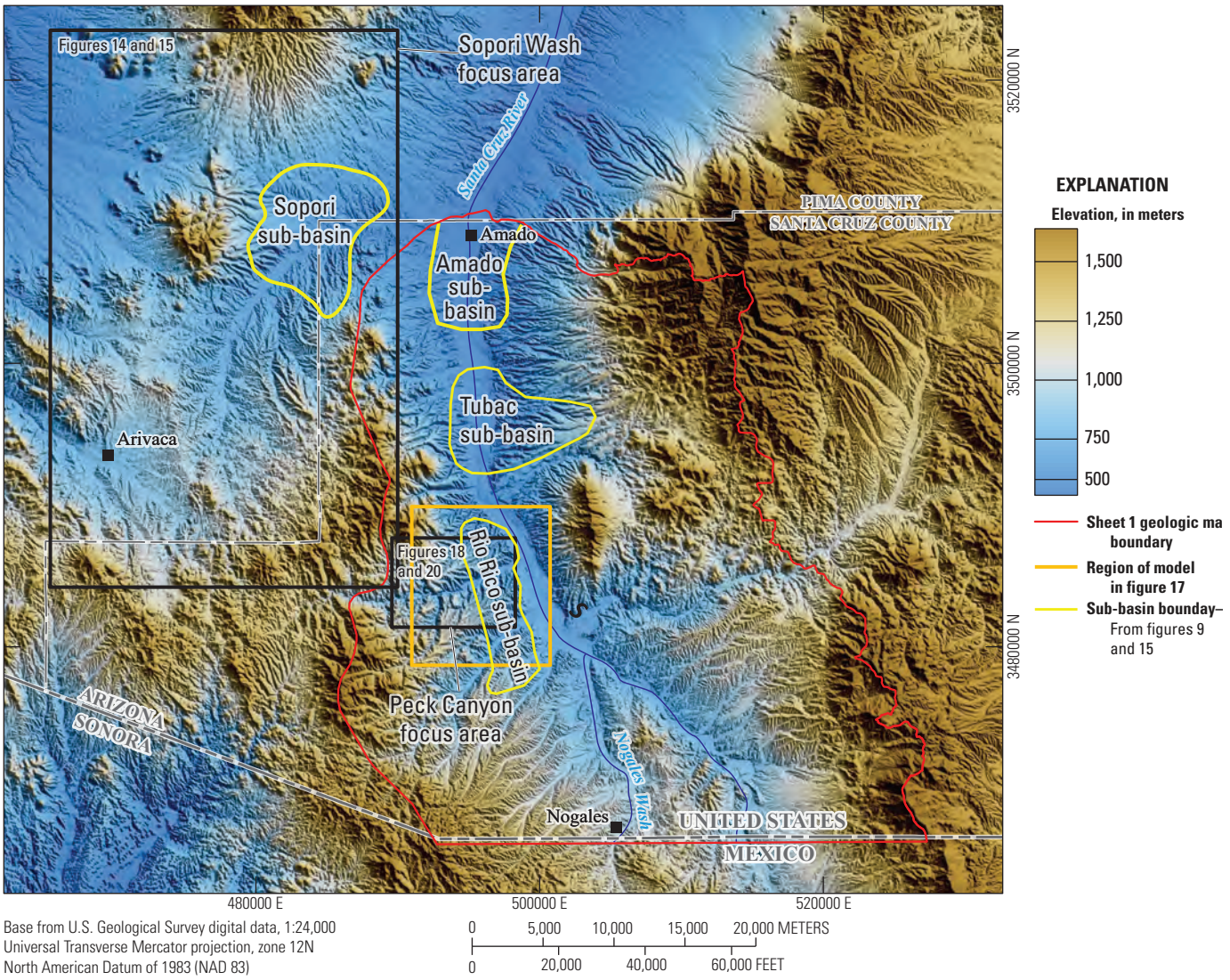

Figure 13. Location map for the Sopori Wash sub-basin plotted on digital elevation model showing features discussed in the text in the upper Santa Cruz River basin region.

over portions of the Sopori Wash sub-basin and in adjacent basin fill and bedrock that lacked gravity data (fig. 15). A new depth to bedrock map produced from both the new gravity data and existing legacy gravity data is shown in figure 15. The map was computed by subtracting a regional complete Bouguer anomaly grid based only on gravity stations located only on bedrock outcrop from the complete Bouguer anomaly grid based on all gravity data (Saltus and Jachens, 1995). The complete Bouguer anomaly grid based on all gravity data was gridded using the minimum curvature technique (Briggs, 1974; Swain, 1976) at a 250 m cell size while the complete Bouguer anomaly grid based only on gravity stations located only on bedrock outcrop was gridded at 1,000 m to facilitate interpolation across the basin. This method assumes that the density of bedrock under basin fill is similar to that found in the ranges adjacent to the basin.

The resultant residual gravity anomaly grid based on the basin fill sediments was then entered into a program to estimate depth to bedrock for a negative residual gravity anomaly using an input gravity anomaly versus depth function (Gettings and Houser, 1997). The gravity anomaly versus depth to bedrock function required by that program was obtained by fitting a least squares line (fig. 16) to data on depth to bedrock and residual gravity anomalies in the upper Santa Cruz River basin (table 5 in Gettings and Houser, 1997). The resultant residual gravity anomaly versus depth to bedrock relationship that was used is shown in table 3.

Based on the new Sopori Wash sub-basin depth to bedrock map (fig. 17), the north–south dimension of the basin is approximately the same, but the east–west dimension is considerably greater, especially in the northern and central parts of the basin. Access to the Cerro Colorado Mountains was not

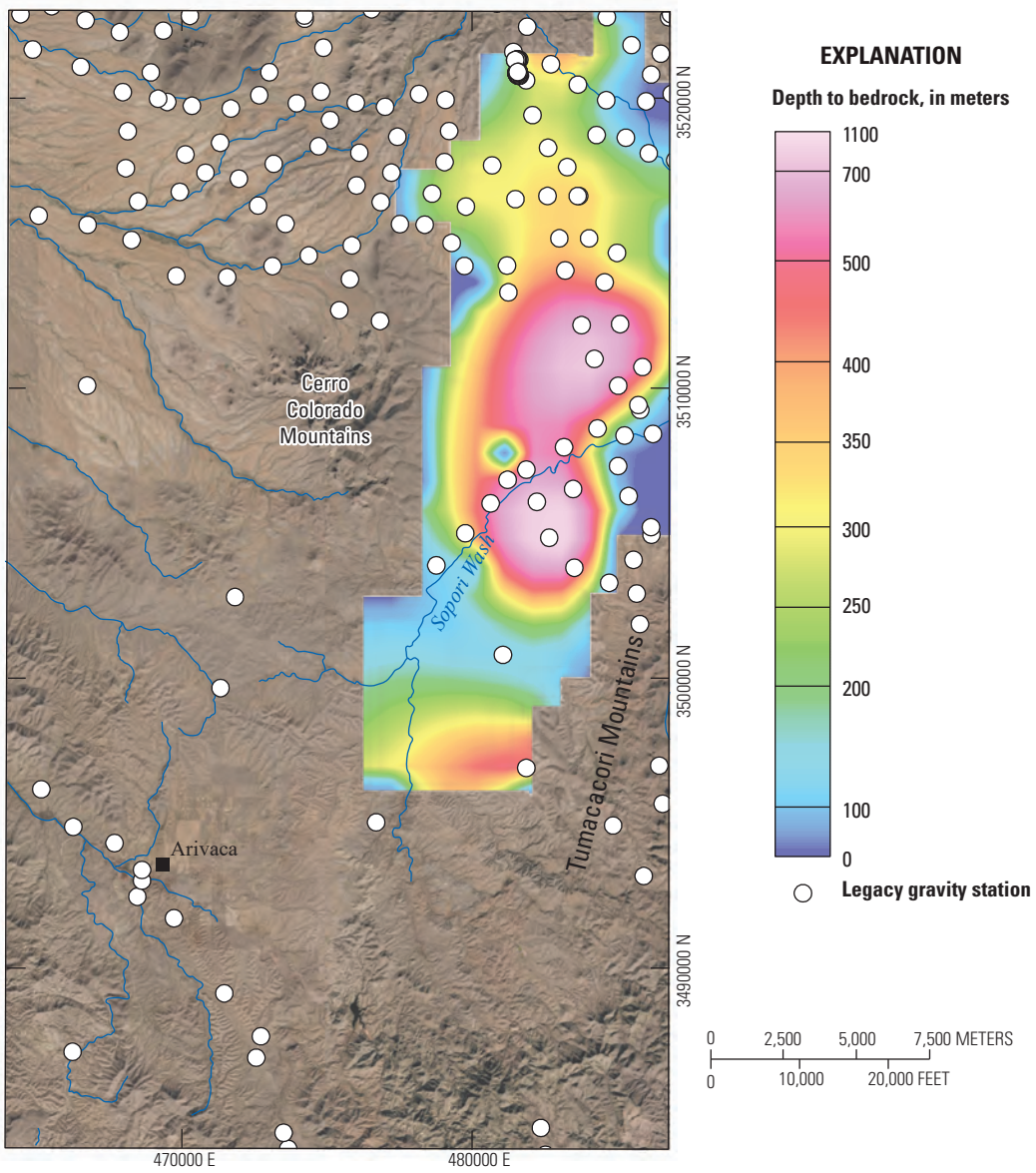

Base from U.S. Geological Survey digital data,1:24,000
Universal Transverse Mercator projection, zone 12N
North American Datum 83 (NAD 83)

Figure 14. Depth to bedrock map, Sopori Wash focus area after Gettings and Houser (1997). See figure 13 for regional location. The Sopori Wash sub-basin is depicted by areas of orange to pink colors indicating depths to bedrock of approximately 400 to 700 m. Only legacy gravity stations were used in the creation of this map.

Table 2. Principal facts for gravity stations acquired near Sopori Wash.

[Table modified from Bultman (2023), ID, identification; NAD 83, North American Datum of 1983; m, meters; NAVD88, North American Vertical Datum of 1988; mGal, milligals; TTC, total terrain correction; FAA, free air anomaly; SBA, simple Bouguer anomaly; CBA, complete Bouguer anomaly]

Station ID	Latitude NAD83	Longitude NAD83	Elevation (m) NAVD88	Observed gravity (mGal)	Theoretical gravity (mGal)	TTC (mGal)	FAA (mGal)	SBA (mGal)	CBA (mGal)
SOP1	31.6633918	–111.2803887	1127.338	979109.93	979109.10	0.24	1.59	–124.63	–124.39
SOP2	31.6426705	–111.2746907	1136.288	979103.66	979104.70	0.21	–0.25	–127.47	–127.25
SOP3	31.6467991	–111.2946385	1151.807	979101.54	979100.20	0.21	2.09	–126.87	–126.65
SOP4	31.6162543	–111.3023535	1176.652	979091.21	979090.10	0.22	1.89	–129.85	–129.63
SOP5	31.5864963	–111.2837735	1146.379	979091.06	979097.00	0.24	–5.20	–133.55	–133.31
SOP6	31.5960385	–111.2837906	1171.855	979088.20	979089.90	0.25	–0.97	–132.17	–131.92
SOP7	31.7109246	–111.1858639	1046.275	979117.50	979137.90	0.37	–19.69	–136.84	–136.46
SOP8	31.7021844	–111.2143255	1153.036	979096.03	979104.30	0.72	–7.51	–136.60	–135.89
SOP9	31.6975430	–111.2066058	1099.366	979107.05	979120.50	0.54	–12.68	–135.76	–135.22
SOP10	31.6459478	–111.2321347	1074.286	979110.72	979124.00	0.32	–12.58	–132.86	–132.55
SOP11	31.6597245	–111.2321273	1085.091	979110.92	979121.80	0.32	–10.16	–131.64	–131.33
SOP12	31.5896867	–111.1985859	1159.082	979084.93	979093.30	0.36	–7.66	–137.43	–137.08
SOP13	31.5962610	–111.1920279	1202.379	979074.85	979080.50	0.39	–4.91	–139.53	–139.14
SOP14	31.6198526	–111.1968722	1134.38	979089.55	979103.40	0.50	–13.10	–140.10	–139.60
SOP15	31.7163603	–111.1881247	1058.615	979115.33	979134.60	0.38	–18.50	–137.02	–136.64
SOP16	31.7177998	–111.1988714	1079.929	979111.50	979128.10	0.38	–15.86	–136.77	–136.39
SOP17	31.7172041	–111.2075698	1090.877	979110.12	979124.70	0.45	–13.81	–135.95	–135.49
SOP18	31.7156139	–111.2169476	1129.443	979103.05	979112.70	0.53	–8.85	–135.31	–134.78
SOP19	31.7161944	–111.2226575	1146.593	979100.72	979107.40	0.67	–5.94	–134.31	–133.64
SOP20	31.7107039	–111.2300653	1191.341	979091.11	979093.20	1.05	–1.30	–134.68	–133.63
SOP21	31.7036275	–111.2327622	1187.983	979091.21	979093.60	1.09	–1.66	–134.67	–133.58
SOP22	31.7043687	–111.2230928	1176.966	979092.34	979097.10	0.76	–3.99	–135.76	–135.00
SOP23	31.6210725	–111.2361129	1094.194	979102.52	979115.90	0.28	–12.63	–135.13	–134.85
SOP24	31.6300190	–111.2392189	1102.585	979102.37	979114.00	0.28	–10.92	–134.36	–134.08
SOP25	31.6354001	–111.2385520	1096.779	979104.45	979116.30	0.29	–11.06	–133.85	–133.57
SOP26	31.6360761	–111.2499602	1099.319	979105.56	979115.50	0.27	–9.22	–132.30	–132.03
SOP27	31.6426850	–111.2595629	1127.497	979103.70	979107.40	0.23	–2.92	–129.15	–128.93
SOP28	31.6442287	–111.2708931	1129.239	979105.29	979107.00	0.22	–0.91	–127.35	–127.13
SOP29	31.6623334	–111.2648084	1115.779	979110.79	979112.60	0.26	–1.03	–125.95	–125.69
SOP30	31.7340082	–111.1871721	1066.77	979115.62	979133.50	0.34	–17.11	–136.54	–136.21
SOP31	31.8999893	–111.2008081	1096.295	979109.48	979137.80	0.36	–27.57	–150.32	–149.96
SOP32	31.7323018	–111.2170304	1151.116	979100.27	979107.30	0.48	–6.29	–135.17	–134.69
SOP33	31.6798000	–111.2001486	1058.264	979110.47	979131.70	0.36	–20.51	–138.99	–138.63
SOP34	31.6704505	–111.1993489	1058.854	979109.03	979130.80	0.36	–21.01	–139.56	–139.20

Table 2. Principal facts for gravity stations acquired near Sopori Wash.—Continued

[ID, identification; NAD 83, North American Datum of 1983; m, meters; NAVD88, North American Vertical Datum of 1988; mGal, milligals; TTC, total terrain correction; FAA, free air anomaly; SBA, simple Bouguer anomaly; CBA, complete Bouguer anomaly]

Station ID	Latitude NAD83	Longitude NAD83	Elevation (m) NAVD88	Observed gravity (mGal)	Theoretical gravity (mGal)	TTC (mGal)	FAA (mGal)	SBA (mGal)	CBA (mGal)
SOP35	31.6614070	–111.1961497	1069.515	979105.17	979126.80	0.38	–20.85	–140.60	–140.22
SOP36	31.6518263	–111.1939539	1080.954	979101.48	979122.50	0.46	–20.24	–141.26	–140.80
SOP37	31.5832898	–111.2717544	1179.505	979082.61	979086.50	0.25	–3.16	–135.22	–134.97
SOP38	31.5945053	–111.2498129	1150.013	979090.82	979096.50	0.24	–4.96	–133.72	–133.48
SOP39	31.6024493	–111.2370979	1122.22	979097.13	979105.70	0.30	–7.87	–133.52	–133.22
SOP40	31.6128893	–111.2371523	1113.606	979098.29	979109.20	0.27	–10.21	–134.89	–134.62

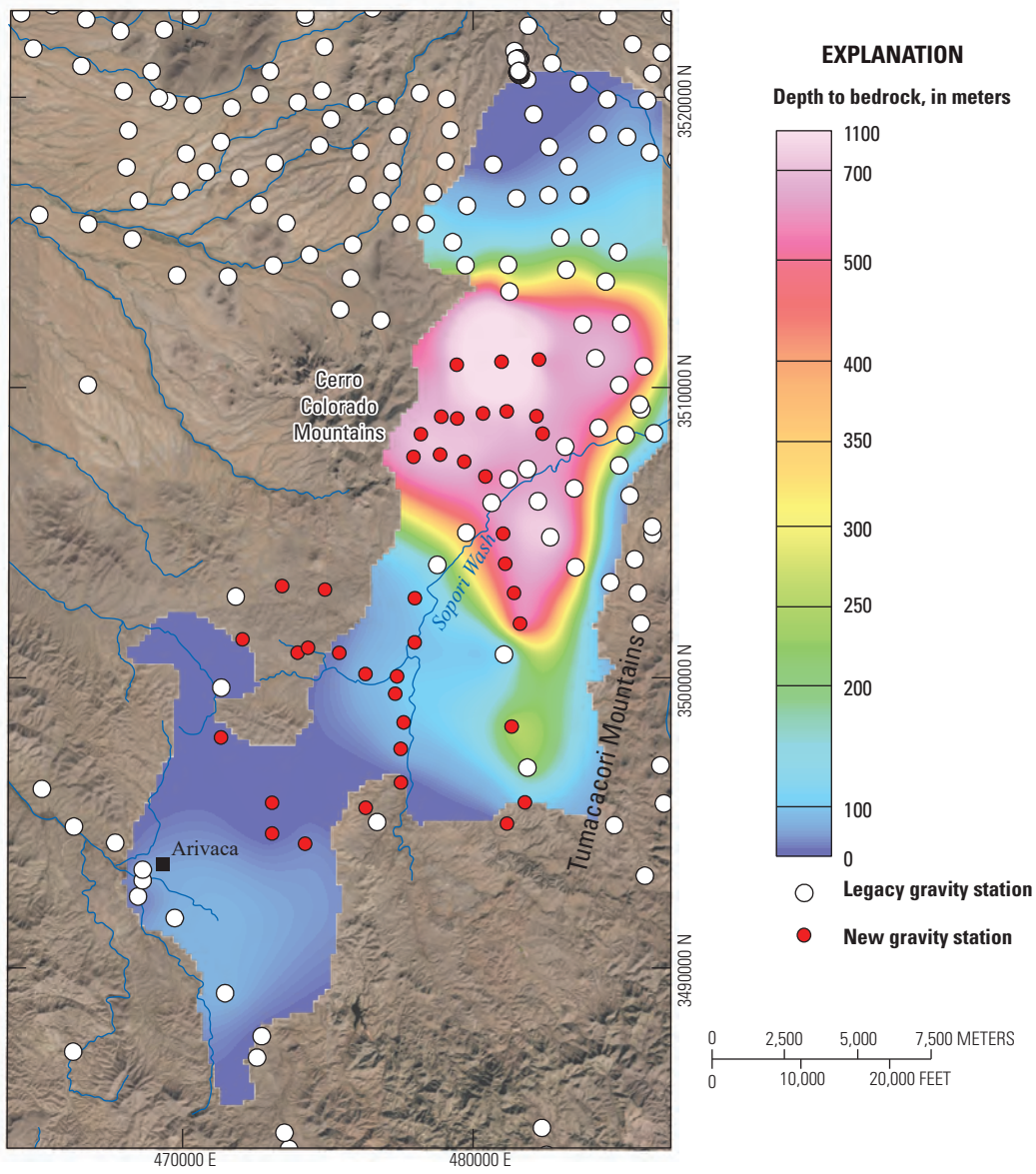

Base from U.S. Geological Survey digital data,1:24,000
Universal Transverse Mercator projection, zone 12N
North American Datum 83 (NAD 83)

Figure 15. Depth to bedrock map of the Sopori Wash focus area based on both legacy gravity data and the new gravity data presented in this report. The Sopori Wash sub-basin is depicted in areas of orange to pink colors indicating depths of approximately 400 to over 700 meters. Map extent shown in figure 13.

possible and no new gravity stations could be acquired there. Therefore, the western boundary of the basin can only be defined by the presence of mapped bedrock. Without nearby subsurface bedrock depth control, interpretation in the extreme western portion of the basin may overestimate depths of basin fill. Depths estimated in the vicinity of the gravity stations are thought to be generally reliable but can still be affected by sources of bias, especially if the Cerro Colorado range has a large negative gravity anomaly. Existing gravity stations to the north and west of the range are available, and it is unlikely that estimated depths in the basin are inaccurate given that the same methods are used as Gettings and Houser (1997), whose estimates have been proven accurate in adjacent basins (Bultman and Page, 2016). In addition, the new gravity stations indicate that the southern depression in the Sopori Wash sub-basin is less extensive and shallower than interpretations based on legacy data (Gettings and Houser, 1997). However, the large extent of deep sediment-filled depressions found in the main part of the Sopori Wash sub-basin indicates that it may be a potential source of groundwater resources. Figure 17

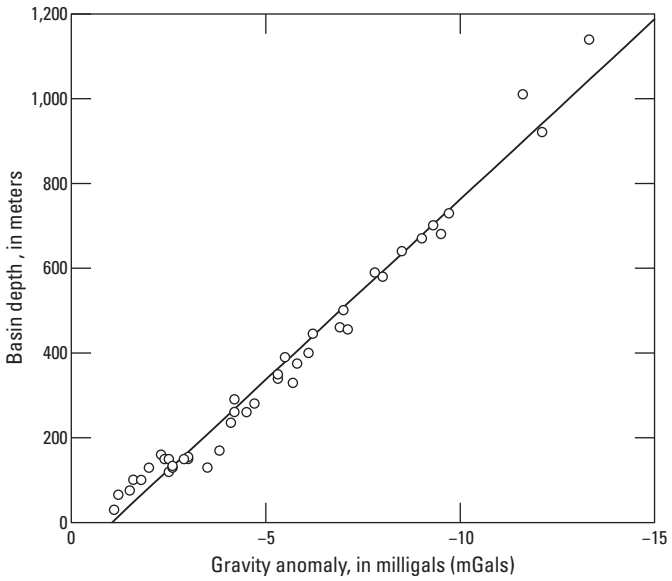

Figure 16. Least squares fit (line) to residual gravity anomaly versus calculated basin depth to bedrock for individual water wells (circles). Data from Gettings and Houser (1997; their table 5).

Table 3. Residual gravity anomaly versus depth to bedrock data used in the Sopori Wash sub-basin.

[Data derived from table 5 in Gettings and Houser (1997). mGal, milligals; m, meters]

Residual gravity anomaly (mGal)	Depth to bedrock (m)
–1	39
–2	82
–3	167
–4	252
–5	337
–6	422
–7	507
–8	592
–9	677
–10	762
11	847
–12	932
–13	1,017
–14	1,102
–15	1,187

displays the depth to bedrock map of the entire upper Santa Cruz River basin created by combining the depth to bedrock maps of Sopori Wash (fig. 15) and the upper Santa Cruz River basin (fig. 9).

Delineation of Hydrologically Significant Faults Near Peck Canyon

The Rio Rico, Tubac, and Amado sub-basins are located in the upper Santa Cruz River basin north of the confluence of the Santa Cruz River and Nogales Wash (fig. 13). The sub-basins become increasingly deeper northward along the river (fig. 8). In addition, groundwater levels become progressively deeper to the north (Nelson, 2007) and the general flow of groundwater is from south to north (Nelson, 2007)

In 2007, the Arizona Department of Water Resources published a modeling report for the Santa Cruz Active Management area (Nelson, 2007) that indicated that the northern portion of the Rio Rico and Tubac sub-basins (figs. 8 and 13) had unusually stable groundwater levels. That report indicated that "faults might be, at least partially, responsible for the stable groundwater levels observed in the northern portion of the Rio Rico Sub-area and the Tubac Sub-area …" (Nelson, 2007, p. 17). Based on an alternative conceptual model that included the possibility of faulting along the western upper Santa Cruz River basin, Nelson (2007) conducted an aquifer test at the Atascosa Ranch on February 17, 2006.

Figure 18 is an aerial photo that encompasses what we refer to as the Peck Canyon focus area. The Atascosa Ranch is located on the western side of this area (fig. 1) in Peck Canyon and overlies the generally north-striking range-front fault named here as the Lowell fault, which juxtaposes Oligocene volcanic rocks of the Atascosa and Montana Peak Formations on the west against latest Miocene to early? Pleistocene sediments (map unit QTa) to the east. The Lowell fault may be responsible for the high hydraulic conductivity measurements observed in the area and is discussed below. Also, the major range-front-fault named the Tumacacori fault (fig. 7) and a northwest-striking fault that merges with the Tumacacori fault named the Agua Fria Canyon fault are shown in figures 7 and 18.

Drewes (1980) inferred the location of Tumacacori fault in the Peck Canyon focus area to be just to the east of exposed Oligocene volcanic rocks of the Atascosa and Tumacacori Mountains and completely concealed by latest Miocene to early? Pleistocene basin-fill and younger alluvium. New mapping for this report (sheet 1) locates the Lowell fault just west of the Tumacacori fault. The Lowell fault is exposed in bedrock in Peck Canyon at the Atascosa Ranch headquarters (fig. 18), and it merges with the Tumacacori fault at its northern and southern ends (sheet 1).

There is geophysical evidence for the location of the concealed Tumacacori fault including curvilinear maxima in the gravity gradient data that indicate boundaries between rocks of different densities (Bultman and Page, 2016). Such a feature is visible paralleling the Tumacacori fault south of Peck Canyon (fig. 18). To the north of Peck Canyon, there are not enough gravity station data to generate gravity gradient information (fig. 18). The data show no curvilinear gravity gradient maxima associated with the Lowell or Agua Fria Canyon faults, but this does not disprove their existence.

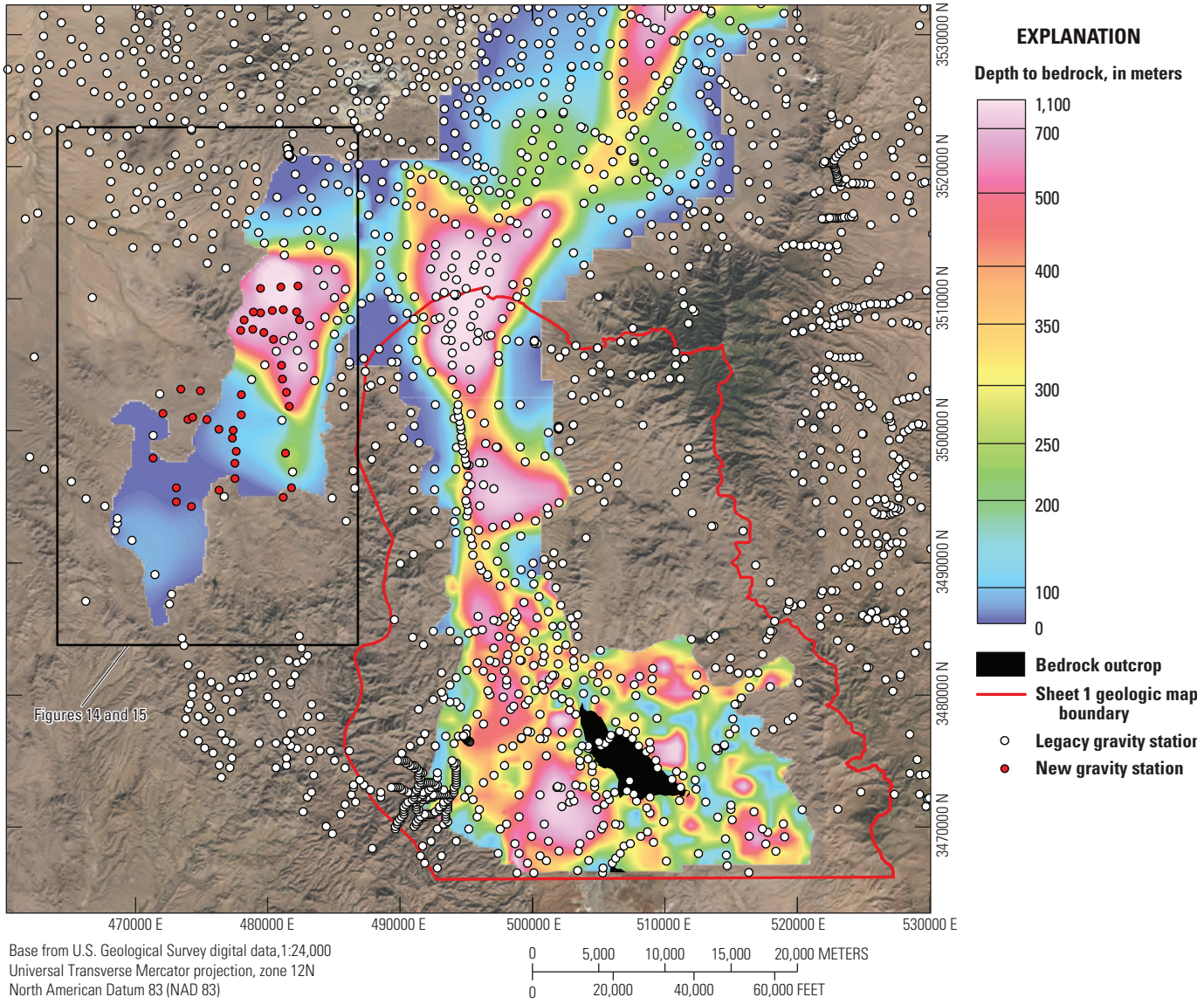

Figure 17. New depth to bedrock map of the entire upper Santa Cruz River basin region created by combining depth to bedrock maps for the Sopori sub-basin and the upper Santa Cruz River basin (figs. 15 and 9 respectively). Black rectangle indicates regions displayed in figures 14 and 15 (Sopori Wash focus area).

An indication of high hydraulic conductivity in this area can be seen at times of moderate streamflow in Peck Canyon Creek, which flows west to east through the Peck Canyon focus area (fig. 18). Water in the stream simply disappears into the ground on the Atascosa Ranch property (figs. 18 and 19). The aquifer test conducted by Nelson (2007) used a test well (fig. 18) located very close to the location where surface water disappears into the ground in Peck Canyon Creek (fig. 19). This well showed a static depth to water level of 199.5 feet at the time of the aquifer test. A constant pumping rate of 75 gallons per minute was applied to the well and the depth to water dropped 200.5 feet after 30 seconds of pumping. The dynamic depth to water remained stable at 200.5 feet after 30 minutes of continuous pumping, after which the test was terminated (Nelson, 2007). Interpretation of these results gave a Theis and Cooper-Jacob drawdown solution of transmissivity equal to 260,000 feet^2/day, and a hydraulic conductivity equal to 2,890 feet/day (Nelson, 2007). The specific capacity solutions were 20,000 feet^2/day for transmissivity and 230 feet per day for hydraulic conductivity (Nelson, 2007). Nelson (2007, p. 106) concluded that the high hydraulic conductivity and transmissivity found at this well indicates “there is very little resistance to groundwater flow in the vicinity of this well site.”

Conductivity depth transforms (CDTs) from the 1998 Santa Cruz transient electromagnetic survey (Bultman and Page, 2016) were used to investigate the relationship between range-front faults and high hydraulic conductivity observed in the Peck Canyon focus area. Figure 20 displays 11 CDTs

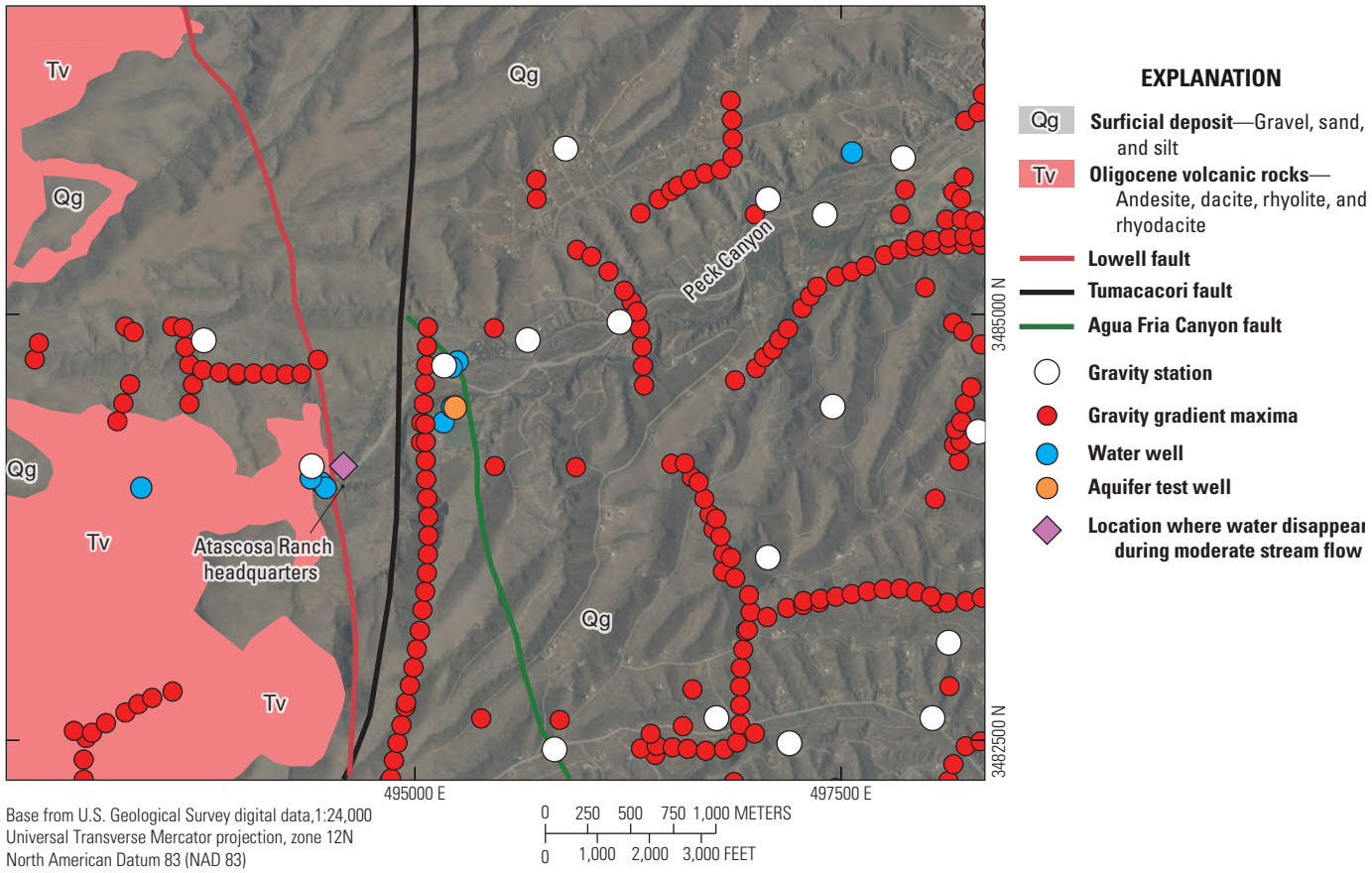

Figure 18. Aerial photo of Peck Canyon focus area (see fig. 13 and map sheet for location of this area within the region). Outcrop of Oligocene volcanic rocks are indicated by red polygons (unit Tv) after Drewes (1980). During periods of moderate flow, water simply disappears into the ground near the shown well (star symbol) and inferred fault on the Atascosa Ranch. Gravity gradient data maxima are derived from the map of complete Bouguer anomaly data (Bultman and Page, 2016).

directly above the flight lines over which they were acquired in the Peck Canyon focus area. The terrain surface of the CDT grids has been projected to approximate the true terrain surface but is not highly accurate. In addition, the Lowell, Tumacacori, and Agua Fria Canyon faults are shown. As noted above, the location of the Tumacacori fault is supported by geophysical evidence, namely a curvilinear gravity gradient maxima that trends along it south of Peck Canyon (fig. 18). In addition, figure 20 indicates that just north of Peck Canyon there is a distinct resistivity low at depth that follows the inferred location of the Tumacacori fault. While not as obvious in the CDT data, a zone of low resistivity at depth coincides with the trace of the Lowell fault, although resistivity values there are not as low as those along the Tumacacori fault.

Low electrical conductivity values in CDTs in basin fill sediments can indicate the absence of clay minerals, especially in saturated sediments. Telford and others (1990) reported that the resistivity of clay-rich sediments can range from 1 to 100 ohm-m (conductivity of 1 to 0.01 S/m). Jia and others (2014) indicated that the electrical conductivity of saturated clay-rich soil is approximately 0.04 S/m or higher with electrical conductivity decreasing both as saturation decreases or as sand content of the sediments increases. In general, electrical conductivities measured in saturated sediments less than 0.04 S/m indicate low clay contents, and clay content decreases as conductivity decreases for a constant salinity. It is hypothesized that at depths greater than 100 m along the Tumacacori fault north of Peck Canyon there is a fracture zone in saturated sediments with an extremely low electrical conductivity (less than 0.005 S/m), likely indicating sediment with an extremely low clay content. We interpret this zone as a high hydraulic conductivity conduit for groundwater to move to the north. This apparent low-clay fracture zone begins near Peck Canyon where it is present near the surface based on CDT profile 411 (fig. 20). This location is nearly coincident with the location of disappearing streamflow in Peck Canyon Creek. The high-hydraulic-conductivity fracture zone allows mountain front recharge into the basin aquifer and likely funnels most of that recharge down-gradient to the north. The trace of the Agua Fria Canyon fault also follows both deep breaks in electrical conductors (fig. 20, CDT profiles 415, 414, 413, and 411) as well as deep areas of low resistivity in the CDTs. The Lowell fault is not well expressed in the CDTs south of Peck Canyon (413–416). It is possible that the fault is very shallow

Figure 19. Photograph of Peck Canyon Creek looking east of Atascosa Ranch. During periods of moderate streamflow, water simply disappears into the ground near the test well and the Lowell and Tumacacori faults (fig. 18). Photograph by William R. Page, U.S. Geological Survey.

here or does not offset rocks of differing conductivity. At Peck Canyon the fault correlates well with a deep zone of low electrical conductivity that continues to the north except for CDT 411. The Lowell fault is exposed at the surface where it crosses Peck Canyon and at locations north of Peck Canyon.

Figure 21 shows the information from the CDTs of figure 20 converted into a 3-D volume by interpolating between the east–west CDTs profiles projected in the north–south direction. The 3-D volume is displayed on top of the geologic map of Drewes (1980) which was published at 1:125,000-scale and is used in figure 21 to provide general location and geologic information. The Drewes range-front-fault shown in figure 21 is the same as the Tumacacori fault in this report. The Lowell and Agua Fria Canyon faults have been added to the geologic map in figure 21 as dashed red lines.

The 3-D volume is cut along an east–west line that moves progressively northward in figure 21*A–E*. This view shows that both the Lowell and Tumacacori faults can be spatially correlated to deep areas of low electrical conductivity, albeit with one exception, seen in figure 21*B*. There, both faults intersect a conductor that appears to be deformed at depth. The Tumacacori and the Lowell faults begin to diverge in figure 21*F*. Here again, they intersect a conductor at depth but it appears to be structurally deformed. The northwest-striking Agua Fria Canyon fault lines up with low electrical conductivity zone at depth that also strikes northwest in figures 21*B–F* and 21*F*, and it intersects a region of low electrical conductivity extending to the surface just south of Peck Canyon. Based on those geophysical features, we interpret that this area may be important for range-front recharge in this part of the upper Santa Cruz River basin.

As the 3-D volume is cut farther to the north in figure 21*G*, the Lowell and Agua Fria Canyon faults represent the western and eastern edge, respectively, of a zone of very low conductivity that reaches the surface in Peck Canyon. The Tumacacori fault continues to follow the narrow zone of low electrical conductivity to the north.

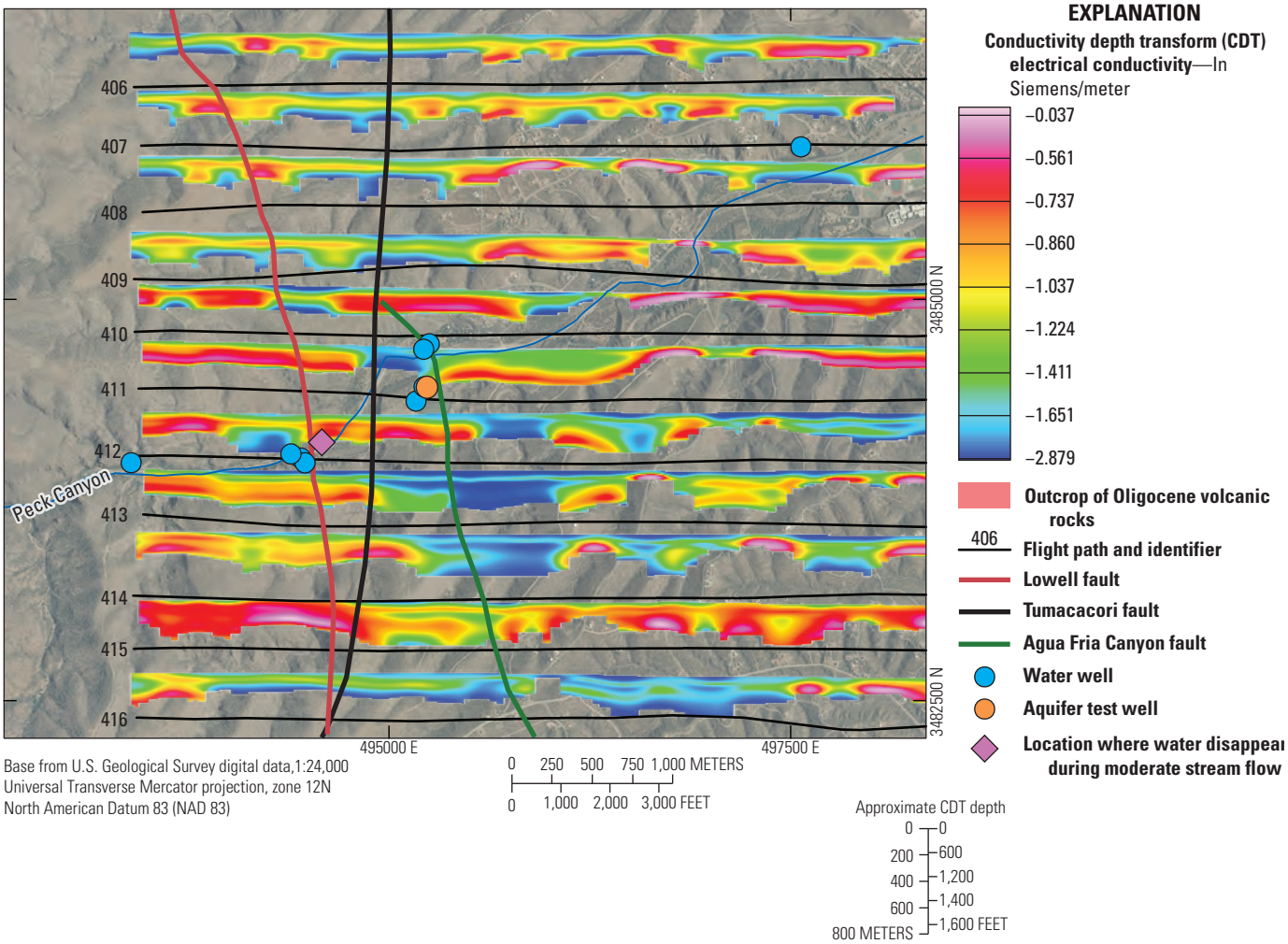

Figure 20. Conductivity depth transforms (CDTs) in the Peck Canyon focus area plotted over aerial photography. CDTs are labeled on the left side and displayed above their acquisition flight paths (black west-east lines).

The Lowell fault strikes slightly to the northwest as it enters Peck Canyon (fig. 21*G*) where it outcrops at the Atascosa Ranch headquarters. The zone of low electrical conductivity at depth continues to trend northward following the Tumacacori fault. In addition, the Agua Fria Canyon fault merges into the Tumacacori fault in this area. A distinct and narrow zone of low electrical conductivity is observed at depth here, and it continues upward to the surface in the same area where water flowing down Peck Canyon creek disappears at times of moderate streamflow.

In figure 21*B*, the Lowell and Agua Fria Canyon faults join at a region of low to moderate resistivity at depth. The Tumacacori fault continues to the north in a distinctive region of low electrical conductivity at depth. The regions of low conductivity at depth continue in figures 21*I* and 21*J*, where they merge between the two faults and extend upwards to near the surface.

Figure 22 illustrates a closer view of the 3-D volume representation of the CDT profiles looking to the northeast. The CDT volume is cut on a north–south line at an easting value of 495000 m to show the low electrical conductivity at depth along the Tumacacori fault north of Peck Canyon. Figure 23 illustrates the 3-D volume representation of the CDT profiles viewed looking to the north. In this view, the entire volume is shown, but all portions of the 3-D volume with conductivity higher than 0.03 S/m have been removed, leaving only regions with low electrical conductivity. These regions are shown to spatially correlate to the Lowell and Tumacacori faults.

The Lowell and Tumacacori faults merge south of Peck Canyon in the Peck Canyon focus area and are the main range-front faults separating the Tumacacori Mountains to the west and the upper Santa Cruz River basin to the east. The faults coincide with a low electrical conductivity zone in this region (fig. 23). At a northing of approximately 3484000, the two concealed faults diverge. The Tumacacori fault strikes north,

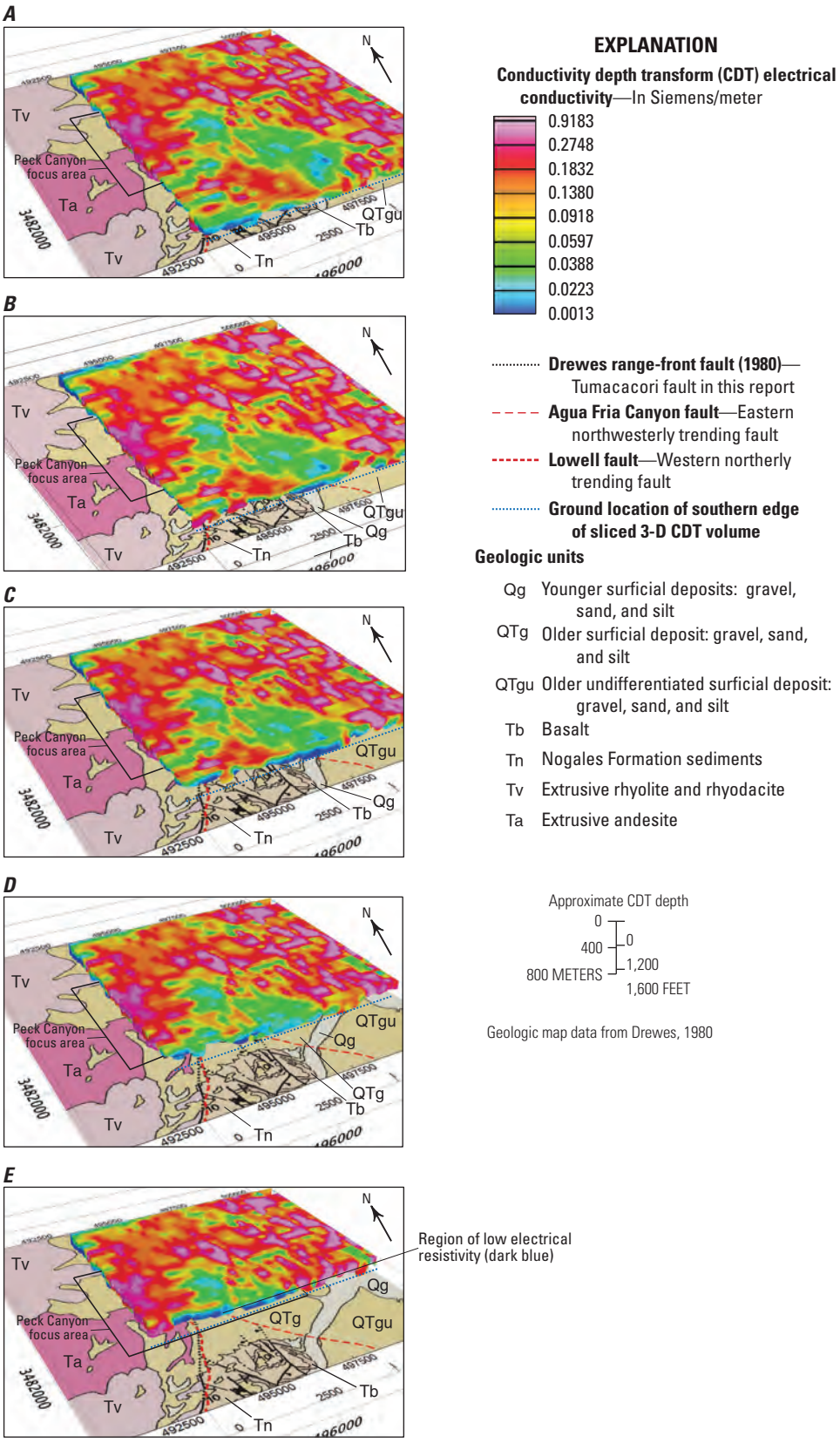

Figure 21. Conductivity depth transforms transformed to a voxel volume representation in the Peck Canyon focus area displayed over the geologic map of Drewes (1980). The top of the model is the ground surface. Parts A–J show the model cut away along an east–west line that moves progressively northward into the model domain. The model area is indicated in figure 13.

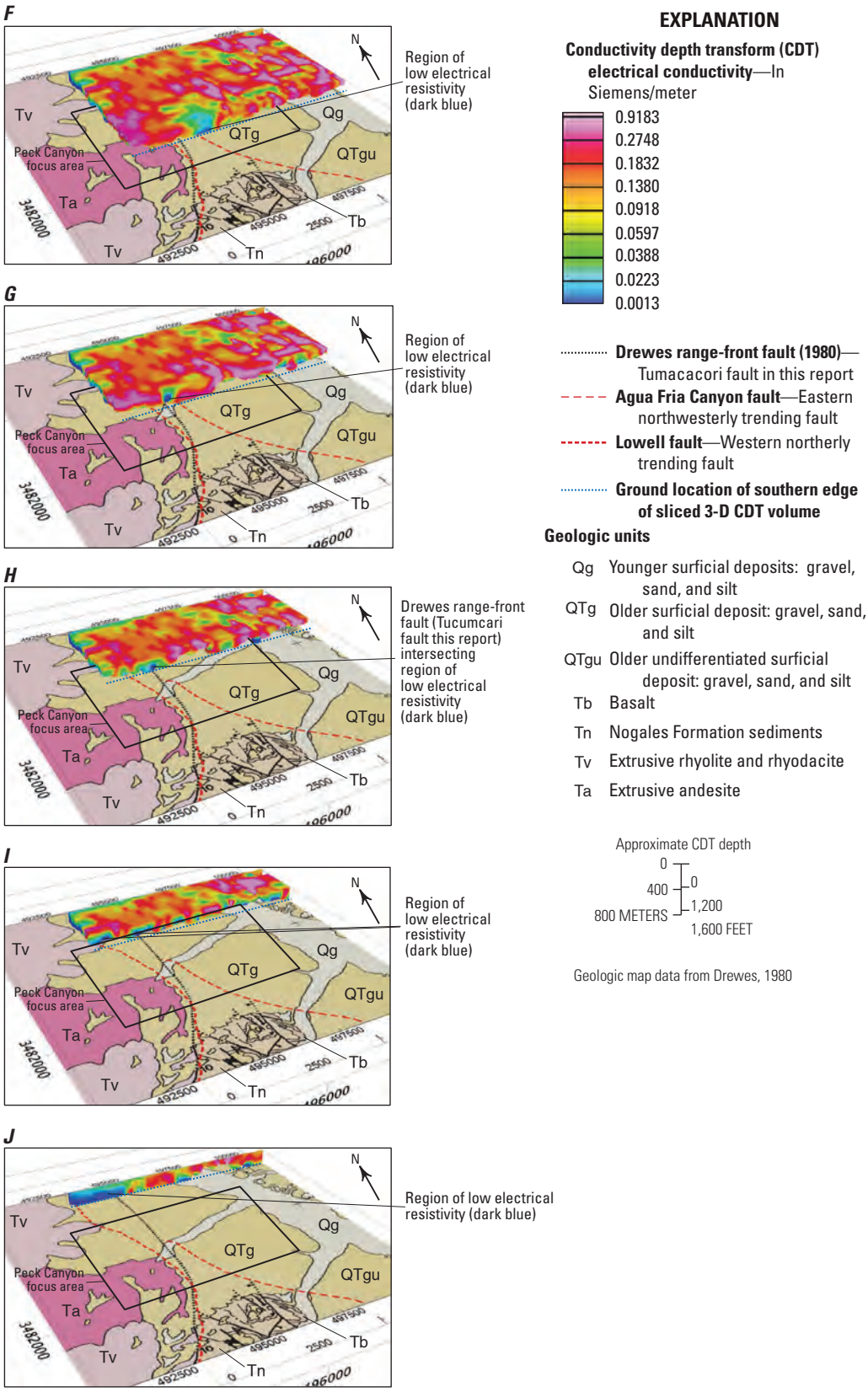

Figure 21.—Continued Conductivity depth transforms transformed to a voxel volume representation in the Peck Canyon focus area displayed over the geologic map of Drewes (1980). The top of the model is the ground surface. Parts A–J show the model cut away along an east–west line that moves progressively northward into the model domain. The model area is indicated in figure 13.

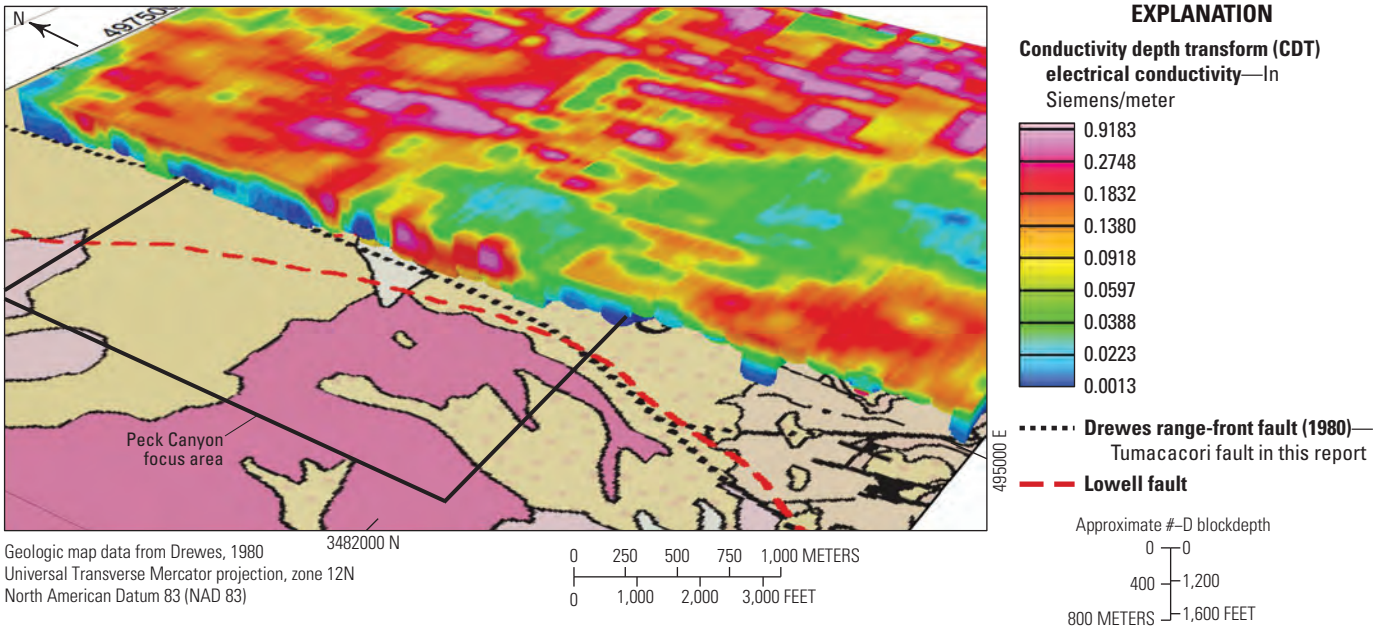

Figure 22. Three-dimensional volume representation of the conductivity depth transforms (CDTs) viewed looking to the northeast. Geology from Drewes (1980). The CDT volume is cut on a north–south line at an easting of 495000 and shows the low electrical conductivity at depth along the Tumacacori fault, north of Peck Canyon.

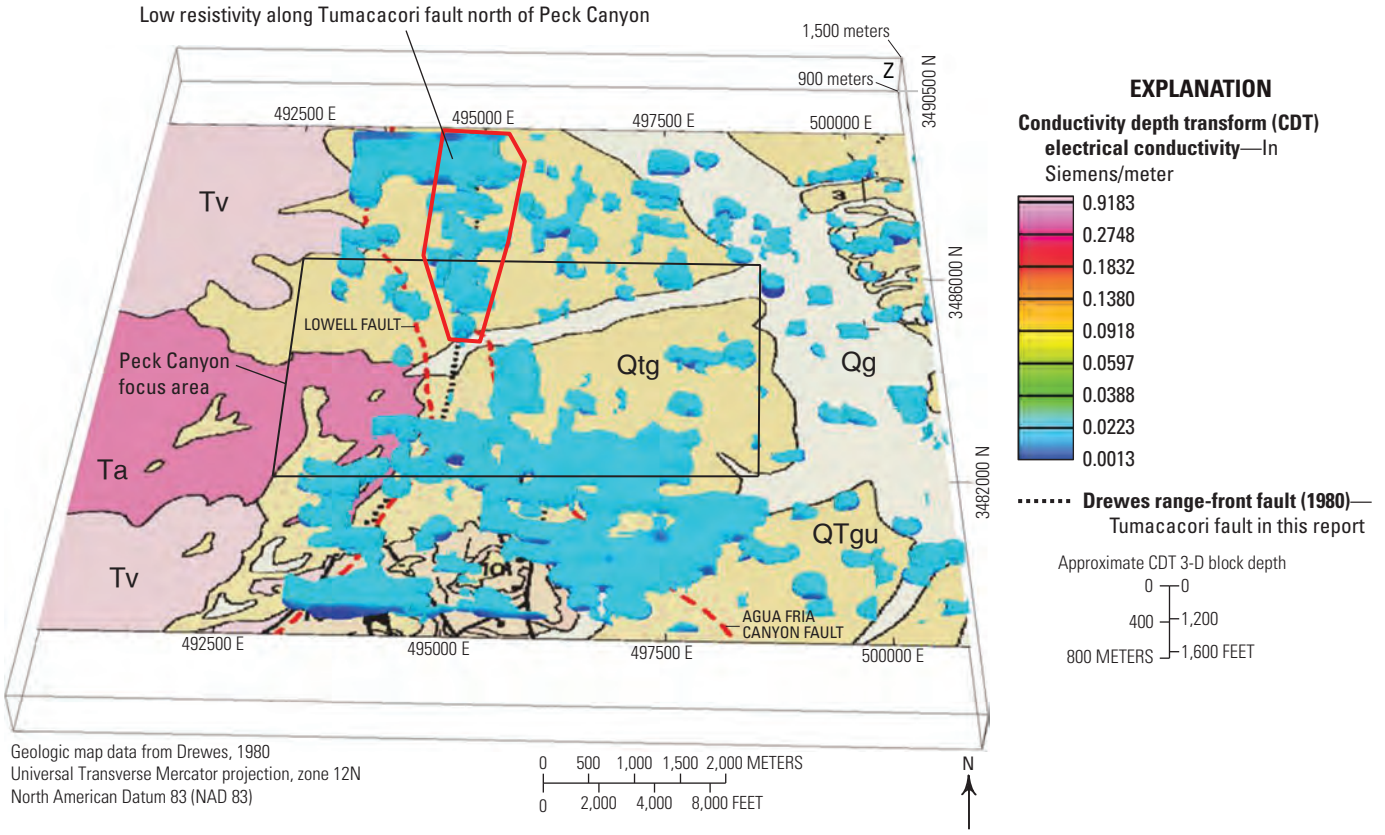

Figure 23. Three-dimensional volume representation of the conductivity depth transforms (CDTs) viewed looking to the northeast plotted over geology of Drewes (1980). The CDT volume is cut on a north–south line at an easting of 495000 and shows the low electrical conductivity at depth along the Tumacacori fault north of Peck Canyon.

whereas the Lowell fault strikes north-northwest. Farther north, the Lowell fault merges back into the Tumacacori fault (fig. 7; sheet 1). Both faults continue to the north along a well-defined zone of low electrical conductivity and are likely to be pathways for groundwater movement from south to north. The Agua Fria Canyon fault (figs. 7 and 23) also follows a zone of low electrical conductivity in the Peck Canyon focus area. This fault defines the eastern edge of a zone of very low electrical conductivity that reaches the surface in Peck Canyon and then likely combines with both the Tumacacori and the Lowell faults (figs. 21*B* and 23).

Evaluating Water Sources in the Potrero Creek Wetlands Through Geologic, Geophysical and Isotopic Investigations

Introduction

The lower end of Potrero Creek near its confluence with Nogales Wash is a remnant ciénega system (desert stream marshland) in the upper Santa Cruz River basin (fig. 24*A*). Currently, wetland environments cover an area of about 0.14 square kilometers (km^2), but they were larger prior to residential, commercial, and recreational development. Ecological habitats vary in different areas of the system and include willow bosque, bulrush marsh, and cattail/open-water marsh environs (EnviroNet Inc., 1997). Just up-gradient of the wetlands, Potrero Creek quickly transitions into a dry wash that only flows during infrequent rain events. In contrast, wetlands are supported by a perennial source of water not directly dependent on surface-water flow within the drainage.

The history of wetland activity has not been investigated through excavations or coring. Archaeological evidence along Nogales Wash and the Santa Cruz River suggests that the Hohokam peoples occupied the area between 700 and 900 CE, leaving pottery remains from both northern and southern cultures (Reinhard and Shipman, 1978). The first written documentation of the wetland is from the 1775–1776 colonizing expedition of Juan Bautista de Anza who led several hundred settlers from Sonora, Mexico, to San Francisco, CA. The expedition camped at the wetlands (Camp #13) described as "Las Lagunas" on October 14 of 1775 (Teggart, 1913).

Two aquifers have been recognized in the vicinity of the wetlands (EnviroNet Inc., 1997). The lower phreatic aquifer is regionally extensive and actively pumped from older Pleistocene to Miocene alluvium by the City of Nogales. The shallower aquifer is interpreted to be perched on top of a claystone unit in the Mariposa member of the Nogales Formation that impedes downward movement of surface water. The source for the perched water was suspected to be surface water that infiltrated during periods of active streamflow, or from leakage of anthropogenic activities upgradient in the Meadow Hills subdivision. It was noted that lower Potrero Creek has been heavily modified by construction activities that have led to alteration and degradation of wetland dynamics by fragmentation, draining, and damming (EnviroNet Inc., 1997).

Given the ecological importance of the site and the context provided by the geologic framework developed in this report, we investigated the hydrologic conditions and water sources supporting perennial surface water in the Potrero wetlands. A better understanding of the hydrogeologic system is critical for protecting this rare wetland habitat from further urban development. To meet this objective, we analyzed a combination of three types of data including (1) detailed geologic mapping in the wetlands vicinity to identify structures capable of localizing groundwater discharge; (2) geochemical fingerprinting of water within the wetlands and comparing it to other known water sources; and (3) evaluation of geophysical data to better understand subsurface features that may control ponding of water at the surface. Fingerprinting perennial surface water within the wetlands largely relies on analyses of natural isotopes of strontium and uranium ($^{87}Sr/^{86}Sr$ and $^{234}U/^{238}U$) that have been shown elsewhere to be particularly useful in distinguishing multiple water sources and mixing relations in arid wetland environments (Paces and Wurster, 2014; Drexler and others, 2014; Paces and others, 2019). Those heavy radiogenic isotopes are largely immune from near-surface physical, biological, and chemical processes that can cause substantial modification of other constituents. In addition, light, stable isotopes constituting the water molecule ($\delta^{18}O$ and $\delta^{2}H$) were also determined for a subset of samples to evaluate the effects of mixing and evaporation on water in different parts of the wetlands. Finally, Sr-isotope analyses of dilute-acid leachates of two samples from the Jurassic quartz monzonite of Mount Benedict were determined to assess whether groundwater flow along fractures in contact with intrusive rocks at depth (fig. 24*B*) could be a possible source of Sr dissolved in wetland samples.

Geology

The Potrero wetlands are present near the mouth of Potrero Canyon where they are inset into older Quaternary and Tertiary sediments (fig. 24). The geologic setting of the Potrero wetlands is complex, but an important geologic feature likely supporting water in the wetlands is the Grand Avenue fault (fig. 24). The fault juxtaposes Jurassic monzonite and overlying tuffaceous sandstone of the Proto Canyon member of the Nogales Formation in the footwall, against claystone, sandstone, and conglomerate units of the Mariposa member of the Nogales Formation, and overlying Quaternary to Holocene sediments in the hanging wall (fig. 24*B*). Nogales Formation sediments and late Miocene to early? Pleistocene gravels are fractured and faulted in the wetlands area. Numerous other faults are exposed in the Grand Avenue fault footwall and include several west and northwest-dipping faults and some east-and-southwest-dipping faults in the Potrero wetlands area

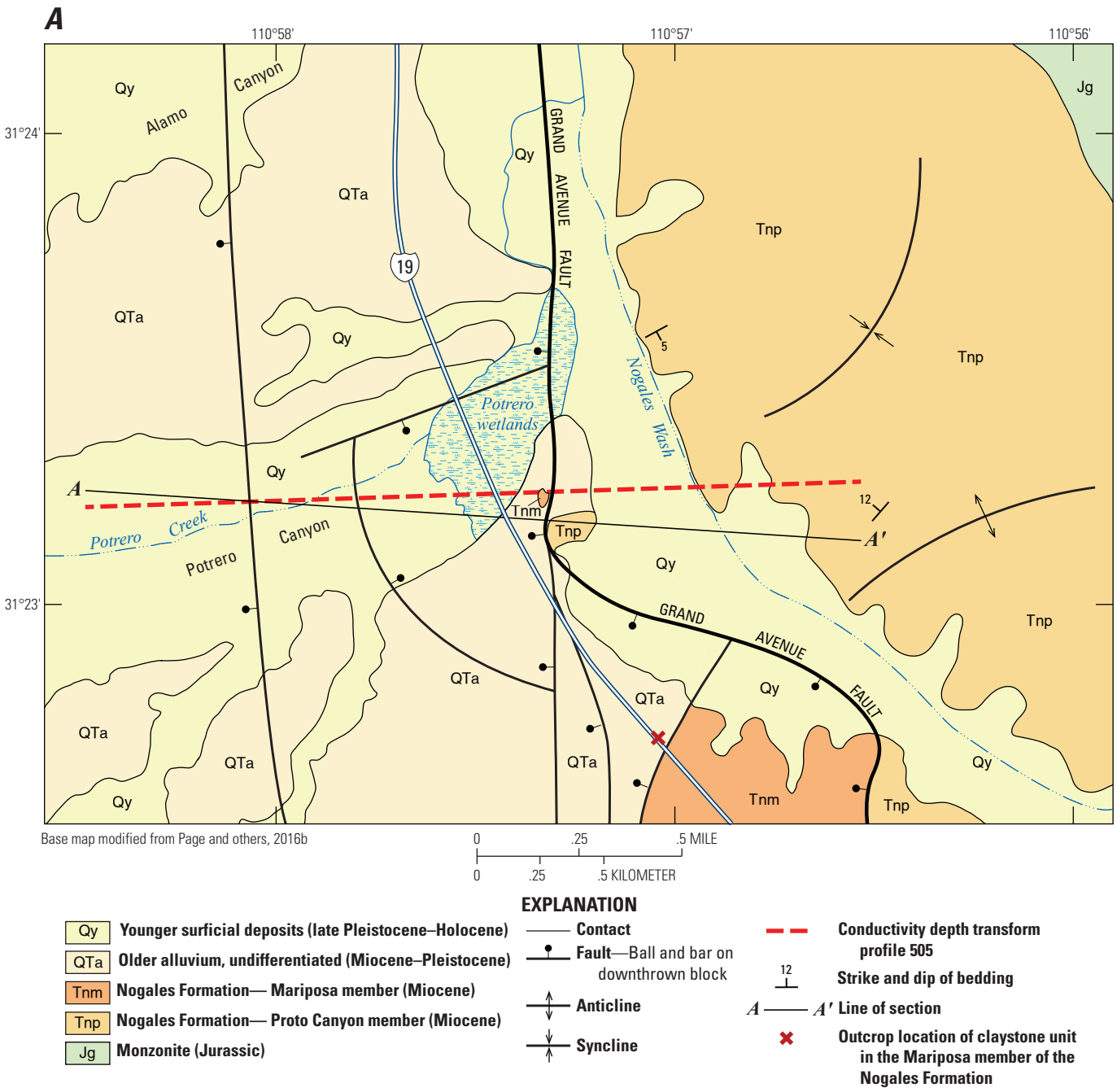

Figure 24. *A*, Simplified geologic map and *B*, cross section of the Potrero wetlands and vicinity after Page and others (2016b). The A–A' transect in A denotes the cross section profile in B.

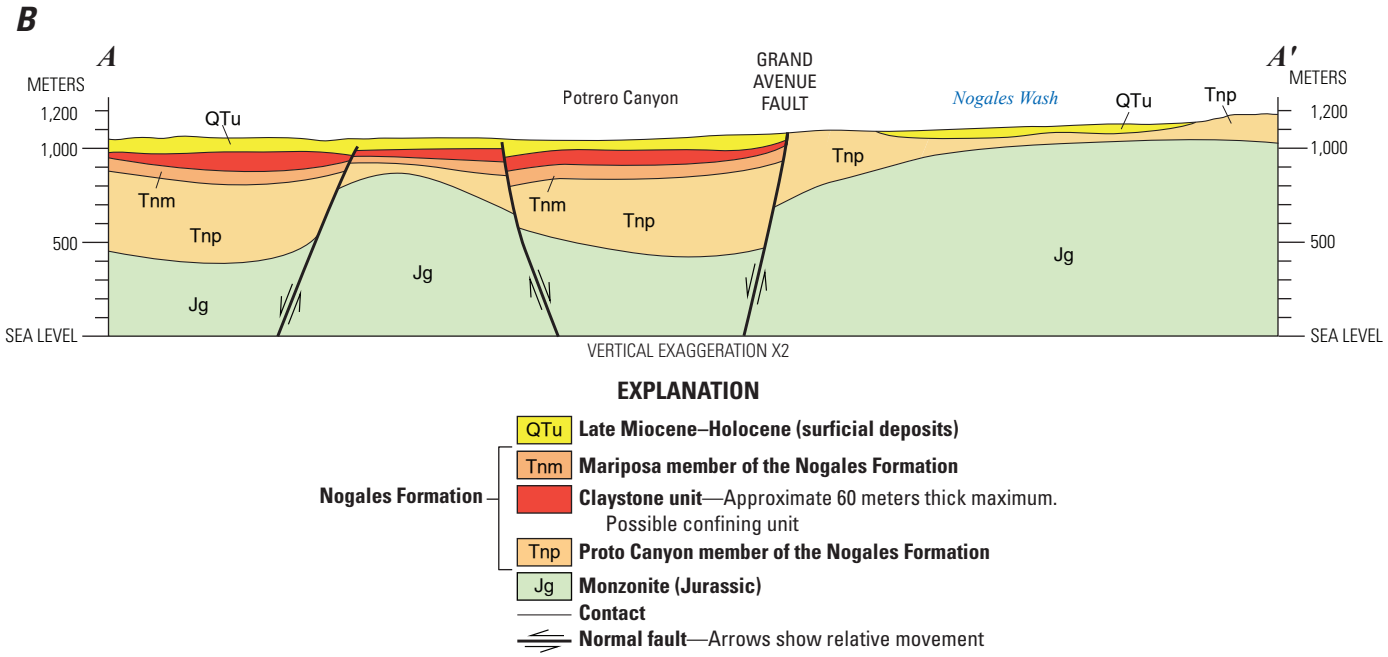

Figure 24.—Continued *A*, Simplified geologic map and *B*, cross section of the Potrero wetlands and vicinity after Page and others (2016b). The A–A′ transect in A denotes the cross section profile in B.

(fig. 24*A*). These faults likely formed by accommodating a major bend in the Grand Avenue fault, from mostly north to northwest-striking in the south, to north-striking in the wetlands area and northward (fig. 24).

In the Potrero wetlands area (fig. 24), the thickness of latest Miocene to Holocene basin fill deposits is estimated to be about 30 to 80 m in the hanging wall of the Grand Avenue fault. We interpret the Mariposa member of the Nogales Formation to underlie the basin fill deposits in the wetlands area based on exposures of the member along I–19 south of the junction of Potrero Canyon and Nogales Wash (fig. 24*A*). The thickness of the Nogales Formation (including the Mariposa and Proto Canyon members) in the subsurface at this location is estimated at about 500 to 600 m based on thicknesses of the members at nearby locations in the Nogales area. Page and others (2016b) mapped a major claystone unit in the lower part of the Mariposa member interpreted to underlie the latest Miocene to early? Pleistocene basin fill gravels in the subsurface of the wetlands area. The interpretation is partly based on local exposures of the claystone about 0.5 km south of the wetlands along I–19 (the closest claystone outcrop location is shown in the southern part of fig. 24*A*). Farther south, the claystone is well exposed and about 60 m thick along the south side Mariposa Road, between I–19 and Grand Avenue (Page and others, 2016b).

Hydrology

Potrero Creek, a tributary of the upper Santa Cruz River, is an ephemeral desert stream draining highlands of the Pajarito Mountains to the southwest. Headwater areas reach altitudes up to 1650 m and drop to an altitude of 1100 m at its confluence with Nogales Wash, about 20 km to the northwest. Several seeps at higher elevations (Russell Spring, Adobe Spring, Bull Spring) suggest that recharge may support scattered discharge of possible perched systems; however, Potrero Creek is a losing stream over nearly its entire length until it reaches the wetlands. Anomalously large and lengthy precipitation events have caused sporadic flooding in the lower reaches of Potrero Creek (for example, rain associated with Hurricane Heather in 1977; Aldridge and Eychaner, 1984); however, rainy seasons in most years do not result in substantial ephemeral streamflow.

Depth to water measurements in wells drilled into the regional phreatic aquifer along Potrero Creek (Arizona Department of Water Resources, 2021) define a potentiometric surface at a depth of about 44.5 m at well UMW3 immediately north of the western end of the wetlands (dark blue dashed line in fig. 25). This depth is consistent with base level altitudes for the Santa Cruz River measured on the east side of Mount Benedict near the mouth of Guevavi Canyon (light blue dotted line in fig. 25). In contrast, perennial water is present at the surface within the main wetlands area, even when streamflow in Potrero Creek is absent. The discrepancy between measured water levels is consistent with a perched system supporting perennial wetlands that is some 40–50 m above the regional potentiometric surface. Wells have not been drilled within the

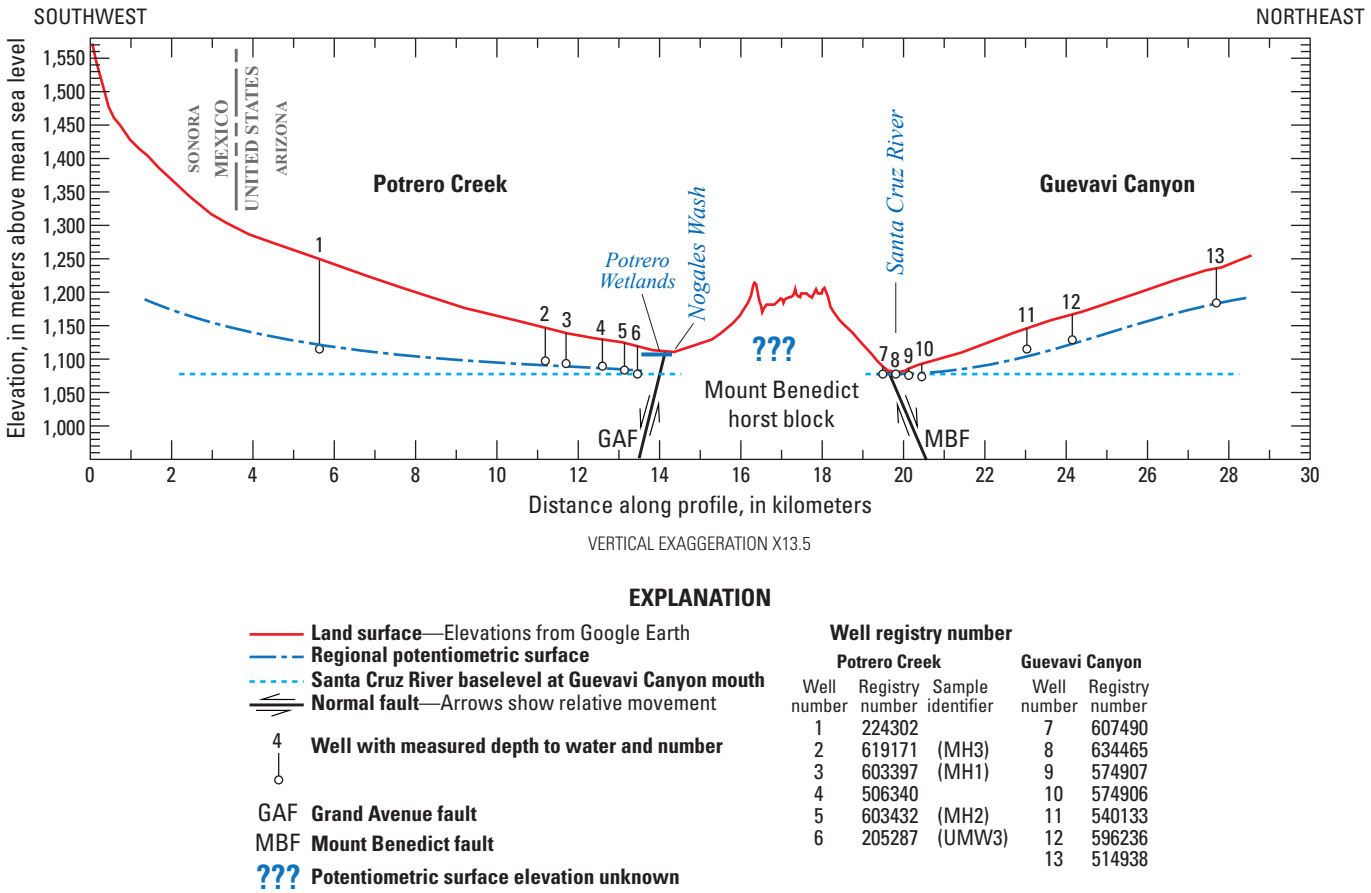

Figure 25. Elevation profile across the project area showing land surface along active channels in Potrero Creek and Guevavi Canyon (thick red lines), water table in the unconfined regional phreatic aquifer (dashed blue line) along Potrero and Guevavi Canyons, and the baselevel of the main drainage system (upper Santa Cruz River) at the approximate latitude of the Potrero wetlands (dotted blue line). See figure 24*A* for approximate profile location. Land surface elevations are from Google Earth. Depth to water measurements are from actively pumped wells within or close to the active channel of each drainage (data from Arizona Department of Water Resources, 2021). Normal faults on either side of the Mount Benedict horst block are shown schematically based on mapping by Page and others (2016b).

wetlands to investigate strata underlying this area, so the nature and geometry of the perching horizon is not well understood. In addition, the source of perched water remains unknown along with the question of whether Nogales Formation sediments between the wetlands confining unit and the underlying regional water table are saturated or unsaturated.

Climate

Climate in the upper Santa Cruz valley is characterized by low annual precipitation, moderate winters, and hot summers. Monthly average high temperatures range from 18.3 degrees Celsius (°C) in January to 35.6 °C in June with average low temperatures of 2.2 °C and 12.8 °C, respectively. Average annual precipitation is 457 millimeters (mm) but is unevenly distributed throughout the year (climate data from https://www.wunderground.com/history/monthly/us/az/nogales). Two distinct seasons of precipitation supply moisture to the upper Santa Cruz River basin, with slightly greater precipitation in the summer than in the winter (Sellers and Hill, 1974). The summer rainy season (shaded bands on fig. 26*A*) occurs in July and August (monthly averages of 105 and 112 mm, respectively) and is derived from monsoonal flow patterns bringing moist tropical airmasses up from the south (Webb and Betancourt, 1992). Precipitation is delivered primarily from widespread convective thunderstorm activity. Winter moisture is delivered from December through March and is caused primarily by trailing cold fronts associated with large low-pressure weather systems that bring cyclonic storm centers originating in the Pacific Ocean (Lee and others, 1999). Dissipation of tropical cyclones can also cause widespread and intense precipitation events in late summer and early fall (Webb and Betancourt, 1992). Late winter and spring typically constitute the dry season with only a few, widely scattered precipitation events leading into monsoon season.

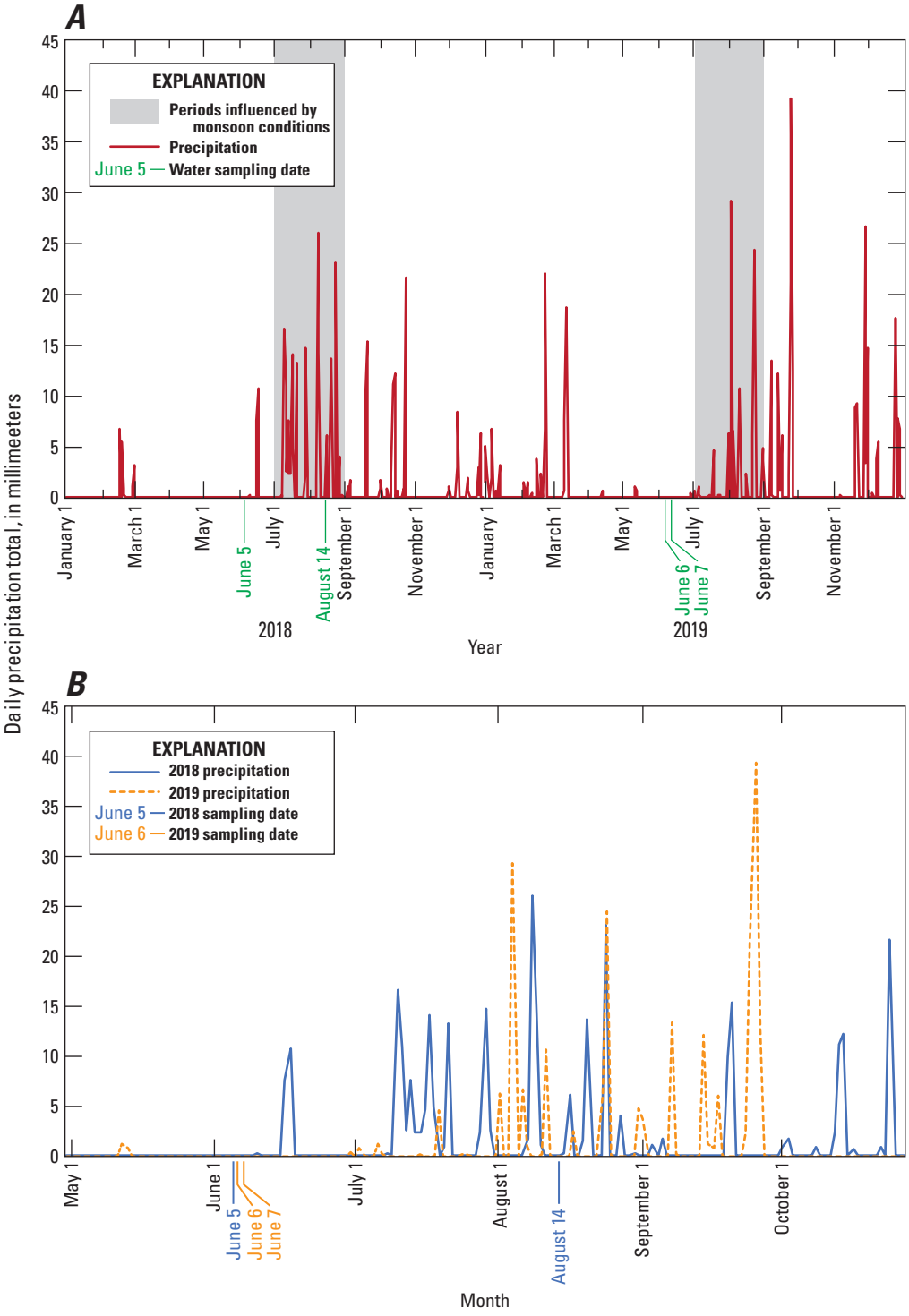

Figure 26. Daily precipitation data from Nogales International Airport Station from January 1, 2018 to December 31, 2019. *A,* Continuous two-year record showing water sampling dates (green arrows) and periods considered to be influenced by monsoon climate conditions (gray shading). *B,* Precipitation record for two separate years overlapped on the same time scale to compare differences in timing of precipitation events between years. Sample dates are shown by blue or orange vertical arrows and correspond to sample dates given in table 4. Precipitation data are from https://www.wunderground.com/history/monthly/us/az/nogales.

Evaporation and evapotranspiration are important processes affecting wetland areas where surface water is present and groundwater is shallow enough to be reached by roots of phreatophytic plants. Detailed evapotranspiration studies have not been conducted in the Potrero wetlands, but elsewhere in the semi-arid southwest, research has shown that rates of evaporation are substantially higher than input from annual precipitation and that evapotranspiration plays a major role in transferring moisture to the atmosphere in vegetated areas (Laczniak and others, 1999; Reiner and others, 2002; DeMeo and others, 2003, 2008; Leenhouts and others, 2006). Water levels in marshy areas drop substantially during summer growing seasons and recover when vegetation becomes dormant in winter given a constant input of water throughout the year. Therefore, even if open water is reduced or not present in the Potrero wetlands, water supply is still able to maintain phreatophytic vegetation.

Samples

Water samples are grouped into three categories based on their locations and sample type and include well water from the Meadow Hills area, surface water from Nogales Wash, and surface water associated with the Potrero wetlands (fig. 27). All samples are from the west side of the Mount Benedict horst block except for one sample from the Santa Cruz River collected near the Buena Vista Ranch (fig. 1).

Groundwater samples from wells were collected at the specified well heads while pumps were operating. Two well-water samples were collected as samples of opportunity from spigots tapping pipelines within the wetlands (LL6–2 and LL6–7) that contained domestic or commercial supply associated with the Valle Verde Water Company system. Specific origins of water in those samples are not known, but the samples likely represent a mixture from active wells pumping from the regional aquifer. Samples of surface water flowing in Nogales Wash were collected from upstream segments lined with concrete (Morley Avenue) and downstream unlined segments. Streamflow is largely sustained by effluent from domestic or commercial water use in the communities of both Nogales, Sonora, and Nogales, Arizona. Nogales Wash samples were collected from both upgradient and downgradient sides of the confluence with Potrero Creek.

Surface water collected from the Potrero wetlands includes samples from upstream areas on the west side of I–19 to downstream areas where streamflow along Potrero Creek exits the wetlands and flows beneath North Grand Avenue towards its confluence with Nogales Wash (fig. 28). The landscape on the west side of the wetlands has been substantially modified by construction of ponds associated with the now-closed Palo Duro Creek golf course. Several of those ponds with open water were also sampled for this study (near sample PW2 on fig. 28). The main, open-water marsh at Las Lugunas de Anza was sampled several times during the study, along with a sample of ponded water from the bosque behind a warehouse constructed on landfill at the site. Water exits the main marsh area to the northeast as streamflow focused in a short riparian segment before flowing through a small residential area. The amount of water present in the wetlands varies seasonally in large part due to variations in evapotranspiration of marsh vegetation. Potrero Creek quickly becomes a dry wash immediately west of the wetlands area (near well UMW3 on fig. 28), with active streamflow occurring only during large, infrequent precipitation events.

Analytical Methods

Strontium and Uranium Isotopes in Water Samples

Analytical methods are described in detail elsewhere (Paces and others, 2020, Data Repository item 2020023) and summarized here. Samples of well water and surface water were collected during site visits in June and August of 2018 and June of 2019. Samples were filtered in the field at 0.45 micrometers (μm) and acidified in the U.S. Geological Survey radiogenic isotope laboratory in Denver, Colorado using ultra-pure nitric acid. Sr concentrations were determined by isotope dilution after adding a known amount of ^{84}Sr-enriched spike to a separate small aliquot of water that was processed separately from ^{87}Sr/^{86}Sr determinations. Both Sr and U isotopic compositions were determined on a single aliquot of 112 to 278 grams (g) of water weighed into open PFA Teflon™ beakers after which a known amount of highly purified, mixed ^{233}U-^{236}U tracer solution was added. Samples equilibrated with spike during evaporation, followed by dissolution in 7M nitric acid. Purification of U and Sr used separate ion chromatographic columns piggy-backed on top of each other so that the initial effluent from the upper U columns (Biorad™ AGIx8 resin) was fed onto lower Sr columns (Eichrom™ Sr resin). Columns were separated after the first 3 resin volumes of nitric acid wash and processed separately to complete U and Sr purification.

All U and Sr isotope measurements were made on a Thermo Finnigan™ Triton thermal-ionization mass spectrometer. Uranium isotope measurements were made in peak-jumping mode using a single discrete-dynode secondary electron multiplier behind a retarding potential quadrupole (RPQ) energy filter. Raw U isotope ratios were corrected for mass fractionation using the known ^{236}U/^{233}U value in the spike solution as well as for spike contributions and procedural blanks (<10 pg). Measured ^{234}U/^{235}U values were converted to ^{234}U/^{238}U assuming a ^{238}U/^{235}U of 137.88 and were normalized relative to a standard value of 0.0000529 (±0.0000011 two sigma error [2σ]) for the ^{234}U/^{238}U atomic ratio in the international U-isotope standard, NIST SRM4321B, run during the same barrel. Corrected ratios were translated to picomole abundances of each isotope and converted to [^{234}U/^{238}U] (square brackets used to denote activity ratios) using values for radioactive decay constants given by Steiger and Jäger (1977) and Cheng and others (2013). Analyses of NIST SRM4321B determined over the same period yielded an average ^{234}U/^{235}U value of 0.007300±0.000013 (2SD; N=83), which is within analytical uncertainty of the certified value of 0.007294±0.000028. Results for an in-house

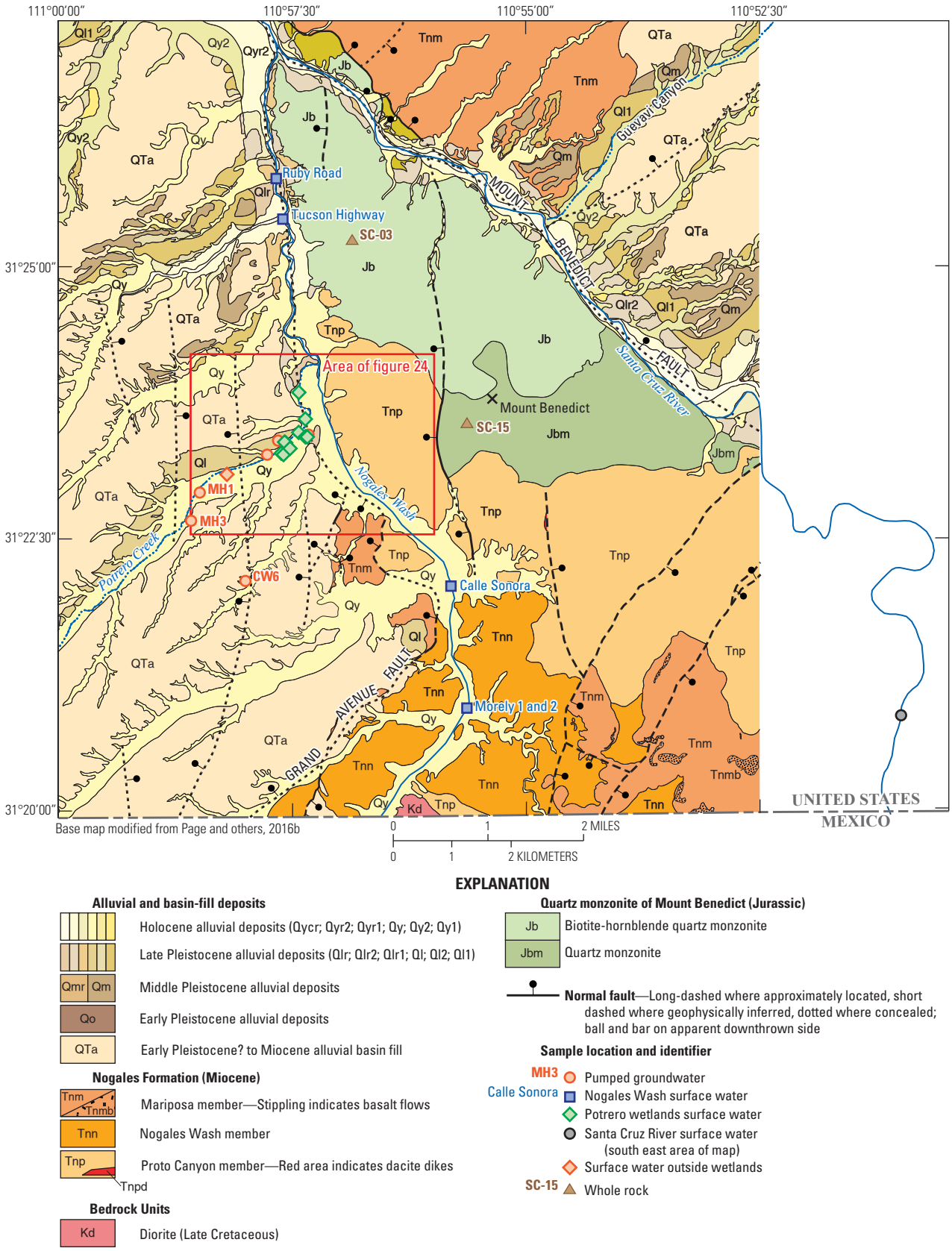

Figure 27. Location of water sampling sites shown along with simplified geologic map units from Page and others (2016b). Unlabeled symbols in the main wetlands area are identified in figure 28.

Figure 28. Satellite image of Potrero Creek wetlands and vicinity (same approximate area as fig. 24) showing locations of surface and well water sampling sites. Trace of the Grand Avenue fault is approximated from Page and others (2016b). Satellite image is from Google Earth.

secular equilibrium standard derived from a 69-Ma-old uranium ore from the Schwartzwalder Mine (Ludwig and others, 1985) yielded results that are consistent with the secular equilibrium value of 1.0000 (average [$^{234}U/^{238}U$] value of 0.9973±0.0022 [2SD; N=15]). All uncertainties presented herein are given at the 95 percent confidence level (±2σ). Unspiked Sr measurements were run in dynamic triple-peak-jumping mode using static Faraday cup measurements in each jump. The $^{87}Sr/^{86}Sr$ ratios were corrected for instrumental fractionation using the accepted $^{86}Sr/^{88}Sr$ value of 0.1194. Data for $^{84}Sr/^{86}Sr$ were also collected during the same run to monitor the effectiveness of the fractionation correction. Total-process blank contributions for Sr varied between 50 and 100 picograms. The mean $^{87}Sr/^{86}Sr$ value obtained for the NIST international Sr-isotope standard, SRM987, collected over the period of analysis was 0.710251±0.000007 (2SD; N=94), which is within uncertainty of the accepted value of 0.710248±0.000006 (McArthur and others, 2001). Fractionation-corrected $^{87}Sr/^{86}Sr$ values determined for unknown samples were corrected for instrument bias by applying the same normalization factor required to adjust the average measured SRM987 obtained for each batch of analyses to the accepted value. A secondary Sr-isotope standard, EN–1, analyzed as an unknown with each batch, yielded a mean $^{87}Sr/^{86}Sr$ value of 0.709174±0.000006 (2SD; N=83) which is identical to the accepted value of 0.709174±0.000002 (±2×standard error; McArthur and others, 2006).

Strontium Isotopes in Whole-Rock Leachates

To characterize the $^{87}Sr/^{86}Sr$ composition of the most hydrologically accessible components present in the crystalline rocks of the Mount Benedict horst block, whole-rock powders from two outcrop samples were subjected to leaching. Approximately 0.5 g of powder was wetted with 1.5 milliliters of 5 N acetic acid for 4 hours at room temperature. After centrifuging at 10,000 rpm, the supernate was transferred to separate Teflon vials, after which the solids were returned to their original vials. Remaining solids were then washed with 0.05 N nitric acid and centrifuged a second time. The supernate was added to the original acetic solution. The resulting solutions were evaporated to dryness, dissolved in concentrated nitric acid, dried down, and re-dissolved in 7 N nitric acid. Sr was purified from those solutions following the same methods explained above.

Stable Isotopes in Water Samples

The isotopic composition of oxygen and hydrogen were measured on a subset of water samples collected in June of 2019 at the University of Arizona Environmental Isotope Laboratory. Values of $\delta^{18}O$ were determined using the CO_2 equilibration method on an automated sample preparation device attached directly to a Finnigan Delta S mass spectrometer. Values of $\delta^{2}H$ were measured using an automated chromium reduction device (H-Device) attached to the same mass spectrometer. The values were corrected based on internal laboratory standards, which are calibrated to results for the international isotope standards Vienna Standard Mean Ocean Water (VSMOW) and Standard Light Antarctic Precipitation (SLAP) analyzed on the same instrument. The analytical precision for $\delta^{18}O$ and $\delta^{2}H$ measurements is 0.16 per mil and 1.2 per mil, respectively (2σ). Water isotopic results are reported using standard δ-per mil notation relative to accepted values for VSMOW.

Results

Resulting radiogenic (Sr and U) and stable (O and H) isotope data as well as descriptive information for well-water and surface-water samples are presented in table 4 and are available in electronic form elsewhere (Paces, 2021). Those data provide a powerful means of assessing relations between groundwater derived from wells pumping the regional alluvial aquifer and surface water present in the Potrero Creek wetlands.

Strontium and Uranium Isotope Data

Concentrations of dissolved ions in surface water can be strongly affected by evaporation, transpiration, precipitation of mineral phases, and dilution by rainwater. Furthermore, U concentrations are highly sensitive to redox conditions; U in its tetravalent state in reducing water is largely insoluble whereas U in its hexavalent state under oxidizing conditions is highly soluble as uranyl complexes. U and Sr concentrations in water samples exhibit a wide range of values with substantial overlap between groups (table 4; fig. 29). U concentrations are elevated (3.5–6.1 nanograms per gram [ng/g]) in most samples of regional groundwater and in surface water from Nogales Wash and the Santa Cruz River. However, U concentrations are much lower (0.01–0.5 ng/g) in water from wells at UMW3 and MH2. The large difference is attributed to reducing conditions present in those wells, although it is unclear whether the phenomenon is only present within the well stems or more broadly within parts of the aquifer. In contrast, Sr concentrations in MH2 water samples are identical to those in other regional groundwater samples. Wetlands surface water yielded a wide range of both U and Sr concentrations that reflect variations in both space and time. In contrast, isotope data cluster more tightly in two distinct groups characteristic of groundwater in the regional phreatic aquifer, and water present in the wetlands (table 4; fig. 30). The isotopic compositions of water from Nogales Wash are intermediate between those two groups.

Values for $^{87}Sr/^{86}Sr$ for water in the regional aquifer (orange circles in fig. 30) span a relatively narrow range from 0.70847 to 0.70860, indicating that groundwater in the shallow phreatic aquifer has a common hydrologic source and is well mixed within the phreatic aquifer. This is also true for [$^{234}U/^{238}U$] values, except for samples from two wells (MH2 and UMW3), which have activity ratios that are much higher (4.28 and 4.43, respectively) than those from other wells in this group (1.80–2.11). U concentrations in those same

Table 4. Strontium (Sr) and uranium (U) concentrations and Sr, U, oxygen (O), and hydrogen (H) isotopic compositions of groundwater and whole rock leachates from the upper Santa Cruz River basin near Potrero Creek, Nogales, Arizona.

[Data are from Paces (2021). Well depth, perforation interval, and last known depth to water data from the Arizona Department of Water Resources Well Registry (https://azwatermaps.azwater.gov/WellReg). Concentrations of Sr and U were determined by isotope dilution with analytical uncertainties estimated to be less than 1 percent of the value given. Atomic ratios of $^{86}Sr/^{88}Sr$ were corrected for instrumental fractionation using a $^{86}Sr/^{88}Sr$ value of 0.1194 and normalized for instrument bias by adjusting measured $^{87}Sr/^{86}Sr$ values obtained for the SRM987 Sr standard of 0.710248. Delta values for $\delta^{87}Sr$ were calculated as $(({}^{87}Sr/{}^{86}Sr_{[unknown]} \div {}^{87}Sr/{}^{86}Sr_{[seawater]})\text{-}1)\times 1000$, where $^{87}Sr/^{86}Sr_{[seawater]} = 0.709174$. Two sigma (2σ) uncertainties are plus or minus (±) 0.02 per mil (‰). Measured atomic $^{234}U/^{235}U$ ratios were corrected for instrument mass fractionation, spike addition, and total process blank and converted to $^{234}U/^{238}U$ assuming an atomic $^{238}U/^{235}U$ equal to 137.88. Atomic $^{234}U/^{238}U$ were then converted to activity ratios (denoted with square brackets) using ^{234}U and ^{238}U decay constants from Cheng and others (2013) and Steiger and Jäger (1977). Measured $^{18}O/^{16}O$ and $^{2}H/^{1}H$ ratios in unknown samples (R_U) were converted to delta notation ($\delta^{18}O_{VSMOW}$ and $\delta^{2}H_{VSMOW}$, respectively) using $((R_U/R_S)\text{-}1)\times 1000$, where R_S is the same ratio measured in the international standard material Vienna Standard Mean Ocean Water (SMOW). ID, identification; WGS84, World Geodetic System 1984; ft, feet; bls, below land surface; ng/g, nanogram per gram; #, number; —, not measured; UMI, United Musical Instruments; N/A, not applicable; Ave, avenue; Rd, road; Dr, drive]

Lab name	Short ID	Site name	Sample date	Latitude (degrees, WGS84)	Longitude (degrees, WGS84)	Well depth (ft bls)	Perforation interval (ft bls)	Last known depth to water (ft bls)	Sr concentration (ng/g)	$^{87}Sr/^{86}Sr$	±2σ	$\delta^{87}Sr$ (‰)	U concentration (ng/g)	$[^{234}U/^{238}U]$	±2σ	$\delta^{18}O_{VSMOW}$ (‰)	$\delta^{2}H_{VSMOW}$ (‰)
Well water																	
AZ18-MH2	MH2	Meadow Hills #2	6/5/2018	31.38743	–110.96257	400	90–400	122.5	168	0.708466	0.000009	–1.00	0.505	4.278	0.009	—	—
AZ18-MH3	MH3	Meadow Hills #3	6/5/2018	31.37742	–110.97678	450	unknown	160	143	0.708579	0.000010	–0.84	5.77	1.796	0.004	—	—
AZ18-MH1	MH1	Meadow Hills #1	6/5/2018	31.38174	–110.97548	430	unknown	167.3	162	0.708535	0.000009	–0.90	5.57	1.979	0.004	—	—
AZ18-CW6	CW6	Coronado Well #6	6/5/2018	31.36811	–110.96671	1005	460–960	285.5	173	0.708561	0.000010	–0.86	5.46	2.055	0.004	—	—
AZ18-UMW3	UMW3	UMI Monitoring Well UMW3 (shallow)	6/5/2018	31.38967	–110.96048	160	130–160	146	104	0.708595	0.000010	–0.82	0.154	4.434	0.019	—	—
AZ18-UMW3D	UMW3D	UMI Monitoring Well UMW-3D (deep)	6/5/2018	31.38967	–110.96048	320	300–320	146.3	72.5	0.708551	0.000010	–0.88	0.0112	2.113	0.018	—	—
LL190606-2	LL6-2	Valle Verde pipeline at Las Lagunas de Anza	6/6/2019	31.39061	–110.95482	unknown	unknown	unknown	152	0.708495	0.000009	–0.96	4.33	1.963	0.005	–8.44	–59.9
LL190606-7	LL6-7	Spigot at Potrero wetland	6/6/2019	31.38951	–110.95936	unknown	unknown	unknown	158	0.708528	0.000009	–0.91	5.55	1.935	0.004	–8.22	–59.9
LL190607-2	LL7-2	Stagnant-water golf pond west of wetlands	6/7/2019	31.38481	–110.9706	N/A	N/A	0	145	0.708687	0.000009	–0.69	1.94	2.462	0.005	–0.90	–22.3
Surface water—Santa Cruz River																	
AZ18-SCR(BVR)	SCR	Santa Cruz River near Buena Vista Ranch	6/5/2018	31.34828	–110.84978	N/A	N/A	0	322	0.708396	0.000010	–1.10	4.15	1.87	0.004	—	—
Surface water—Nogales Wash																	
AZ18-NW(Morley)	NW-Morley1	Nogales Wash near Highway 82/Morley Ave	6/5/2018	31.3494	–110.92722	N/A	N/A	0	327	0.709219	0.000010	0.06	5.01	1.576	0.003	—	—
NgWsh@Hwy82	NW-Morley2	Nogales Wash (lined)	8/14/2018	31.34878	–110.92719	N/A	N/A	0	328	0.708963	0.000009	–0.30	3.90	1.568	0.003	—	—
NgWsh@C.Sonora	NW-Sonora	Nogales Wash at Calle Sonora	8/14/2018	31.36745	–110.92961	N/A	N/A	0	320	0.708963	0.000009	–0.30	3.51	1.587	0.004	—	—
NgWsh@RubyRd	NW-Ruby	Nogales Wash/Potrero Creek at Ruby Rd Bridge	8/14/2018	31.42992	–110.96068	N/A	N/A	0	269	0.70878	0.000009	–0.56	6.29	1.397	0.003	—	—
NgWsh@TucsonRd	NW-Tucson	Nogales Wash at Tucson Rd	8/14/2018	31.42374	–110.95934	N/A	N/A	0	272	0.708786	0.000009	–0.55	6.07	1.395	0.003	—	—
Surface water— Potrero Creek wetlands																	
AZ18-Wtlds	PW	Country Club Dr and Frontage Rd—open water	6/5/2018	31.38863	–110.95894	N/A	N/A	0	195	0.709676	0.000010	0.71	3.19	1.264	0.003	—	—
PotrWtlds 1	PW1	Country Club Dr and Frontage Rd—open water	8/14/2018	31.38864	–110.95889	N/A	N/A	0	199	0.709645	0.000009	0.66	0.0551	1.264	0.011	—	—
PotrWtlds 2	PW2	Fresh water golf pond in wetlands	8/14/2018	31.38778	–110.95992	N/A	N/A	0	182	0.709398	0.000009	0.32	0.0552	1.422	0.004	—	—

Table 4. Strontium (Sr) and uranium (U) concentrations and Sr, U, oxygen (O), and hydrogen (H) isotopic compositions of groundwater and whole rock leachates from the upper Santa Cruz River basin near Potrero Creek, Nogales, Arizona.—Continued

[Data are from Paces (2021). Well depth, perforation interval, and last known depth to water data from the Arizona Department of Water Resources Well Registry (https://azwatermaps.azwater.gov/WellReg). Concentrations of Sr and U were determined by isotope dilution with analytical uncertainties estimated to be less than 1 percent of the value given. Atomic ratios of $^{86}Sr/^{88}Sr$ were corrected for instrumental fractionation using a $^{86}Sr/^{88}Sr$ value of 0.1194 and normalized for instrument bias by adjusting measured $^{87}Sr/^{86}Sr$ values obtained for the SRM987 Sr standard of 0.710248. Delta values for $\delta^{87}Sr$ were calculated as $((^{87}Sr/^{86}Sr_{[unknown]} \div {}^{87}Sr/^{86}Sr_{[seawater]})-1)\times1000$, where $^{87}Sr/^{86}Sr_{[seawater]} = 0.709174$. Two sigma (2σ) uncertainties are plus or minus (±) 0.02 per mil (‰). Measured atomic $^{234}U/^{235}U$ ratios were corrected for instrument mass fractionation, spike addition, and total process blank and converted to $^{234}U/^{238}U$ assuming an atomic $^{238}U/^{235}U$ equal to 137.88. Atomic $^{234}U/^{238}U$ were then converted to activity ratios (denoted with square brackets) using ^{234}U and ^{238}U decay constants from Cheng and others (2013) and Steiger and Jäger (1977). Measured $^{18}O/^{16}O$ and $^{2}H/^{1}H$ ratios in unknown samples (R_U) were converted to delta notation ($\delta^{18}O_{VSMOW}$ and $\delta^{2}H_{VSMOW}$, respectively) using $((R_U/R_S)-1)\times1000$, where R_S is the same ratio measured in the international standard material Vienna Standard Mean Ocean Water (SMOW). ID, identification; WGS84, World Geodetic System 1984; ft, feet; bls, below land surface; ng/g, nanogram per gram; #, number; —, not measured; UMI, United Musical Instruments; N/A, not applicable; Ave, avenue; Rd, road; Dr, drive]

Lab name	Short ID	Site name	Sample date	Latitude (degrees, WGS84)	Longitude (degrees, WGS84)	Well depth (ft bls)	Perforation interval (ft bls)	Last known depth to water (ft bls)	Sr concentration (ng/g)	$^{87}Sr/^{86}Sr$	±2σ	$\delta^{87}Sr$ (‰)	U concentration (ng/g)	$[^{234}U/^{238}U]$	±2σ	$\delta^{18}O_{VSMOW}$ (‰)	$\delta^{2}H_{VSMOW}$ (‰)
PotrWtlds 3	PW3	Las Lagunas de Anza—ponded water	8/14/2018	31.39046	–110.95551	N/A	N/A	0	308	0.709552	0.000009	0.53	1.79	1.242	0.003	—	—
Surface water— Potrero Creek wetlands—Continued																	
LL190606-1	LL6-1	Las Lagunas de Anza—ponded water	6/6/2019	31.39037	–110.95524	N/A	N/A	0	383	0.7095422	0.000009	0.52	2.24	1.251	0.003	–0.56	–23.1
LL190606-3	LL6-3	Las Lagunas de Anza—ponded water	6/6/2019	31.39124	–110.95695	N/A	N/A	0	193	0.709681	0.000009	0.72	0.215	1.299	0.004	–5.11	–44.3
LL190606-4	LL6-4	Potrero Creek at N Grand Ave—streamflow	6/6/2019	31.39324	–110.95561	N/A	N/A	0	171	0.709644	0.000009	0.66	0.303	1.275	0.007	–6.25	–48.6
LL190606-5	LL6-5	Potrero Creek at Cochise Dr—streamflow	6/6/2019	31.3973	–110.95714	N/A	N/A	0	173	0.709631	0.000009	0.64	0.501	1.251	0.004	–5.90	–48.3
LL190606-6	LL6-6	Country Club and Frontage Rd, north—ponded water	6/6/2019	31.38953	–110.95934	N/A	N/A	0	131	0.7095536	0.000009	0.54	0.158	1.278	0.004	–5.68	–46.8
LL190606-8	LL6-8	Country Club and Frontage Rd, south—ponded water	6/6/2019	31.38859	–110.95865	N/A	N/A	0	132	0.7095073	0.000009	0.47	0.205	1.309	0.004	–5.23	–45.7
LL190607-1	LL7-1	Las Lagunas de Anza—ponded water	6/7/2019	31.39042	–110.95555	N/A	N/A	0	354	0.7095586	0.000009	0.54	1.82	1.244	0.003	–1.50	–25.7
LL190607-3	LL7-3	Freshwater golf pond in wetlands	6/7/2019	31.38783	–110.96013	N/A	N/A	0	104	0.7095331	0.000009	0.51	0.0770	1.403	0.005	–6.46	–50.4
Bedrock leachates																	
SC3 MtBenMonz	SC3L	Mount Benedict monzonite leachate	N/A	31.42025	–110.9479	N/A	N/A	N/A	—	0.711719	0.000008	3.59	—	—	—	N/A	N/A
SC15 MtBenMonz	SC15L	Mount Benedict monzonite leachate	N/A	31.39213	–110.92717	N/A	N/A	N/A	—	0.715747	0.000009	9.27	—	—	—	N/A	N/A

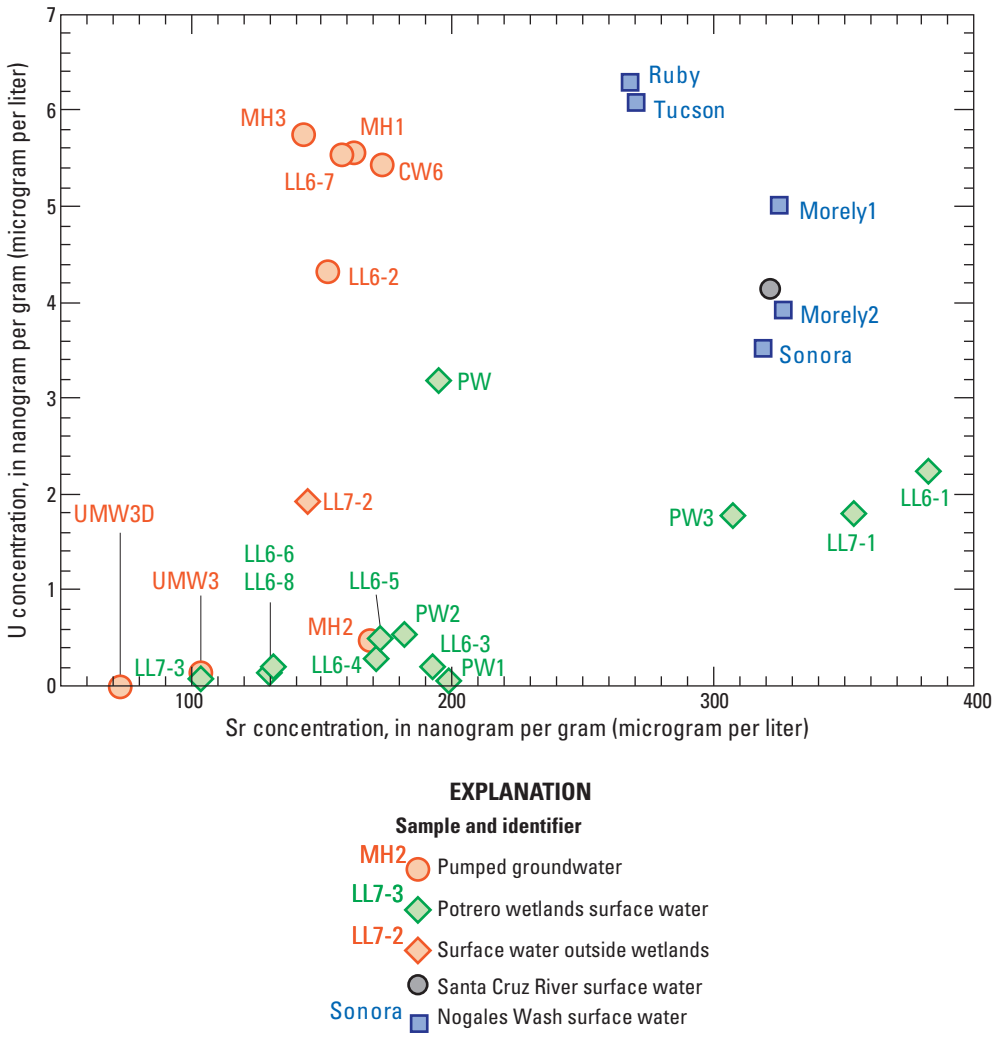

Figure 29. Concentrations of strontium (Sr) and uranium (U) for water sampled in the Potrero wetlands and vicinity. Data are from table 4.

samples are substantially lower than values in other well water samples (table 4). Elevated [$^{234}U/^{238}U$] values can be obtained under conditions of low-flow (very low water/rock ratios) or in reducing environments where the tiny amounts of ^{234}U derived through alpha-recoil processes are less overwhelmed by the dominant isotope ^{238}U transported in solution (Andrews and Kay, 1982; Paces and others, 2002; Suksi and others, 2006; Porcelli, 2008). A well-water sample from the same location as UMW3 but pumped from a deeper completion interval (300–320 feet for UMW3D versus 130–160 feet for UMW3) has a [$^{234}U/^{238}U$] value within the range observed for other regional aquifer samples (2.113), even though it has the lowest observed U concentration (0.011 µg/g). Regardless of the cause for the two anomalously high U-isotopic compositions, $^{234}U/^{238}U$ values for the remaining samples and $^{87}Sr/^{86}Sr$ results for all samples are consistent enough to characterize the regional groundwater source pumped from the shallow phreatic aquifer.

Wetlands water samples have distinctly lower [$^{234}U/^{238}U$] and higher $^{87}Sr/^{86}Sr$ relative to water in the upgradient regional aquifer (fig. 30). The range of values forms a crude linear array that trends toward the main cluster of regional groundwater compositions. In addition, compositions show a tendency to correlate with location within the wetlands (fig. 28). Samples collected in June of 2019 that have the highest $^{87}Sr/^{86}Sr$ are from areas east of I–19 on the north edge of the wetlands where stream flow was active (samples LL6–3, LL6–4, and LL6–5). During the same collection period, samples with the lowest $^{87}Sr/^{86}Sr$ values were from areas to the west of I–19 including ponds associated with the former Palo Dura Creek golf course (samples LL6–6, LL6–8, and LL7–3). Samples PW and PW1 collected in 2018 just west of I–19 yielded some of the highest $^{87}Sr/^{86}Sr$ compositions whereas another 2018 sample from the pond further west (sample PW2) yielded the lowest $^{87}Sr/^{86}Sr$ and highest [$^{234}U/^{238}U$] values. Samples collected from the open marsh

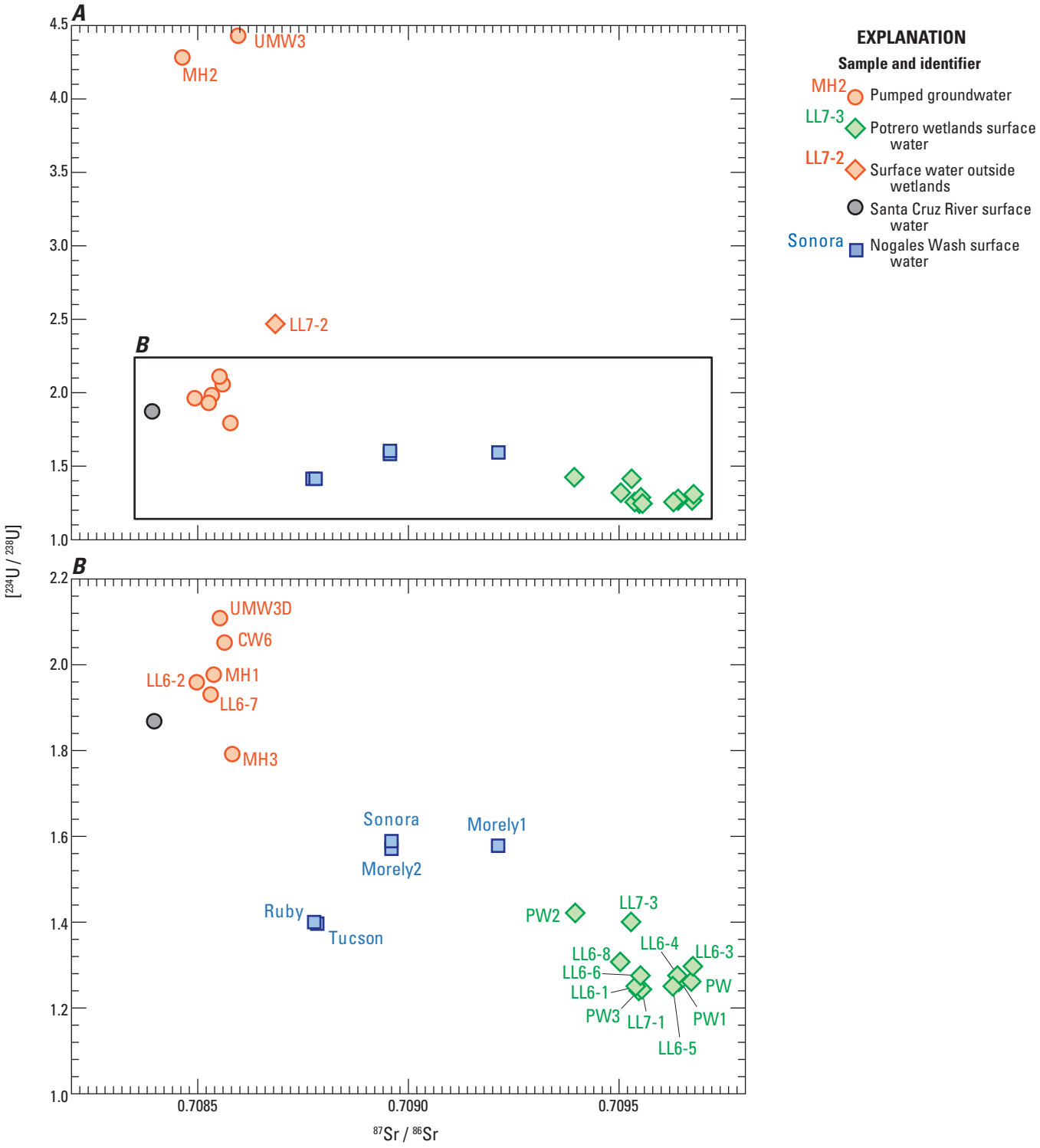

Figure 30. Isotopic compositions of strontium and uranium for water sampled in the Potrero wetlands and vicinity. Square brackets for [$^{234}U/^{238}U$] values denote activity ratios. *A.* All samples from table 4. *B.* Samples with [$^{234}U/^{238}U$] values less than 2.2.

at Las Lagunas de Anza (samples PW3, LL6–1, and LL7–1) consistently had intermediate compositions regardless of sample date. Strontium and uranium isotopic compositions of those samples contrast greatly with results from a sample of stagnant water evaporating in a shallow pond constructed on the former golf course approximately 1 km further upstream (sample LL7–2 in fig. 28). Isotope data for that sample are similar to results observed for regional groundwater (fig. 30*A*) even though depths to the regional water table in this area are between 37 m at well MH2 and 51 m at well MH1 (wells 5 and 3, respectively on fig. 25).

Two samples of streamflow in Nogales Wash taken in June and August of 2018 from a concrete-lined segment along Morley Road have nearly identical [$^{234}U/^{238}U$] values but distinctly different $^{87}Sr/^{86}Sr$ values (fig. 30*B*) indicating variable sources of Sr in urban runoff at different times. However, both U- and Sr-isotopic compositions are identical in samples taken on the same day from lined (sample Morley2) and unlined sites (sample Sonora) within approximately 2 km. In contrast, two samples of Nogales Wash water collected on the same day downstream of the confluence with Potrero Creek (samples Ruby and Tucson on fig. 30*B*) have distinctly lower $^{87}Sr/^{86}Sr$ and [$^{234}U/^{238}U$] values relative to upstream samples. Those shifts in Nogales Wash water composition are inconsistent with the addition of either Potrero wetlands water or domestic/industrial sources originating from pumped well water. Other tributary stream flows contributing to Nogales Wash are not apparent in this reach.

Groundwater samples from wells constructed in the quartz monzonite of Mount Benedict were not available for analysis in this study. However, acetic-acid leachates of whole-rock powder were analyzed to evaluate whether Sr available to groundwater in the horst-block fracture system is more- or less-radiogenic than water in the Nogales-formation aquifer. Results for two separate rock samples had $^{87}Sr/^{86}Sr$ values of 0.711719 and 0.715747 (table 4), which are substantially more radiogenic than values in either Meadow Hills regional groundwater (average and 2SD value of 0.70856±0.00013, N=9) or in Potrero wetlands water (0.70958±0.00016, N=12).

Oxygen and Hydrogen Isotopes

Stable isotopes of water were analyzed for a subset of samples collected in June of 2019. Results of groundwater from the regional aquifer sampled from pipelines crossing the wetlands have compositions that plot close to the global meteoric water line (samples LL6–2 and LL6–7 in fig. 31). In contrast, surface water from wetland sites have O and H compositions that are substantially heavier (less negative). Wetland water samples form a well-defined evaporation trend that projects back toward values for regional groundwater with a slope that suggests evaporation under relative humidity conditions of about 60 percent. Samples from the main area of open water associated with the marsh at Las Lagunas de Anza (samples LL6–1 and LL7–1 in fig. 28) are subject to the highest degrees of pan evaporation and have the heaviest δ^2H and $\delta^{18}O$ compositions of all wetlands water samples. Other surface water samples have intermediate compositions along the evaporation trend that are not clearly related to their position within the wetland system. The one sample of stagnant water from a nearly dried-up pond west of the wetlands (sample LL7–2 on fig. 28) has the heaviest δ^2H and $\delta^{18}O$ values and does not fall on the same regression line defined by wetland water. A two-point regression (orange dashed line on fig. 31) yields a slope that is consistent with large degrees of pan evaporation of a regional Meadow Hills groundwater source at low relative humidity.

Discussion

Unlike stable-isotope compositions that can undergo large amounts of fractionation by physical processes, heavy radiogenic isotopes of Sr and U are particularly well suited as natural hydrologic tracers in arid environments (Paces and Wurster, 2014). Both trace elements are relatively abundant in most near-surface water sources and have isotopic compositions that can vary widely in different hydrologic reservoirs. Those differences are easy to measure at high levels of precision and accuracy, and because mass differences between isotopes are small compared to the total mass for both elements, isotope ratios remain largely unaffected by near-surface processes. Therefore, the combination of Sr and U isotopic compositions in surface waters has the potential to provide a particularly powerful tool for evaluating source contributions where processes such as pan evaporation, plant transpiration, mineral precipitation, and solute gains and losses via sorption-desorption can have dramatic effects on chemical and stable-isotope compositions of near-surface water.

Data shown in figure 30 indicate that water supplying the Potrero wetlands has Sr and U isotopic compositions that cannot be derived from either regional groundwater in the shallow phreatic aquifer to the west, or from sources related to surface flow in Nogales Wash. Streamflow in Potrero Creek was not available for sampling in this study but is not expected to represent a viable source for perennial wetlands given its highly intermittent nature. Furthermore, if Potrero Creek streamflow was the source of water supporting wetlands, it would have to reach the area of perching without contributing substantial recharge through streambed losses along the way. Under that scenario, regional phreatic groundwater along the wash should show contributions of wetlands-like water to samples pumped from upgradient wells, which is not observed in the cluster of orange circles in figure 30. In addition, most wetlands samples (9 of 12) were obtained in June after months-long periods that lacked precipitation events (fig. 26). Therefore, a perennial source from groundwater discharge rather than streamflow is required to maintain saturated conditions in the wetlands.

Source Mixing in Wetland Water

The trend of isotopic variation in wetland surface-water samples is interpreted to reflect mixtures of two groundwater

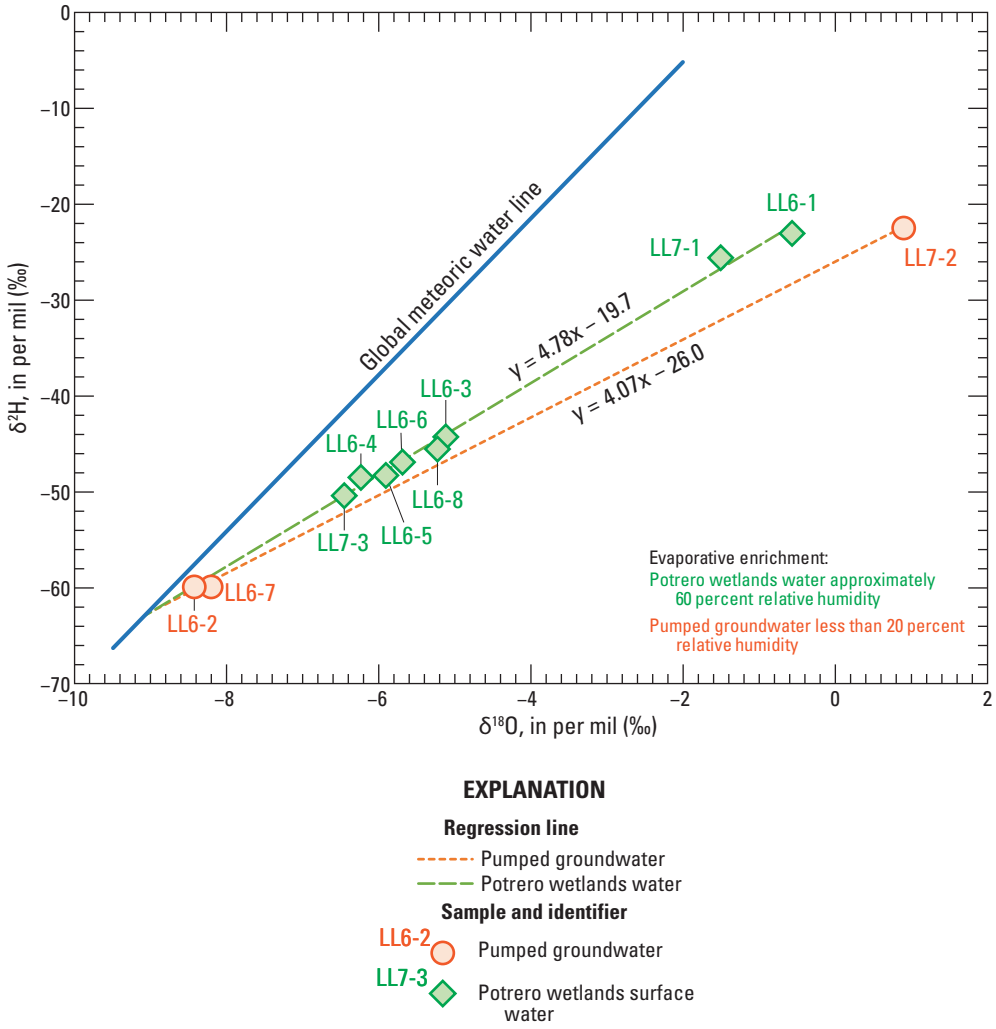

Figure 31. Isotopic compositions of hydrogen (δ^2H) and oxygen ($\delta^{18}O$) in water samples collected in June of 2018. Data are given in delta notation relative to the international reference standard Vienna standard mean ocean water (VSMOW) and are listed in table 4. Global meteoric water line is from Rozanski and others (1993). The dash-dot evaporation curve is based on the regression of 8 wetlands data points shown as green diamonds. The dotted evaporation curve represents a two-point regression based on the average of pumped groundwater samples LL6–2 and LL6–7 and water from a stagnant pond on the former golf course (sample LL7–2). Estimates of relative humidity for evaporation curves are from Clark and Fritz (1997). Sample locations are shown in figure 28.

sources. The endmember representing the regional phreatic aquifer is interpreted to have a composition similar to data for well-water shown in figure 30*B* with $^{87}Sr/^{86}Sr$ values between 0.70849 and 0.70858 and $[^{234}U/^{238}U]$ values between 1.796 and 2.113. The larger variability in $[^{234}U/^{238}U]$ is assumed to be influenced by borehole redox conditions in individual wells that are not pumped frequently. Samples of water from two Val Verde supply pipes crossing the wetlands (samples LL6–2 and LL6–7) have compositions that are very similar to values obtained from water sampled at the MH1 wellhead and most likely represent this endmember.

The other endmember supplying groundwater to the Potrero wetlands is best represented by samples with the highest $^{87}Sr/^{86}Sr$ and lowest $[^{234}U/^{238}U]$ compositions (fig. 30*B*). Those samples include LL6–3, LL6–4, and LL6–5 from the main wetland area collected in June 2019, and samples PW and PW1 immediately west of I–19 collected in June and August of 2018 (fig. 28). Unlike those samples, open water from the same site as PW and PW1 collected in June of 2019 (samples LL6–6 and LL6–8) had distinctly lower $^{87}Sr/^{86}Sr$ values compared to the previous year. Water from ponds further west (PW2 and LL7–3) consistently had lower $^{87}Sr/^{86}Sr$ values and elevated $[^{234}U/^{238}U]$ that fall along a trend in the

direction toward the compositions of water in the regional phreatic aquifer. Samples of open water from the managed marsh at Las Lagunas de Anza collected in both 2018 and 2019 (PW3, LL6–1 and LL7–1) have nearly identical intermediate $^{87}Sr/^{86}Sr$ values regardless of sample date.

Spatial and temporal differences in $^{87}Sr/^{86}Sr$ and $[^{234}U/^{238}U]$ imply that mixing proportions of the two endmembers vary depending on either natural or anthropogenic factors. Binary mixing relations between wetlands and regional phreatic groundwater sources depend on both the concentrations and isotopic compositions of Sr and U in each of the end members (Faure and Mensing, 2005; Paces and Wurster, 2014).

Sr concentrations as well as $^{87}Sr/^{86}Sr$ and $[^{234}U/^{238}U]$ compositions are restricted for both end members; however, U concentrations are more variable. This results in a wide range of binary mixing curves between different wetlands endmembers, several of which are illustrated in figure 32*A*. Surface water samples with the highest $^{87}Sr/^{86}Sr$ values (assumed to be closest to the wetlands supply endmember) have U concentration values ranging from 0.06 to 3.19 ng/g (micrograms per liter [µg/L]). Mixtures of endmembers represented by samples PW and MH1 (3.19 and 5.57 ng/g, respectively) will plot along a curve that closely predicts the isotopic composition of sample LL7–3 from the western-most wetland pond presuming the mixture consists of approximately 13 percent MH1 water and 87 percent PW water. In contrast, mixtures of samples LL6–3 with only 0.22 ng/g U and MH1 do not yield results that come close to predicting isotopic compositions of other wetland water samples. In that case, small additions of MH1 to LL6–3 water cause rapid increases in $[^{234}U/^{238}U]$ values due to the order-of-magnitude lower U concentration in sample LL6–3. If U concentrations were higher in the wetlands endmember than that in MH1, hyperbolic mixing curves would bow downward (dashed gray curves in fig. 32*A*). Compositions similar to sample PW2 can be obtained if the PW endmember has a U concentration of 7 ng/g and contributes about 72 percent of the supply. Mixtures of PW and MH1 endmembers can only produce compositions like those measured in the Las Lagunas de Anza open marsh (samples PW3, LL6–1, and LL7–1) if the U concentrations in PW are much higher (30 ng/g or more).

The simple binary mixing relations shown in figure 32*A* are intended to investigate potential causes for small, but significant, variations in $^{87}Sr/^{86}Sr$ and $[^{234}U/^{238}U]$ compositions throughout wetland waters. This mechanism is difficult to justify if groundwater supply has low U concentrations. However, the large amount of organic matter present in the warm, perennial wetland environment likely creates reducing conditions that are effective at removing U from solution. Given the large range of U concentrations observed in the wetlands water samples (0.06 to 3.19 ng/g) and an effective process for removing U once water reaches the surface, groundwater supplying perennial water to Potrero wetlands is expected to be oxidizing in nature and able to carry between 2 and 10 ng/g U as determined in sample PW (fig. 28). Reducing conditions in the organic-rich environment can rapidly convert soluble hexavalent uranyl complexes to insoluble tetravalent U forms, removing U without changing its $[^{234}U/^{238}U]$ isotopic composition (Drexler and others, 2014). Under this scenario, we interpret that groundwater supplying the wetlands is distinct from regional phreatic groundwater sampled in upgradient wells. We are unaware of any natural causes for unconfined groundwater present at depths of 40–50 m in wells immediately west of the wetlands to reach the surface. However, water management practices by the City of Nogales may occasionally contribute pumped water to the west side of the wetland system resulting in the variable compositions and apparent mixing trends observed in figure 32.

Variations in δ^2H and $\delta^{18}O$ in wetland waters might also provide some indication of mixing between wetland groundwater supply and groundwater in the regional phreatic aquifer. However, all wetland water samples fall along the evaporation trend show in figure 31 that projects toward less-fractionated compositions similar to samples LL6–2 and LL6–7 near the global meteoric water line. Streamflow out of the main wetlands area sampled beneath Grand Avenue and further downstream (samples LL6–4 and LL6–5 in fig. 28) have values that plot at the more negative end of the spectrum. In contrast, standing water in the main wetland area (sample LL6–3) and in ponds just west of I–19 (samples LL6–6 and LL6–8) have progressively more evaporated compositions, although far from the most evaporated samples in the suite representing open water in the main Las Lagunas de Anza marsh (samples LL6–1 and LL7–1). Open water sampled from the pond nearest the former golf course (sample LL7–3) has the least-evaporated composition and reflects higher amounts of water pumped from the regional phreatic aquifer. Higher $^{87}Sr/^{86}Sr$ and lower $[^{234}U/^{238}U]$ values for this sample are consistent with mixing of those two water sources (fig. 32*A*). Even though isotopes of the water molecule should behave conservatively in mixtures of different components, the inconclusive relations observed for δ^2H and $\delta^{18}O$ results show how near-surface processes can complicate their use for discriminating sources in arid wetland environments.

Presence of Local Perching Horizon

Perennial water supporting phreatophytic vegetation in the wetlands, even during dry months, requires a reliable source of water supply. One likely source is upwelling groundwater from depths beneath the phreatic aquifer resulting in discharge along faults and fractures associated with the Grand Avenue fault (fig. 24). Surface-water flow through the wetlands begins in Potrero Creek just west of its intersection with I–19 and into the main wetlands area between I–19 and Grand Avenue. Surface water flows out of the main wetlands area, beneath Grand Avenue, and to the northeast until it joins Nogales Wash (fig. 28). This area is coincident with the Grand Avenue fault where fractures likely serve as conduits for water to reach the surface and spread out above a shallow, impermeable claystone unit.

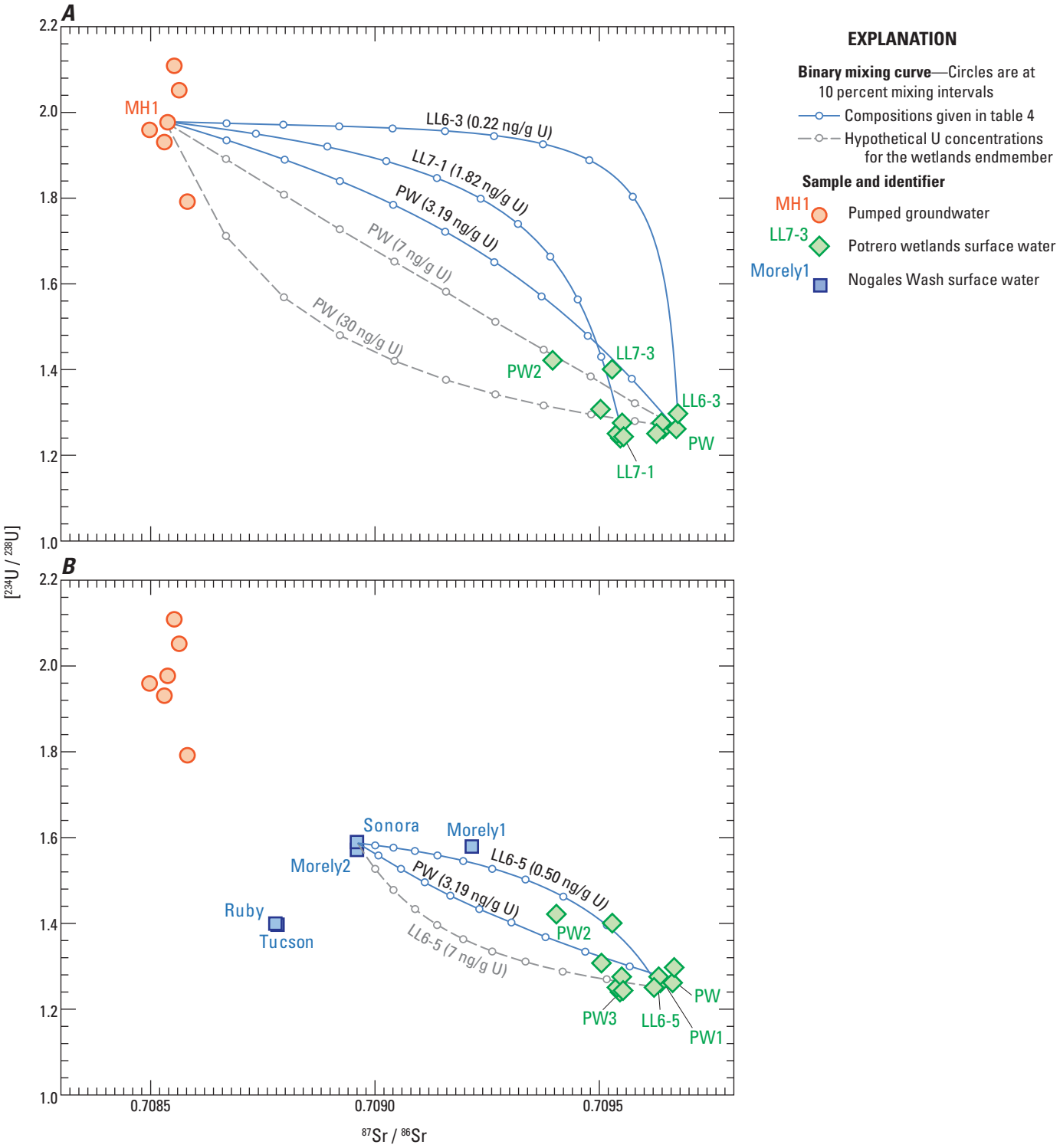

Figure 32. Simple binary mixing curves for selected strontium (Sr) and uranium (U) concentrations and $^{87}Sr/^{86}Sr$ and $[^{234}U/^{238}U]$ compositions for endmembers described in text. Predicted compositions will plot along hyperbolic-shaped curves shown with small open circles at 10 percent mixing intervals. Solid blue lines use compositions given in table 4. Dashed gray lines assume hypothetical U concentrations for the wetlands endmember. (A) Mixing relations between groundwater endmembers representing the regional phreatic aquifer (sample MH1) and for wetlands water (samples PW, LL6–3, and LL7–1). (B) Mixing relations between upgradient stream flow in Nogales Wash (sample Sonora) and wetlands outflow (samples PW and LL6–5). Mixing calculations are described in Paces and Wurster (2014).

The presence of a claystone unit in the wetlands subsurface is interpreted from transient electromagnetic conductivity depth transform (CDT) profiles (figs. 33 and 34) (Bultman and Page, 2016). Those data indicate the presence of high electromagnetic conductive zones that are consistent with saturated claystone within the Mariposa member of the Nogales Formation (bright magenta colors in figs. 33 and 34). Those data indicate the presence of zones of high electromagnetic conductive zones that are consistent with saturated claystone within the Mariposa member of the Nogales Formation (bright magenta colors in fig. 33). The claystone likely forms a local confining unit below the Potrero wetlands, in a broad gentle syncline that extends west of the Grand Avenue fault (fig. 24B). Red colors in the CDT profile (fig. 33) are interpreted as saturated sandstone or sandy claystone in the Nogales Formation. Yellow to green colors in the CDT profile indicate zones with low electromagnetic conductivity interpreted as unsaturated sediments near the surface or saturated Nogales Formation sandstone at depth.

Figure 34 shows multiple CDT profiles from the Santa Cruz transient electromagnetic study (Bultman and Page, 2016) in the Potrero Creek wetlands area arranged as fences displayed over the geologic map of the Nogales and Rio Rico 7.5′ quadrangles (Page and others, 2016a). The faults on the latter map have since been revised and are shown in figure 24*A*. Profile CDT 505 crosses the Potrero Creek wetlands just west of I–19. Surface water present in the wetlands including an area with ponds developed for the former Palo Duro golf course, may interfere with a CDT solution. Nevertheless, a claystone unit of the Mariposa member of the Nogales Formation is interpreted in the subsurface both east and west of the main wetlands and likely forms a perching horizon that supports the Potrero Creek wetlands. CDT data showing very high conductivities indicative of claystone also appear in CDT 506 immediately south of the wetlands. There, the land surface is at a higher elevation and the claystone may act as a barrier to groundwater flow to the south. Directly north of the wetlands along CDT 504, high-conductivity material is not apparent in the subsurface which is consistent with the absence of surface ponding in that area. In fact, groundwater levels drop to over 49 m depth along CDT 504 just west of I–19. What appears to be an east–northeast-striking fault, or simply the stratigraphic limit of the claystone, may define the northern extent of the perching horizon in this part of the wetlands. This feature is also visible as a horizontal gradient maxima from interpretations based on aeromagnetic data (Bultman and Page, 2016), which may indicate a fault.

The claystone confining unit is not apparent in profile CDT 504 in the area of the Las Lagunas de Anza marsh (fig. 34*C*). Three possible explanations for this include (1) it is an area of active upward movement of water through sandstones and the nearby Grand Avenue fault; (2) poor CDT solutions may not provide good resolution of the claystone in that area due in part to recent fill added to create a drive-in theater (gray area within wetlands boundary in fig. 34*C*) that interferes with solutions to the CDT algorithm. Surface water in the Las Lagunas de Anza area (fig. 28) may also play a role in the lack of a CDT solution; and (3) the sandstone in this area has much lower permeability than elsewhere and allows ponding of surface water without the presence of claystone.

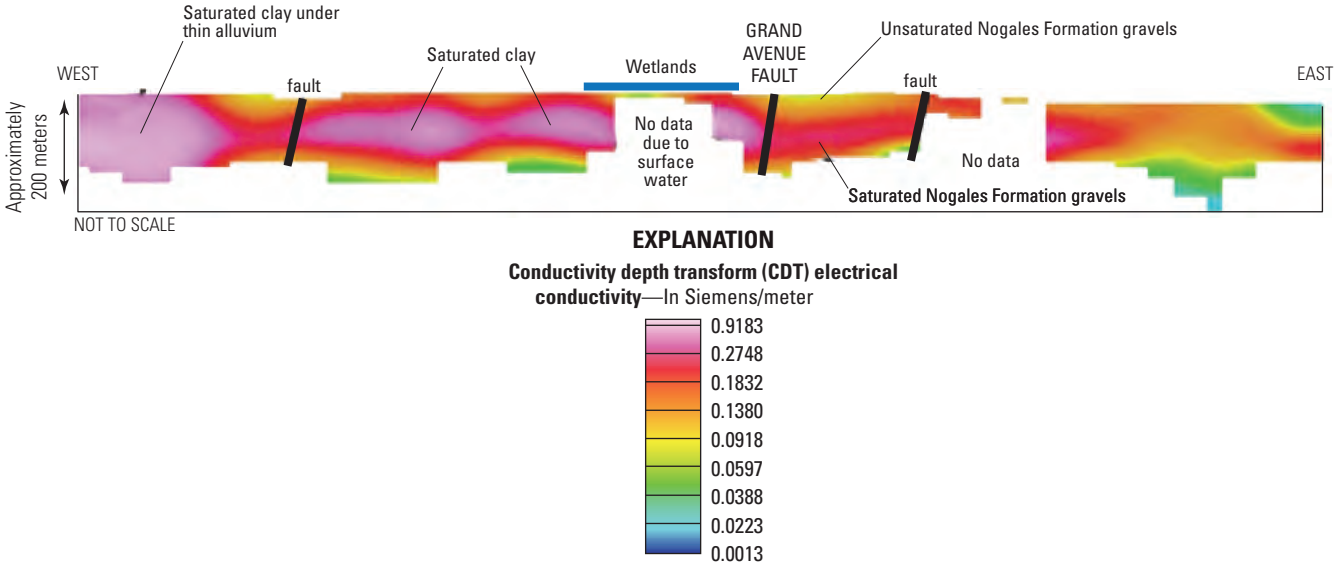

Figure 33. Conductivity depth transform (CDT) profile 505, which is aligned subparallel with cross section A–A' in figure 24. Magenta colors are interpreted to represent a saturated claystone unit in the Mariposa member of the Nogales Formation; red colors are likely saturated gravels in the Nogales Formation; yellow colors are interpreted as unsaturated gravels in the Proto Canyon member of the Nogales Formation, or late Miocene to Holocene gravels. Faults shown as thick black subvertical lines.

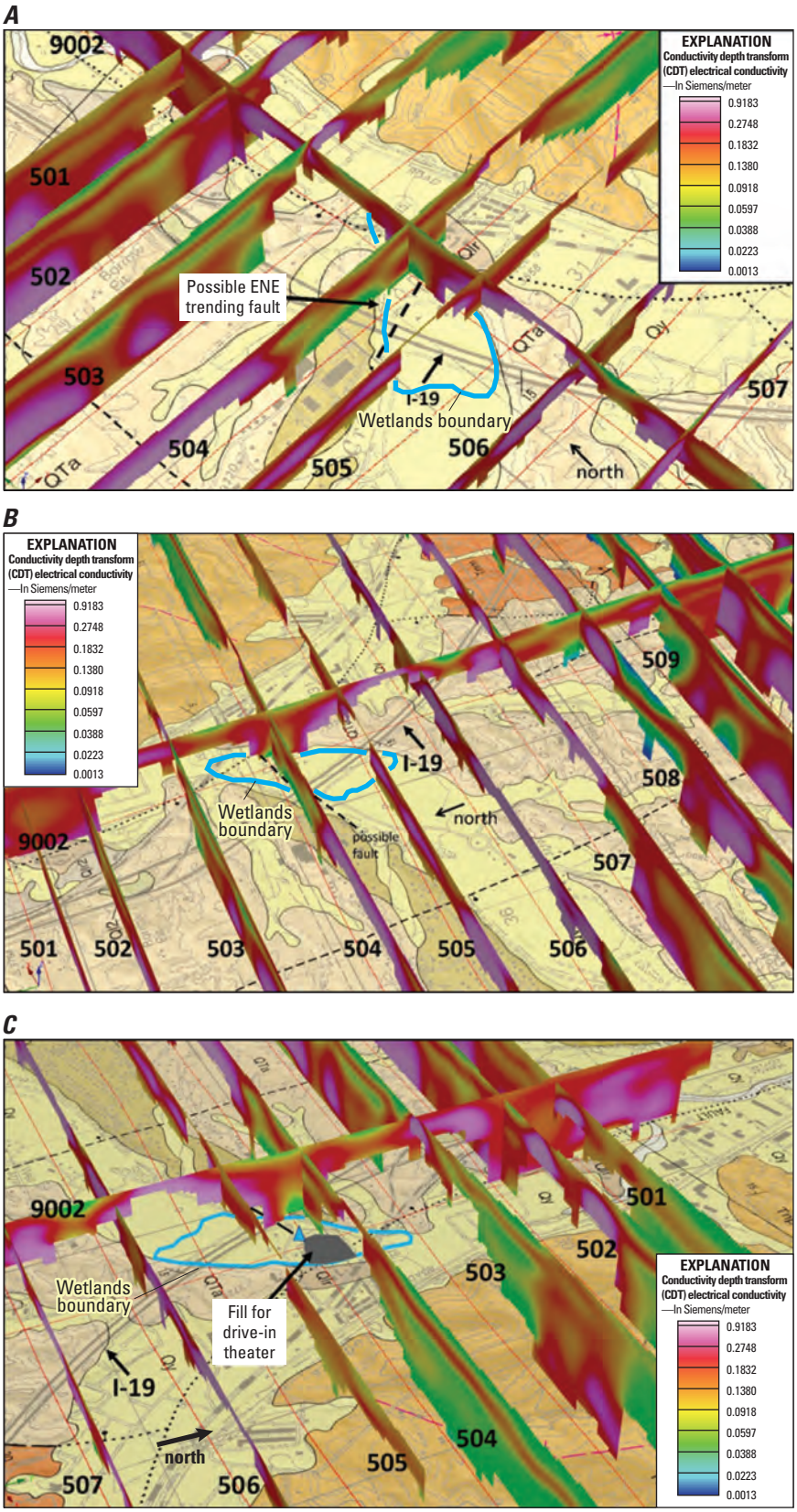

Figure 34. Fence diagram showing a series of east–west conductivity depth transform (CDT) transects labeled 501 to 509 along with a single north–south transect labeled 9002 shown floating above the geologic base map used in figure 24. The red lines on the geologic map that underlie the CDTs are the flight paths over which the CDT data were collected. Fence diagram is centered on the Potrero wetlands and rotated to different azimuth directions in each of the individual figures (A, B, and C) to show different views of the subsurface structure. *A*. Oblique view of the wetlands is from the south-west. *B*. Oblique view of the wetlands is from the west north-west. *C*. Oblique view of the wetlands is from the east south-east. CDT transects are after Bultman and Page (2016).

Contribution of Wetland Discharge to Nogales Wash

Outflow from the Potrero wetlands enters Nogales Wash approximately halfway between sampling sites at East Calle Sonora (Sonora on figs. 27, 29, and 30) and Old Tucson Highway (Tucson in figs. 29 and 30). Although Sr and U isotope data indicate that surface flow in Nogales Wash cannot be a source for perennial water supply to the wetlands (fig. 30), it is hydrologically possible that outflow from the wetlands may constitute a source of water to downstream flow in Nogales Wash. Four samples of surface flow in Nogales Wash sampled in August 2018 showed distinct differences in $^{87}Sr/^{86}Sr$ and [$^{234}U/^{238}U$] compositions between the two upstream sites (samples Morely1 and Sonora in fig. 30) and two downstream sites (samples Tucson and Ruby). Potrero Creek is the only flowing tributary in this reach.

Lower $^{87}Sr/^{86}Sr$ values are observed in downstream samples of Nogales Wash, indicating that additions to streamflow must be dominated by a component with less radiogenic Sr than values observed in wetlands outflow (fig. 32*B*). Sample LL6–5 most likely reflects wetland discharge under baseflow conditions in June of 2019; however, none of the wetland samples have $^{87}Sr/^{86}Sr$ values lower than those observed in upstream Nogales Wash flow. This includes several wetlands samples (PW1, PW2, and PW3) collected on the same day as the Nogales Wash samples. Several simple binary mixing curves between wetland samples and Nogales Wash water sampled at East Calle Sonora (Sonora on figs. 29 and 30) show compositions predicted for downstream samples. Although mixtures have [$^{234}U/^{238}U$] values that overlap compositions observed in Tucson and Ruby samples, none of the results are capable of explaining the lower $^{87}Sr/^{86}Sr$ compositions of downstream Nogales Wash samples. We conclude that the volume of discharge from the Potrero Creek wetlands is small compared to the volume of flow constituting Nogales Wash water, and that addition of other components (not from the wetlands) is required to explain downstream changes in Nogales Wash composition.

Source of Groundwater Discharging in Wetlands

Groundwater upwelling along fractures associated with the Grand Avenue fault is required to provide perennial supply to the Potrero Creek wetlands (fig. 35). Sr and U isotopic data indicate that water sustaining the wetlands is unrelated to groundwater in the regional phreatic aquifer immediately adjacent to the wetlands. However, available data do not define a unique source for the groundwater supporting wetlands and several possibilities may contribute.

The most likely source of groundwater discharging into the wetlands is through fractures and faults associated with the Grand Avenue fault (fig. 24), which strikes north along the east side of the wetlands at the junction of Potrero Wash and Nogales Wash (figs. 24 and 35). Infiltration into the adjacent Mount Benedict fault block and flow through fractures in the Jurassic monzonite represents a potential source of water that may become focused along the Grand Avenue fault. Although elevations in the horst block do not exceed 1400 m making it an unlikely candidate for substantial recharge and the coarsely crystalline plutonic rock has very low overall permeability. $^{87}Sr/^{86}Sr$ values obtained from acetic-acid leachates of two powdered monzonite samples indicate that groundwater flowing through secondary fracture permeability in the pluton is capable of dissolving Sr substantially more radiogenic than Sr in groundwater from alluvial aquifers. Leachate $^{87}Sr/^{86}Sr$ values of 0.711719 and 0.715747 are substantially higher than water sampled in the wetlands. Mixing of groundwater from the horst block having higher $^{87}Sr/^{86}Sr$ with lower-$^{87}Sr/^{86}Sr$ groundwater in the alluvial aquifer as deeper water rises to the surface could result in compositions observed in wetland water.

Another possible source of the wetlands water is recharge of groundwater with elevated $^{87}Sr/^{86}Sr$ from Cretaceous felsic volcanic rocks constituting the Pajarito Mountains to the southwest in both Arizona and Sonora (sheet 1; fig. 7). Rocks include rhyodacite tuff and welded tuff (Drewes, 1980; Riggs, 1985) that would likely have elevated present-day $^{87}Sr/^{86}Sr$ values. Groundwater collection sites in those remote areas are not available, and characterization of radiogenic isotope compositions of those rocks was not attempted. However, results for 9 samples of unmineralized Jurassic and Late Cretaceous felsic plutons across southern Arizona had measured $^{87}Sr/^{86}Sr$ values ranging from 0.70987 to 0.72481 with a median value of 0.71295 (Farmer and DePaolo, 1984), all of which are higher than values measured in Potrero wetland water. The Pajarito highlands reach elevations of 1,500–1,700 m within 13 km of the wetlands. Those highlands may also provide recharge into Nogales Formation alluvial aquifers at lower elevations to supply perennial discharge into the wetlands. However, groundwater would have to flow 13 km under partly confined conditions in the Miocene Nogales Formation gravel aquifers from the Pajarito Mountains to the Potrero wetlands.

Conclusions

Perennial wetlands located along Potrero Creek near its intersection with the Grand Avenue fault require a reliable source of groundwater supply to maintain a diverse ecological environment. Groundwater in the regional phreatic aquifer immediately upgradient of the wetlands is hosted in Quaternary and Tertiary sediments with the potentiometric surface at a depth of 44.5 m. The presence of surface water in the wetlands is thus hydraulically incompatible with a groundwater source from the regional phreatic aquifer. Furthermore, isotopic compositions of strontium (Sr) and uranium (U) in groundwater of the regional phreatic aquifer are distinct from compositions of surface water present in wetlands, although small amounts of mixing between a wetlands water source and groundwater pumped from the regional aquifer can explain the limited amount of $^{87}Sr/^{86}Sr$ and [$^{234}U/^{238}U$] variability

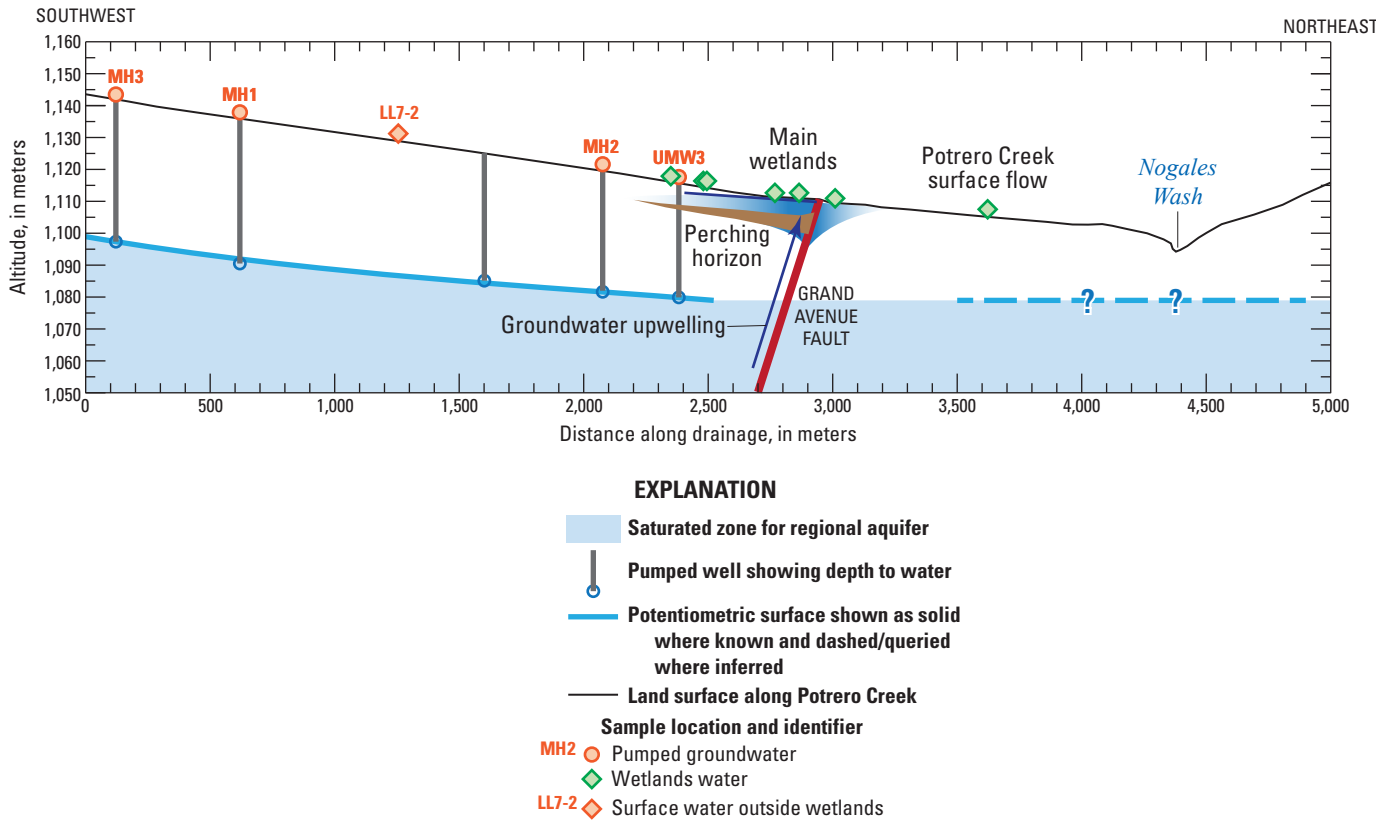

Figure 35. Schematic cross section along Potrero Creek showing the position of the potentiometric surface associated with the regional phreatic aquifer compared to surface water present in the Potrero Creek wetlands. Meadow Hills water wells are shown as orange circles with depths to water listed in table 4. Surface water samples from the wetlands (and the stagnant golf pond sampled as LL7–2) are shown as diamonds. A schematic depiction of deeper groundwater upwelling along the Grand Avenue fault is shown supplying water perched above a low permeability claystone unit beneath the main wetlands area.

observed across the kilometers-long extent of the wetlands. Surface flow from Potrero Creek or Nogales Wash are also considered hydrologically unlikely of supplying year-round flow for the wetlands, and $^{87}Sr/^{86}Sr$ and $[^{234}U/^{238}U]$ compositions in Nogales Wash samples preclude streamflow from the south as a wetlands-water source.

Field mapping and transient electromagnetic conductivity depth transform geophysical surveys indicate the presence of a saturated claystone unit within the Mariposa member of the Nogales Formation that likely forms a local confining unit below the Potrero wetlands. The thickness and depth of this unit has not been determined by borehole investigations, but its presence is interpreted to be an important hydraulic factor allowing groundwater upwelling along the Grand Avenue fault to spread laterally, forming a perching layer that helps maintain shallow saturated conditions.

Total amounts of groundwater supplying the wetlands have not been estimated. Discharge from the wetlands forms surface flow joining Nogales Wash approximately 500 meters to the north. An even larger flux may be lost through pan evaporation from open ponds and marshes, and through evapotranspiration from phreatic vegetation covering the wetland habitats. Contributions of wetland water to the overall streamflow budget of Nogales Wash are not significant based on $^{87}Sr/^{86}Sr$ and $[^{234}U/^{238}U]$ mixing calculations between upstream Nogales Wash and Potrero wetland endmembers. Isotopic compositions observed in downstream Nogales Wash samples require contributions from an additional, unsampled component in order to explain the shift to lower $^{87}Sr/^{86}Sr$ and $[^{234}U/^{238}U]$ values.

We consider the most likely source supplying perennial water to the wetlands is the Jurassic quartz monzonite of Mount Benedict, primarily because it is locally exposed, contains labile radiogenic Sr, and underlies the Potrero wetlands at depth. In addition, the monzonite is fractured and faulted along the Grand Avenue fault, and these structures likely form the conduits providing the wetlands perennial water.

Another possible source of groundwater with radiogenic Sr discharging into the wetlands is the Pajarito Mountains, which consist of Cretaceous felsic volcanic rocks reaching elevations from 1,524 to 1,829 meters. However, we consider the Pajarito Mountains a less likely source primarily because

of their distance (13 kilometers) from the wetlands, and the requirement of at least a partly confined aquifer within the basin sediments across that distance. We conclude further studies are needed to determine the water source(s) of the wetlands more reliably. Nevertheless, investigations presented here provide a foundation and starting point for any further work.

Summary

This report includes an updated geologic map (sheet 1) and cross sections (sheet 2) of the upper Santa Cruz River basin emphasizing Miocene to Holocene basin hydrogeology and structure. The map and text describe the basin aquifers which consist of Miocene to Holocene geologic units. Seven hydrogeologic cross sections are included in the report (sheet 2) and illustrate the geometry, thickness, and structure of the Miocene to Holocene alluvial aquifer units. The results of our most current project hydrogeologic studies are summarized and include (1) mapping and defining the depth to bedrock as illustrated in sheets 1 and 2 to better understand the geometry and structure of the Miocene to Holocene aquifers; (2) describing hydraulically significant faults in the map area; (3) describing the depth to bedrock, hydrogeology, and structure in the Sopori Wash and Peck Canyon focus areas; and (4) evaluating groundwater sources and the hydrogeology of the Potrero Creek wetlands area based on isotopic data, groundwater geochemistry, and geologic and geophysical data.

References Cited

Aldridge, B.N., and Eychaner, J.H., 1984, Floods of October 1977 in Southern Arizona and March 1978 in Central Arizona: U.S. Geological Survey Water-Supply Paper 2379, 143 p., accessed January 5, 2022, at https://pubs.usgs.gov/wsp/2223/report.pdf.

Andrews, J.N., and Kay, R.L.F., 1982, $^{234}U/^{238}U$ activity ratios of dissolved uranium groundwaters from a Jurassic limestone aquifer in England: Earth and Planetary Science Letters, v. 57, no. 1, p. 139–151, accessed January 5, 2022 at https://doi.org/10.1016/0012-821X(82)90180-7.

Arizona Department of Water Resources, 2021, Registry of wells in Arizona, accessed November 9, 2021, at https://azwatermaps.azwater.gov/WellReg.

Betancourt, J.L., 1990, Tucson's Santa Cruz River and the arroyo legacy: Tucson, University of Arizona, Ph.D. dissertation, 239 p.

Briggs, I.C., 1974, Machine contouring using minimum curvature: Geophysics, v. 39, no. 1, p. 39–48. [Also available at https://doi.org/10.1190/1.1440410.]

Bull, W.B., 1991, Geomorphic responses to climate change: New York, Oxford University Press, 326 p.

Bultman, M.W., 2015, Detailed interpretation of aeromagnetic data from the Patagonia Mountains area, southeastern Arizona: U.S. Geological Survey Scientific Investigations Report 2015–5029, 25 p.

Bultman, M.W., 2023, Sopori Wash sub-basin gravity data, Pima and Santa Cruz Counties, Arizona: U.S. Geological Survey data release, https://doi.org/10.5066/P9MBNX4O.

Bultman, M.W., and Page, W.R., 2016, Bedrock morphology and structure, upper Santa Cruz Basin, south-central Arizona, with Transient Electromagnetic Survey Data: U.S. Geological Survey Open-File Report 2016–1152, 49 p. [Also available at https://doi.org/10.3133/ofr20161152.]

Cebula, G.T., Kunk, M.J., Mehnert, H.H., Naeser, C.W., Obradovich, J.D., and Sutter, J.F., 1986, The Fish Canyon Tuff, a potential standard for the ^{40}Ar-^{39}Ar and fission-track methods: Terra Cognita, v. 6, no. 2, p. 139–140. [abs.].

Cheng, H., Edwards, R.L., Shen, C.-C., Polyak, V.J., Asmerom, Y., Woodhead, J., Hellstrom, J., Wang, Y., Kong, X., Spötl, C., Wang, X., and Alexander, E.C., Jr., 2013, Improvements in ^{230}Th dating, ^{230}Th and ^{234}U half-life values, and U–Th isotopic measurements by multi-collector inductively coupled plasma mass spectrometry: Earth and Planetary Science Letters, v. 371–372, p. 82–91, accessed January 5, 2022, at https://doi.org/10.1016/j.epsl.2013.04.006.

Clark, I., and Fritz, P., 1997, Environmental isotopes in hydrogeology: New York, Lewis Publishers, 328 p.

Cohen, K.M., Finney, S.C., Gibbard, P.L., and Fan, J.-X., 2013, The ICS international chronostratigraphic chart: Episodes, v. 36, no. 3, p. 199–204, at https://doi.org/10.18814/epiiugs/2013/v36i3/002.

Cosca, M.A., Page, W.R., Gray, F., Menges, C.M., Lee, J.P., and Bultman, M., 2013, $^{40}Ar/^{39}Ar$ geochronology of the Oligocene Grosvenor Hills Volcanics and the Miocene Nogales Formation, upper Santa Cruz Basin, southern Arizona [abs.]: Geological Society of America Abstracts with Programs, v. 45, no. 7, 129 p.

Damon, P.E., and Bikerman, M., 1964, Potassium-Argon dating of Post-Laramide plutonic and volcanic rocks within the Basin and Range province of Southeastern Arizona and adjacent areas: Arizona Geological Society Digest, v. 7, p. 63–78.

Damon, P.E., Shafiqullah, M., Harris, R.C., and Spencer, J.E., 1996, Compilation of unpublished Arizona K-Ar dates from the University of Arizona Laboratory of Isotope Geochemistry, 1971–1991: Arizona Geological Survey Open-File Report 96–18, 53 p.

Deino, A., and Potts, R., 1990, Single-crystal $^{40}Ar/^{39}Ar$ dating of the Olorgesailie Formation, southern Kenya rift: Journal of Geophysical Research, v. 95, B6, p. 8453–8470, accessed January 5, 2022, at https://doi.org/10.1029/JB095iB06p08453.

DeMeo, G.A., Lazniak, R.J., Boyd, R.A., Smith, J.L., and Nylund, W.E., 2003, Estimated groundwater discharge by evapotranspiration from Death Valley, California, 1997–2001: U.S. Geological Survey Water Resources Investigation Report 03–4254, 27 p., accessed January 5, 2022, at https://pubs.usgs.gov/wri/wrir034254/.

DeMeo, G.A., Smith, J.L., Damar, N.A., and Darnell, J., 2008, Quantifying groundwater and surface water discharge from evapotranspiration processes in 12 hydrographic areas of the Colorado regional groundwater flow system, Nevada, Utah, and Arizona: U.S. Geological Survey Scientific Investigations Report 2008–5116, 22 p., accessed January 5, 2022, at https://pubs.usgs.gov/sir/2008/5116/.

Drewes, H., 1971a, Mesozoic stratigraphy of the Santa Rita Mountains, southeast of Tucson, Arizona: U.S. Geological Survey Professional Paper 658–C, 81 p. [Also available at https://doi.org/10.3133/pp658C.]

Drewes, H., 1971b, Geologic map of the Mount Wrightson quadrangle, southeast of Tucson, Santa Cruz and Pima Counties, Arizona: U.S. Geological Survey Miscellaneous Geologic Investigations Map I–614, scale 1:48,000.

Drewes, H., 1972, Cenozoic rocks of the Santa Rita Mountains, southeast of Tucson, Arizona: U.S. Geological Survey Professional Paper 746, 66 p., accessed January 5, 2022, at https://doi.org/10.3133/pp746.

Drewes, H., 1980, Tectonic map of southeast Arizona: U.S. Geological Survey Miscellaneous Investigations Series Map I–1109, 2 sheets, scale 1:125,000, accessed January 5, 2022, at https://doi.org/10.3133/ofr79775.

Drewes, H., 1981, Tectonics of southeastern Arizona: U.S. Geological Survey Professional Paper 1144, 270 p. [Also available at https://doi.org/10.3133/pp1144.]

Drewes, H., Fields, R.A., Hirschberg, D.M., and Bolm, K.S., 2002, Spatial digital database for the tectonic map of southeast Arizona: U.S. Geological Survey Miscellaneous Investigations Series Map I–1109, Digital database, version 2.0., accessed January 5, 2022, at https://pubs.usgs.gov/imap/i1109/i1109.pdf.

Drexler, J.Z., Paces, J.B., Alpers, C.N., Windham-Myers, L., Neymark, L.A., Bullen, T.D., and Taylor, H.E., 2014, $^{234}U/^{238}U$ and δ^{87} Sr in peat as tracers of paleosalinity in the Sacramento- San Joaquin Delta of California, USA: Applied Geochemistry, v. 40, p. 164–179, accessed January 5, 2022, at https://doi.org/10.1016/j.apgeochem.2013.10.011.

EnviroNet Inc, 1997, Potrero Creek wetlands management plan and feasibility report: Arizona Water Protection Fund publication 95–024WPF, 28 p., accessed January 5, 2022, at https://www.azwpf.gov/sites/default/files/media/95-024WPF-ManagementPlanandFeasibilityStudy.pdf.

Farmer, G.L., and DePaolo, D.J., 1984, Origin of Mesozoic and Tertiary granite in the western United States and implications for pre-Mesozoic crustal structure—2. Nd and Sr isotopic studies of unmineralized and Cu- and Mo-mineralized granite in the Precambrian craton: Journal of Geophysical Research, v. 89, no. B12, p. 10141–10160. [Also available at https://doi.org/10.1029/JB089iB12p10141.]

Faure, G., and Mensing, T.M., 2005, Isotopes—Principles and applications 3rd ed.: New York, John Wiley & Sons, 897 p.

Gettings, M.E., and Houser, B.B., 1997, Basin geology of the upper Santa Cruz Basin, Pima and Santa Cruz Counties, southeastern Arizona: U.S. Geological Survey Open-File Report 97–676, 39 p. [Also available at https://doi.org/10.3133/ofr97676.]

Graybeal, F.T., Moyer, L.A., Vikre, P.G., Dunlap, P., and Wallis, J.C., 2015, Geologic map of the Patagonia Mountains, Santa Cruz County, Arizona: U.S. Geological Survey Open-File Report 2015–1023, scale 1:48,000, accessed January 5, 2022, at https://pubs.usgs.gov/of/2015/1023/.

Helmick, W.R., 1986, The Santa Cruz River terraces near Tubac, Santa Cruz County, Arizona: University of Arizona M.S. Thesis, Tucson, 96 p.

Houser, B.B., Peters, L., Esser, R.P., and Gettings, M.E., 2004, Stratigraphy and tectonic history of the Tucson basin, Pima County, Arizona, based on Exon State (32)–1 well: U.S. Geological Survey Scientific Investigations Report 2004–5076, 32 p., accessed January 5, 2022, at https://pubs.usgs.gov/sir/2004/5076/.

Jia, Hong-jing, Li, Shun-qun, and Li, Lin, 2014, The relationship between the electrical resistivity and saturation of unsaturated soil: Electronic Journal of Geotechnical Engineering, v. 19, p. 3739–3746.

Kuiper, K.F., Deino, A., Hilgen, F.J., Krijgsman, W., Renne, P.R., and Wijbrans, J.R., 2008, Synchronizing rock clocks of Earth history: Science, v. 320, no. 5875, p. 500–504, accessed January 5, 2022, at https://doi.org/10.1126/science.1154339.

Laczniak, R.J., DeMeo, G.A., Reiner, S.R., Smith, J.L., and Nylund, W.E., 1999, Estimates of ground-water discharge as determined from measurements of evapotranspiration, Ash Meadows area, Nye County, Nevada: U.S. Geological Survey Water Resources Investigation Report 99–4079, 70 p., accessed January 5, 2022, at https://doi.org/10.3133/wri994079.

Lee, M., House, P.K., and Pearthree, P.A., 1999, Historical geomorphology and hydrology of the Santa Cruz River: Arizona Geological Survey Open-File Report 99–13, 98 p., accessed January 5, 2022, at http://repository.azgs.az.gov/sites/default/files/dlio/files/nid824/ofr-99-13_santa_cruz_river.pdf.

Leenhouts, J.M., Stromberg, J.C., and Scott, R.L., 2006, Hydrologic requirements of and consumptive groundwater use by riparian vegetation along the San Pedro River, Arizona: U.S. Geological Survey Scientific Investigations Report 2005–5163, 154 p.

Lindsey, D.A., and Van Gosen, B.S., 2005, Surface geologic map of the Mount Hopkins and northern part of the San Cayetano 7.5′ quadrangles, Santa Cruz and Pima Counties, Arizona: Arizona Geological Survey Contributed Map 06–A (CM–06–A), 1 sheet, scale 1:24,000.

Lindsey, D.A., and Van Gosen, B.S., 2010, Processes of terrace formation on the piedmont of the Santa Cruz River valley during Quaternary time, Green Valley—Tubac area, southeastern Arizona: U.S. Geological Survey Scientific Investigations Report 2010–5028, 39 p. [Also available at https://doi.org/10.3133/sir20105028.]

Lipman, P.W., and Sawyer, D.A., 1985, Mesozoic ash-flow caldera fragments in southeastern Arizona and their relation to porphyry copper deposits: Geology, v. 13, no. 9, p. 652–656, accessed January 5, 2022, at https://doi.org/10.1130/0091-7613(1985)13<652:MACFIS>2.0.CO;2.

Ludwig, K.R., Wallace, A.R., and Simmons, K.R., 1985, The Schwartzwalder uranium deposit, II—Age of uranium mineralization and Pb-isotope constraints on genesis: Economic Geology and the Bulletin of the Society of Economic Geologists, v. 80, no. 7, p. 1858–1871.

McArthur, J.M., Howarth, R.J., and Bailey, R.R., 2001, Strontium isotope stratigraphy—LOWESS version 3, best fit to the marine Sr-isotope curve for 0–509 Ma and accompanying look-up table for deriving numerical age: The Journal of Geology, v. 109, no. 2, p. 155–170, accessed January 5, 2022, at https://doi.org/10.1086/319243.

McArthur, J.M., Rio, D., Massari, F., Castradori, D., Bailey, T.R., Thirlwall, M., and Houghton, S., 2006, A revised Pliocene record for marine-$^{87}Sr/^{86}Sr$ used to date an interglacial event recorded in the Cockburn Island Formation, Antarctic Peninsula: Palaeogeography, Palaeoclimatology, Palaeoecology, v. 242, no. 1–2, p. 126–136, accessed January 5, 2022, at https://doi.org/10.1016/j.palaeo.2006.06.004.

Marvin, R.F., Stern, T.W., Creasey, S.C., and Mehnert, H.H., 1973, Radiometric ages of igneous rocks in from Pima, Santa Cruz, and Cochise Counties, Arizona: U.S. Geological Survey Bulletin 1379, 27 p.

Menges, C.M., 1981, The Sonoita Creek Basin, implications for Late Cenozoic tectonic evolution of basin and ranges in southeastern Arizona: Tucson, University of Arizona, M.S. Thesis, 239 p.

Menges, C.M., and McFadden, L.D., 1981, Evidence for a latest Miocene to Pliocene, transition from Basin-and-Range tectonic to post tectonic landscape evolution in southeastern Arizona, *in* Stone, Claudia, and Jenny, J.P., eds.: Arizona Geological Society Digest XVII, p. 649–680.

Menges, C.M., and Pearthree, P.A., 1989, Late Cenozoic tectonisim and its impact on regional landscape evolution, *in* Jenny, J.P., and Reynolds, S.J., eds.: Arizona Geological Society Digest XVII, p. 649–680.

Min, K.W., Mundil, R., Renne, P.R., and Ludwig, K.R., 2000, A test for systematic errors in $^{40}Ar/^{39}Ar$ geochronology through comparison with U/Pb analysis of a 1.1-Ga rhyolite: Geochimica et Cosmochimica Acta, v. 64, no. 1, p. 73–98, accessed January 5, 2022, at https://doi.org/10.1016/S0016-7037(99)00204-5.

Morgan, L.E., 2021, Argon data for Santa Cruz Basin, Arizona (ver. 1.1, November 2022): U.S. Geological Survey data release, accessed December 1, 2022, at https://doi.org/10.5066/P94NR0D9.

Nelson, F.J., 1963, Geologic map of Pena Blanca and Walker Canyon area, Santa Cruz County, Arizona: M.S. thesis, University of Arizona, Tucson, Arizona, scale 1:16,700.

Nelson, K., 2007, Groundwater flow model of the Santa Cruz active management area along the effluent-dominated Santa Cruz River, Santa Cruz and Pima Counties, Arizona: Arizona Department of Water Resources Modeling Report No. 14, 117 p., accessed January 5, 2022, at https://new.azwater.gov/sites/default/files/Modeling_Report_14_0.pdf.

Paces, J.B., 2021, Sr-, U-, H- and O-isotope data used to evaluate water sources in the Potrero Creek Wetlands, Upper Santa Cruz Basin, southern Arizona, USA: U.S. Geological Survey data release, accessed January 5, 2022, at https://doi.org/10.5066/P9XXW25T.

Paces, J., Gray, F., Hart, O.E., and Page, W.R., 2019, Evaluating water sources in Potrero Creek Wetlands using $^{87}Sr/^{86}Sr$ and U^{234}/U^{238} isotopes: Geological Society of America Abstracts with Programs, v. 51, no. 5, accessed January 5, 2022, at https://doi.org/10.1130/abs/2019AM-335643.

Paces, J.B., Ludwig, K.R., Peterman, Z.E., and Neymark, L.A., 2002, $^{234}U/^{238}U$ evidence for local recharge and patterns of ground-water flow in the vicinity of Yucca Mountain, Nevada, USA: Applied Geochemistry, v. 17, no. 6, p. 751–779, accessed January 5, 2022, at https://doi.org/10.1016/S0883-2927(02)00037-9.

Paces, J.B., Palmer, M.V., Palmer, A.N., Long, A.J., and Emmons, M.P., 2020, 300,000 yr history of water-table fluctuations at Wind Cave, South Dakota, USA—Scale, timing, and groundwater mixing in the Madison Aquifer: Geological Society of America Bulletin, v. 132, nos. 7–8, p. 1447–1468, accessed January 5, 2022, at https://doi.org/10.1130/B35312.1. GSA Data Repository Item 2020023 accessed January 5, 2022, at https://gsapubs.figshare.com/articles/journal_contribution/Supplemental_Material_300_000_yr_history_of_water-table_fluctuations_at_Wind_Cave_South_Dakota_USA_Scale_timing_and_groundwater_mixing_in_the_Madison_Aquifer/12542240.

Paces, J.B., and Wurster, F.C., 2014, Natural uranium and strontium isotope tracers of water sources and surface water–groundwater interactions in arid wetlands—Pahranagat Valley, Nevada, USA: Journal of Hydrology (Amsterdam), v. 517, p. 213–225, accessed January 5, 2022, at https://doi.org/10.1016/j.jhydrol.2014.05.011.

Page, W.R., Bultman, M.W., Berry, M.E., Turner, K.J., Menges, C.M., Gray, F., Paces, J.B., VanSistine, D.P., Morgan, L.E., and Havens, J.C., 2023, Database for the geologic map of the upper Santa Cruz River basin, southern Arizona: U.S. Geological Survey data release, https://doi.org/10.5066/P9PGUZV0.

Page, W.R., Bultman, M.W., VanSistine, D.P., Menges, C.M., Gray, F., and Pantea, M.P., 2018, Geologic framework and hydrogeology of the Rio Rico and Nogales 7.5′ quadrangles, Arizona, with three-dimensional hydrogeologic model: U.S. Geological Survey Scientific Investigations Report 2018–5062, 34 p.

Page, W.R., Gray, F., Bultman, M.W., and Menges, C.M., 2016a, Hydrogeologic investigations of the Nogales Formation in the Nogales area, Upper Santa Cruz Basin, Arizona: U.S. Geological Survey Scientific Investigations Report 2016–5087, 31 p. [Also available at https://doi.org/10.3133/sir20165087.]

Page, W.R., Menges, C.M., Gray, F., Berry, M.E., Bultman, M.W., Cosca, M.A., and VanSistine, D.P., 2016b, Geologic map of the Rio Rico and Nogales 7.5′ quadrangles, Santa Cruz County, Arizona: U.S. Geological Survey Scientific Investigations Map 3354, scale 1:24,000, accessed January 5, 2022, at https://doi.org/10.3133/sim3354.

Pearthree, P.A., and Biggs, T.H., 1999, Surficial geology and geologic hazards of the Tucson Mountains: Arizona Geological Survey Open-File Report 99-22, 12 p., 2 sheets, scale 1:24,000.

Pearthree, P.A., and Youberg, A., 2000, Surficial geologic map and geologic hazards of the Green Valley—Sahuarita area, Pima County, Arizona: Arizona Geological Survey, Digital Map 3 (DGM–03), 21 p., 2 pls., scale 1:24,000.

Porcelli, D., 2008, Investigating groundwater processes using U- and Th-series nuclides, chap. 4 *of* Krishnaswami, S., and Cochran, J.K., eds., U-Th Series Nuclides in Aquatic Systems: Radioactivity in the Environment, v. 13, p. 105–153, accessed January 5, 2022, at https://doi.org/10.1016/S1569-4860(07)00004-6.

Reiner, S.R., Lazniak, R.J., DeMeo, G.A., Smith, J.L., Elliott, P.E., Nylund, W.E., and Fridrich, C.J., 2002, Groundwater discharge determined from measurements of evapotranspiration, other available hydrologic components, and shallow water-level changes, Oasis Valley, Nye County, Nevada: U.S. Geological Survey Water Resources Investigation Report 01–4239, 65 p., accessed January 5, 2022, at https://doi.org/10.3133/wri014239.

Reinhard, K.J., and Shipman, J.H., 1978, Prehistoric cremations from Nogales, Arizona: The Kiva, v. 43, no. 3-4, p. 231–252, accessed January 5, 2022, at https://doi.org/10.1080/00231940.1978.11757902.

Renne, P.R., Swisher, C.C., Deino, A.L., Karner, D.B., Owens, T.L., and DePaolo, D.J., 1998, Intercalibration of standards, absolute ages and uncertainties in $^{40}Ar/^{39}Ar$ dating: Chemical Geology, v. 145, no. 1–2, p. 117–152, accessed January 5, 2022, at https://doi.org/10.1016/S0009-2541(97)00159-9.

Riggs, N.R., 1985, Stratigraphy, structure, and mineralization of the Pajarito Mountains, Santa Cruz County, Arizona [M.S. thesis]: Tucson, University of Arizona, 102 p.

Riggs, N.R., and Busby-Spera, C.G., 1991, Facies analysis of an ancient, dismembered, large caldera complex and implications for intra-arc subsidence—Middle Jurassic strata of Cobre Ridge, southern Arizona, *in* Cas, R., and Busby-Spera, C., eds.: Volcaniclastic Sedimentation—Sedimentary Geology, v. 74, nos. 1–4, p. 39–68, accessed January 5, 2022, at https://doi.org/10.1016/0037-0738(91)90034-B.

Rozanski, K., Araguás-Araguás, L., and Gonfiantini, R., 1993, Isotopic patterns in modern global precipitation, *in* Swart, P.K., Lohmann, K.C., McKenzie, J., and Savin, S., eds., Climate Change in Continental Isotopic Records—Geophysics Monograph Series v. 78: Washington, DC, American Geophysical Union, p. 1–36, accessed January 5, 2022, at https://doi.org/10.1029/GM078p0001.

Saltus, R.W., and Jachens, R.C., 1995, Gravity and basin-depth maps of the Basin and Range Province, Western United States: U.S. Geological Survey Geophysical Investigations Map, GP–1012, 1 sheet, scale 1:2,500,000, accessed January 5, 2022, at https://doi.org/10.3133/gp1012.

Seaman, S.J., Scherer, E.E., and Standish, J.J., 1995, Multistage magma mingling and the origin of flow banding in the Aliso lava dome, Tumacacori Mountains, southern Arizona: Journal of Geophysical Research, v. 100, B5, p. 8381–8398, accessed January 5, 2022, at https://doi.org/10.1029/94JB03260.

Sellers, W.D., and Hill, R.H., 1974, Arizona Climate, 1931–1972 2nd ed.: Tucson, Ariz., University of Arizona Press, 616 p.

Simons, F.S., 1974, Geologic map and sections of the Nogales and Lochiel quadrangles, Santa Cruz County, Arizona: U.S. Geological Survey Miscellaneous Investigations Series Map I–762, 9-p. pamphlet, scale 1:48,000, accessed January 5, 2022, at https://doi.org/10.3133/i762.

Steiger, R.H., and Jäger, E., 1977, Subcommission on geochronology—Convention on the use of decay constants in geo- and cosmochronology: Earth and Planetary Science Letters, v. 36, no. 3, p. 359–362, accessed January 5, 2022, at https://doi.org/10.1016/0012-821X(77)90060-7.

Suksi, J., Rasilainen, K., and Pitkanen, P., 2006, Variations in $^{234}U/^{238}U$ activity ratios in groundwater—A key to flow system characterization?: Physics and Chemistry of the Earth Parts A/B/C, v. 31, no. 10–14, p. 556–571. [Also available at https://doi.org/10.1016/j.pce.2006.04.007.]

Swain, C.J., 1976, A Fortran IV program for interpolating irregularly spaced data using the difference equations for minimum curvature: Computers & Geosciences, v. 1, no. 4, p. 231–240, accessed January 5, 2022, at https://doi.org/10.1016/0098-3004(76)90071-6.

Teggart, F.J., 1913, The Anza expedition of 1775–1776, Diary of Pedro Font: Publications of the Academy of Pacific Coast History, v. 3, no. 1, 131 p., accessed January 5, 2022, at https://books.google.com/books?id=7XcUAAAAYAAJ&printsec=frontcover&source=gbs_ge_summary_r&cad=0#v=onepage&q&f=false.

Telford, W.M., Geldart, L.P., and Sheriff, R.E., 1990, Applied Geophysics 2nd ed.: Cambridge, Cambridge University Press, 770 p. [Also available at https://doi.org/10.1017/CBO9781139167932.]

U.S. Department of Agriculture Natural Resources Conservation Service, 2008, Soil Survey Geographic (SSURGO) database for Santa Cruz and parts of Cochise and Pima Counties, Arizona: U.S. Department of Agriculture Natural Resources Conservation Service, az667, accessed October 21, 2010, at https://websoilsurvey.sc.egov.usda.gov/App/HomePage.htm.

U.S. Geological Survey Geologic Names Committee, 2018, Divisions of geologic time—Major chronostratigraphic and geochronologic units: U.S. Geological Survey Fact Sheet 2018–3054, 2 p. [Also available at https://doi.org/10.3133/fs20183054.]

Vallée, M.A., and Smith, R.S., 2007, Comparison of fixed-wing airborne electromagnetic 1D inversion methods, *in* 5th Decennial International Conference on Mineral Exploration, Poster Papers, Toronto, September 9–12, 2007: Exploration 07, accessed in 2014, at http://www.dmec.ca/ex07-dvd/E07/posters.html.

Vikre, P.G., Graybeal, F.T., Fleck, R.J., Barton, M.D., and Seedorff, E., 2014, Succession of Laramide magmatic and magmatic-hydrothermal events in the Patagonia Mounntains, Santa Cruz County, Arizona: Economic Geology and the Bulletin of the Society of Economic Geologists, v. 109, no. 6, p. 1667–1704, accessed January 5, 2022, at https://doi.org/10.2113/econgeo.109.6.1667.

Webb, R.H., and Betancourt, J.L., 1992, Climatic variability and flood frequency of the Santa Cruz River, Pima County, Arizona: U.S. Geological Survey Water-Supply Paper 2379, 40 p.

Wolfgram, P., and Karlik, G., 1995, Conductivity-depth transform of GEOTEM data: Exploration Geophysics, v. 26, no. 2–3, p. 179–185, accessed January 5, 2022, at https://doi.org/10.1071/EG995179.

Wood, M.L., House, P.K., and Pearthree, P.A., 1999, Historical geomorphology and hydrology of the Santa Cruz River, Arizona Geological Survey Open-File Report 99–13, 98 p., 1 pl., scale 1:100,000.

Youberg, A., and Helmick, W.R., 2001, Surficial geologic maps and geologic hazards of the Amado-Tubac area, Santa Cruz and southern Pima Counties, Arizona: Arizona Geological Survey Digital Map 13, scale 1:24,000.

Publishing support provided by the Science Publishing Network, Denver Publishing Service Center

For more information concerning the research in this report, contact the

Center Director, USGS Geosciences and Environmental Change Science Center

Box 25046, Mail Stop 980

Denver, CO 80225

(303) 236-5344

Or visit the Geosciences and Environmental Change Science Center website at https://www.usgs.gov/centers/gecsc

ISSN 2329-132X (online)
https://doi.org/10.3133/sim3490